SEISMIC ANALYSIS OF AN ANCIENT LIGHTHOUSE BY MESO-SCALE MODELING TECHNIQUE

A Thesis Submitted to
the Graduate School of Engineering and Sciences of
İzmir Institute of Technology
in Partial Fulfillment of the Requirements for the Degree of

MASTER OF SCIENCE

in Civil Engineering

by
Safiyullah Üveys GÖZÜN

December 2020
İZMİR

ACKNOWLEDGEMENTS

I would like to thank to my advisor Assoc. Prof. Dr. İzzet Özdemir and my co-advisor Assoc. Prof. Dr. Cemalettin Dönmez for their invaluable effort and patience in supervising me.

I would also like to thank to Deniz Alkan for the information and opportunities he provided me throughout this thesis.

I am thankful to my dear family and friends for their support and encouragement.

ABSTRACT

SEISMIC ANALYSIS OF AN ANCIENT LIGHTHOUSE BY MESO-SCALE MODELING TECHNIQUE

Modeling masonry structures has always been a difficult subject due to the lack of information about the behavior, the heterogeneity of the masonry materials and complex geometries of masonry structures. In terms of the computational costs and complexity, several methods are proposed in the literature.

In this thesis, the capabilities of the meso-scale modeling technique are investigated by means of two experiments selected from the literature and the seismic response of an ancient lighthouse. Brick and mortar type structure is idealized as expanded units surrounded by zero thickness cohesive interfaces representing the mortar behavior. This means that the failure of mortar layers is considered explicitly by means of cohesive surfaces whereas the mechanical response of expanded units is described by Drucker-Prager/Cap model. This approach is used to simulate the in-plane and the out-of-plane behavior of masonry walls reported in the literature. After validating the models with the experimental results, implicit-dynamic time history analyses of an ancient lighthouse are conducted by using 2 different earthquake records. The influence of mortar properties on the energy dissipation mechanisms and collapse pattern of the structure are investigated by means of a parametric study. As an attempt to identify the critical earthquake level corresponding to the initiation of sliding within the lighthouse, a set of additional analyses are conducted with scaled earthquake records.

ÖZET

ORTA SEVİYE DETAYLI MODELLEME TEKNİĞİ İLE ANTİK BİR DENİZ FENERİNİN SİSMİK ANALİZİ

Yığma yapıların modellenmesi, davranış hakkındaki bilgi eksikliği, duvar malzemelerinin heterojenliği ve yığma yapıların karmaşık geometrileri nedeniyle her zaman zor bir konu olmuştur. Hesaplama maliyetleri ve karmaşıklığı açısından, literatürde farklı yöntemler önerilmiştir.

Bu tezde, orta ölçekli modelleme tekniği, literatürden seçilen iki deney ve eski bir deniz fenerinin sismik davranışı ile incelenmiştir. Tuğla ve harç tipi yapı, harç davranışını temsil eden sıfır kalınlıkta kohezif arayüzlerle çevrili genişletilmiş birimler olarak idealize edilmiştir. Bu, harç tabakalarının bozulmasının, kohezif yüzeyler aracılığıyla modellendiği anlamına gelirken, genişletilmiş birimlerin mekanik özellikleri Drucker-Prager / Cap modeli tarafından tanımlanmaktadır. Bu yaklaşım, literatürde bulunan yığma duvarlarının düzlem içi ve düzlem dışı davranışını simüle etmek için kullanılır. Modeller deneysel sonuçlarla doğrulandıktan sonra, eski bir deniz fenerinin zaman tanımı alanındaki dinamik analizleri, 2 farklı deprem kaydı kullanılarak yapılmıştır. Harç özelliklerinin yapının enerji sönümleme mekanizmalarına ve göçme mekanizmasına etkisi parametrik bir çalışma ile incelenmiştir. Deniz feneri içerisinde, kopmaların başlamasına karşılık gelen kritik deprem düzeyinin belirlenmesi amacıyla, ölçekli deprem kayıtları ile bir dizi ek analiz yapılmıştır.

TABLE OF CONTENTS

LIST OF FIGURES

Figure **Page**

Figure **Page**

Figure **Page**

Figure **Page**

Figure **Page**

LIST OF TABLES

CHAPTER 1

INTRODUCTION

Masonry is one of the oldest techniques to build a structure. In most of the historical structures such as bridges, mosques, towers, or ordinary structures, it can be seen that the main structural system is composed of bulk units (stones, bricks, clay blocks) and mortar joints. The main reason to use masonry is its construction simplicity. Aesthetics, durability, solidity, low maintenance, sound absorption, and resistance to fire are also important characteristics of masonry. At the present day, the usage of masonry is limited but it is still in demand. Retaining walls, pre-stressed masonry members, low-rise masonry structures can be shown as evidence that usage of masonry still exists. They are also used in steel or concrete structures as infill walls.

Stone probably was the first material that was used to construct masonry structures. The oldest examples of the first stone masonry houses were found near Lake Hullen, Israel (c. 9000-8000 BC) which were circular and semi-subterranean dry-stone huts with diameters of 3 to 9 m. Pharaonic pyramids of Egyptian Architecture (c. 2800-2000 BC), temples, palaces, arches, churches, bricks and several types of structures which belong to Roman and Romanesque architecture (c. AD 0-1200), gorgeous cathedrals of Gothic architectures (c. AD 1200-1600) are some legacies of stone masonry which survived until today. (Lourenco 1996)

In time, as an alternative to stone, mud-brick was started to be used as a masonry material. The emergence of sun-dried bricks occurred in crowded places of ancient times. The hot dry climate, the abundance of clay, shortage of timber and stones which can be used without cutting were the main motivations for developing the brick. Loaf-shaped mud bricks which were found at Jericho, Palestine (c. 8350-7350 BC) are impressive examples of mudbrick. In addition to mudbrick, it had been seen that burnt bricks were stronger and more durable. The reference in the Bible is Genesis XI, 3-4, when the inhabitants of Babylonia “said to one another ‘Come, let us make bricks and bake them’. They used brick for stone and bitumen for mortar. Then they said ‘Let us build ourselves a city and a tower with its top in the heavens’” is the most famous reference of the usage of burnt brick. Then probable the first skyscraper is built by using brick for stone and bitumen for mortar. (Lourenco 1996)

Some of the historical structures are still in use at present (Feilden 2003) despite other ones remains as ruins (Ashurts 2007). It is certain that historical structures get damage like cracks or collapses with time because of deterioration of the materials, seismic actions, or settlements. Therefore, they need strengthening. For this reason, it is necessary to understand the causes of damage and its influence on the structure so that a proper strengthening technique is going to be selected and used. Architectures, engineers, and scientists have to make interdisciplinary work to make it possible (Teomete 2004).

It is important to understand the behavior of masonry because, it affects both the response of structures with infill masonry walls and structures where masonry is used as the main structural material. Without having a good understanding of the structural response, it is not reasonable to repair and strengthen the structure.

Structural analysis of masonry structures has always been a problematic issue for a long time for engineers and researchers. Several techniques have been developed to understand and to predict the behavior of masonry structures. Especially, in the last decades, thanks to improvement in computational technologies, the scientific community focused on complex numerical methods instead of traditional ones (Sacco 2014).

Although masonry has a periodic arrangement of bricks surrounded by mortar, the resulting behavior is complex and anisotropic which poses difficulties as far as predictive modeling investigations are concerned. Especially under extreme loadings such as earthquakes, predicting the response of masonry structures is considered to be a challenging problem in structural mechanics. To this end, several modeling approaches have been proposed in the literature. These strategies can be categorized into two main groups as macro-scale modeling and micro-scale modeling (Lourenco 2002, Giordano, et al 2002). Micro-scale modeling is further divided into two subgroups which are detailed and simplified micro-modeling. Simplified micro-modeling is also named meso-scale modeling. (Karimian 2015). These modeling approaches will be discussed briefly in Chapter 2.

1.1. Motivation and Layout of the Thesis

The major motivation of this thesis is to investigate the seismic behavior of an ancient lighthouse on the basis of a reconstructed solid model that captures the details of the structure at the individual stone level. In order to carry out the non-linear time history

analysis under earthquake records, a meso-scale modeling strategy is preferred. After presenting some basics of the modeling approaches in Chapter 2, the mechanical properties of the masonry materials are discussed. In the next chapter, the predictive capabilities of the meso-scale modeling approach are assessed by means of two masonry wall experiments reported in the literature. The following chapter is reserved for modeling details of the lighthouse and the constitutive models used therein. The details of the time history analysis are presented in Chapter 5 including the results and main findings. In the last chapter, the main findings are recapitulated and potential future research directions are commented on.

CHAPTER 2

MASONRY MODELLING TECHNIQUES

There are a number of modeling techniques used for masonry structures that vary in accuracy, simplicity and cost. Mostly, there is an inverse proportion between the level of accuracy and simplicity. Despite of advances in available computational tools and resources, it is still necessary to make simplifications and assumptions to reduce the computational cost.

It is known that historic or modern masonry structures consist of two main components (stones, bricks as bulk units, and mortar as the binder) which have different mechanical properties. However, in most cases, homogenized models are used in Finite element method (FEM)-based modeling packages, in the form of macro modeling, to describe the behavior of masonry. This is an efficient method to model and analyze large scale masonry structures with a reasonable computational cost (Bull 2001). The examples of homogenization approach in modeling historic structures can be seen in (Al-Chaar and Mehrabi 2008; Maier, et al. 1991). In this approach, a periodic repetitive micro model of the masonry unit and mortar is extracted and used as representative equivalent volume (REV) as schematically shown in Figure 2.1. This basic cell model is used to get the anisotropic homogenized response of the material and this low cost homogenized model is used to model the whole structure. This full-scale model does not differentiate between different constituents and does not contain interfaces. Therefore, the details such as separations between units can not be observed directly. In the literature, this approach is called macro-scale modeling and is generally preferred to investigate the seismic response of large scale structures (Dolatshahi, et al. 2015). The macro-scale finite element model of Omar Toson Palace (Amer, et al. 2017) is shown in Figure 2.2 as an example of this approach.

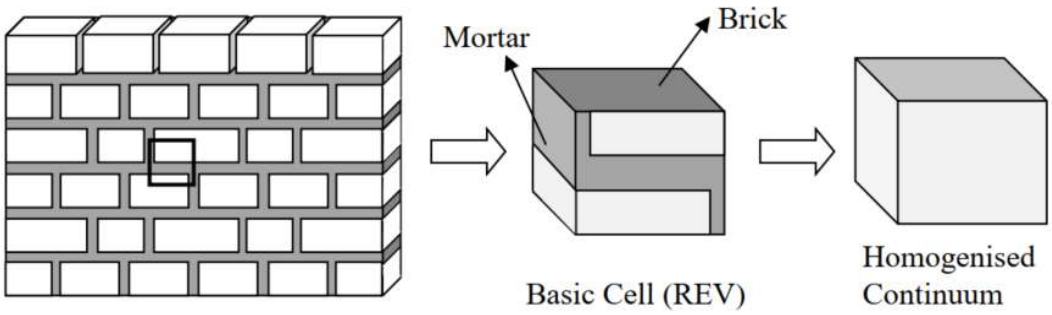

Figure 2.1: Homogenization procedure in a masonry wall (Source: Maier, et al.,1991)

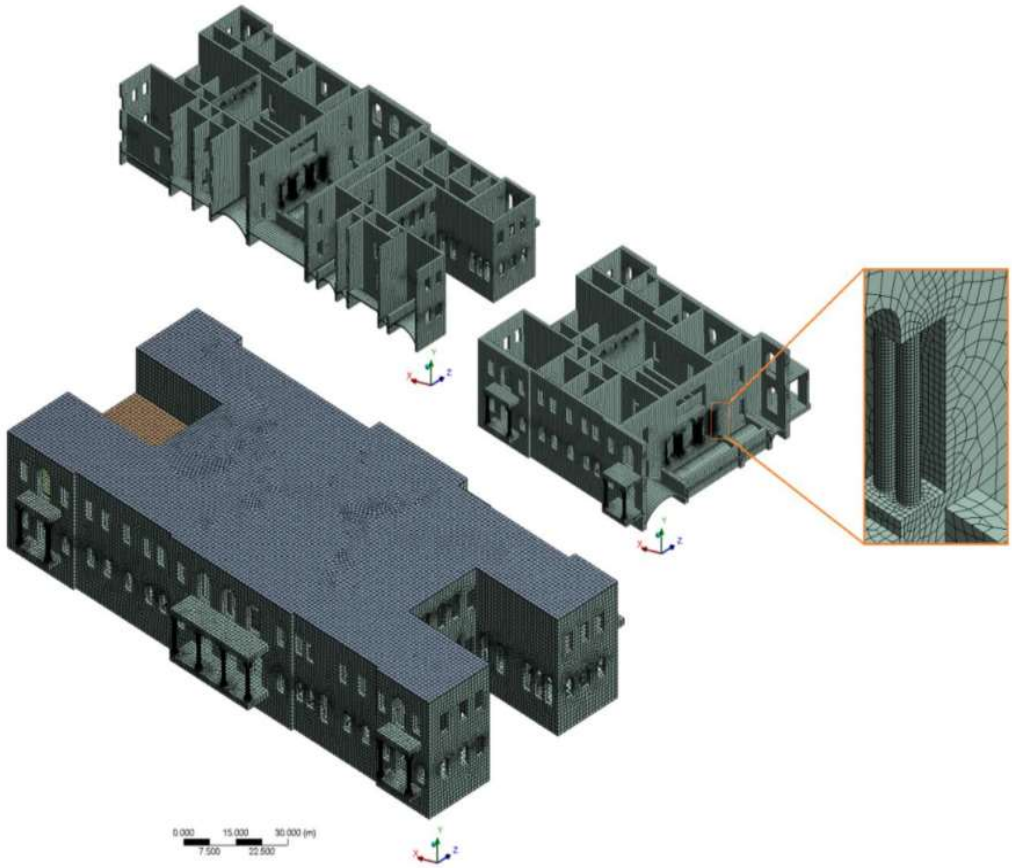

Figure 2.2: Macro-scale model of Omar Toson Palace (Source: Amer, et al. 2017)

Apart from these kinds of models, in the literature, there are more simplified macro models which try to capture the structural response by assemblies composed of springs and masses. As an example of this model, please see Figure 2.3.

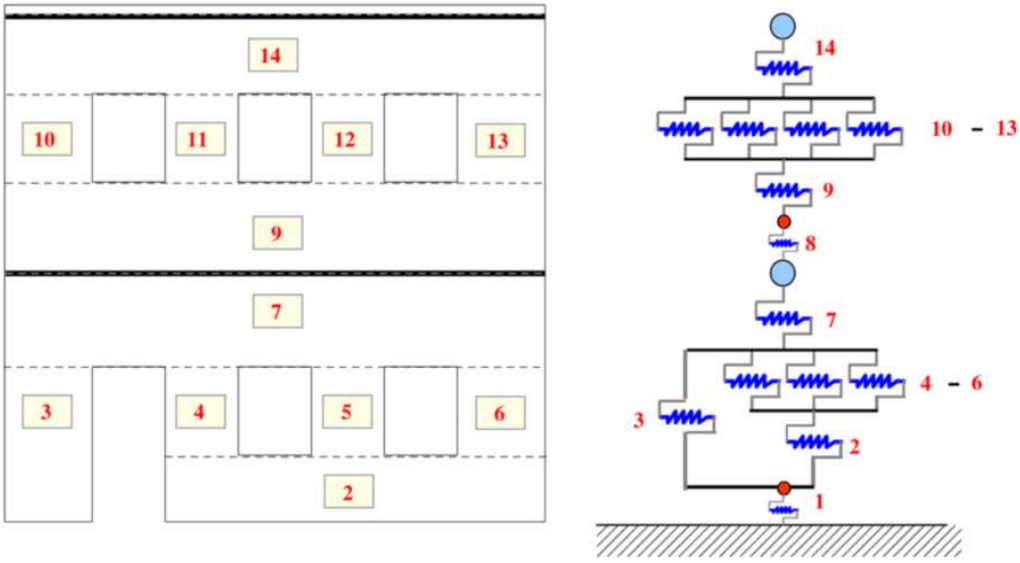

Figure 2.3: Equivalent composite spring model of an unreinforced masonry panel (Source: Park, et al. 2009)

A more realistic, yet computationally low-cost model was proposed by Pasticier et al. (Pasticier, et al. 2007) where the planes were represented by equivalent frames to perform seismic analysis. The representation of Pasticier's model can be seen in Figure 2.4

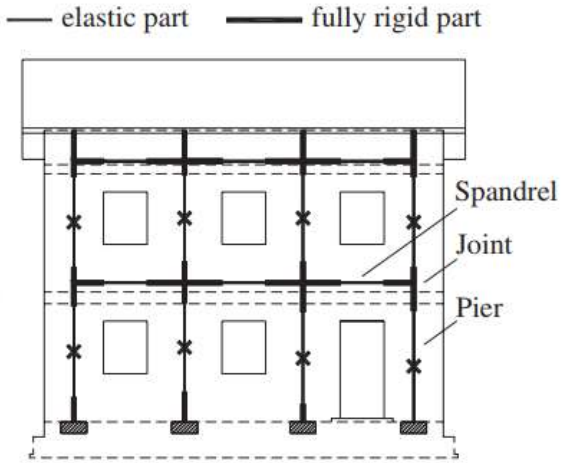

Figure 2.4: Masonry model which consists of equivalent frames (measures in meter) (Source: Pasticier, et al. 2007)

It has to be noted that the results that can be gotten from macro models are limited. The local failure mechanisms can not be observed and they are not suitable for a detailed investigation. For a better understanding of local failure mechanisms, heterogeneous models are recommended.

In a heterogeneous model, all structural units are modeled explicitly. By using the proper constitutive laws for each material of masonry, the behavior of units and interaction between them are taken into account (Theodossopoulos, et al. 2003). In the literature, there exists two different heterogeneous modeling approaches. These are called:

- Micro-Scale Modeling Approach (Detailed Micro-Scale Approach)

- Meso-Scale Modeling Approach (Simplified Micro-Scale Approach)

The major difference between these two approaches is the way mortar layers are modeled. In micro-scale modeling approach, bricks and mortar are modeled by continuum elements and the surfaces between them are represented by interface elements or cohesive contact surfaces that have the capacity to capture tensile failure modes such as rupture and sliding. The representation of the micro-scale modeling approach can be seen in Figure 2.5.

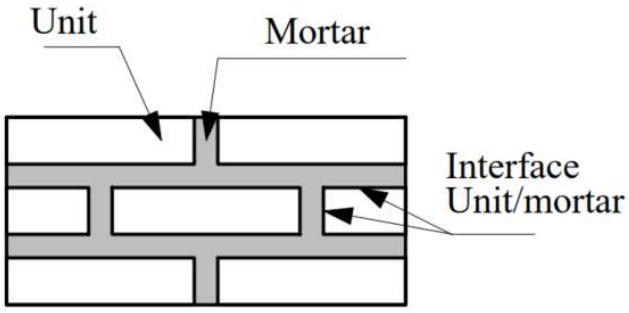

Figure 2.5: Schematic representation of micro-scale modeling in masonry (Source: Lourenco 1996).

This approach is generally used where there is a need for a detailed analysis of local behavior (Lourenco 1996). Pressure-sensitive elastoplasticity is used to represent the compressive failure in the micro-scale modeling technique. (Lourenco and Pina-

Henriques 2006) and (Abbas and Saeed 2017) are typical examples of this modelling approach and in Figure 2.6, the failure state of a wall model under in-plane lateral loading is shown.

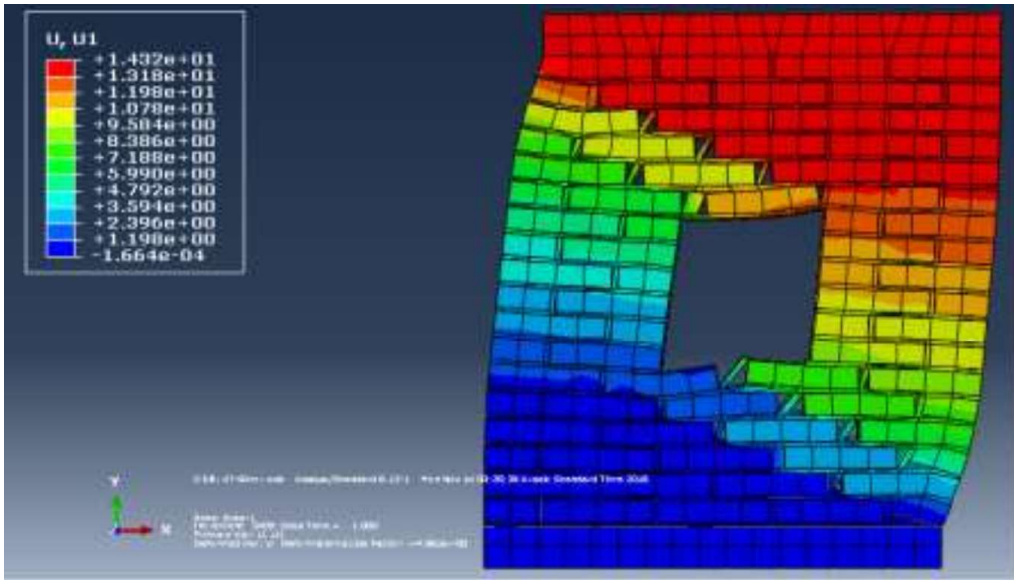

Figure 2.6: Micro model of a masonry wall under in plane loading. (Source: Abbas and Saeed 2017)

Micro-scale modelling is an effective way to get more detailed results. However, it is time-consuming both during the model preparation and analysis phases. It requires a large amount of initial data for modeling the materials and the interaction between them (Giordano, et al. 2002). The computational cost is too high compared to macro models and is not preferred especially for large and geometrically complex structures.

In meso-scale modeling, the mortar layers (joints) which include the properties of mortar and the brick-mortar interaction are lumped in interface elements or cohesive contact surfaces. The brick units are expanded and therefore local deformations, failure modes and Poisson effect of mortar can not be examined. As a result of these simplifications, the predictive capacity of the model decreases. The representation of the meso-scale modeling approach can be seen in Figure 2.7

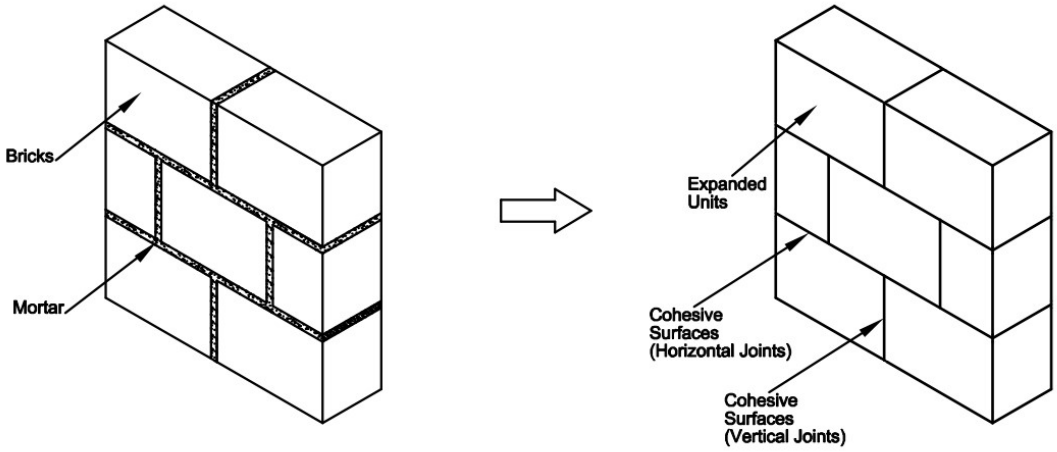

Figure 2.7: Schematic representation of meso-scale modeling.

In this approach, the cracks in bricks units can be taken into account by creating "potential crack surfaces" in bulk units by using interface elements or cohesive contact surfaces inserted typically at the middle of the brick units, see Figure 2.8. (Aref and Dolatshahi 2013).

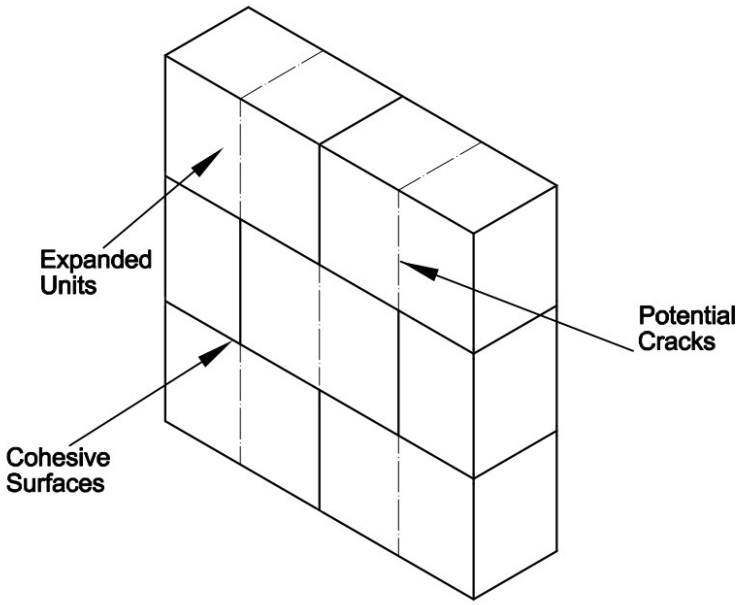

Figure 2.8: Representation of meso-scale modeling including potential cracks.

It has to be noted that, the change in the dimensions of masonry units affects the stiffness of the structure and hence it reduces the accuracy.

CHAPTER 3

MECHANICAL BEHAVIOR OF MATERIALS FOR MASONRY STRUCTURES

As mentioned before, masonry structures consist of two main materials such as units (bricks, fired clay, adobe, concrete blocks, stones) and joints (lime or cement-based mortar, bitumen, clay, and glue) (Karimian 2015). The properties of selected materials and their proportions create a variety of behavior limits. Therefore, in analyzing, designing, or repairing processes, understanding the behavior of the structural system, starts with understanding the behavior of each material.

The main materials of masonry structures are generally quasi-brittle materials and these materials are prone to show softening behavior. It means that after a critical point, the resistance of the material gradually decreases under increasing deformation. This drop is caused by internal cracks which are growing and increasing during the loading process. Voids and flaws in quasi-brittle materials exist even before loading. For example, there could be micro-cracks in mortar due to the shrinkage or micro-cracks in clay bricks that develop during the burning process. These problematic points create change in initial stiffness and strength and cause damage initiation and evolution in the material under loading. (Lourenco 1996)

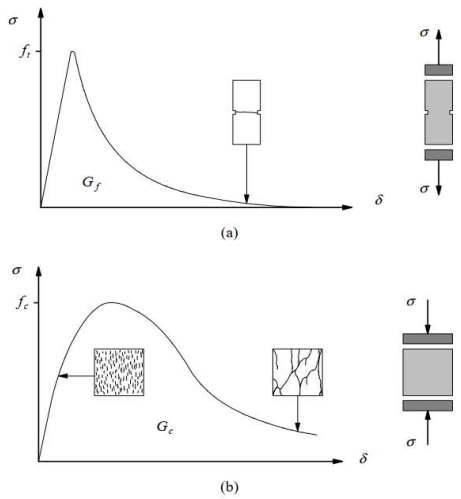

Figure 3.1: Typical behavior of quasi-brittle materials under tension (a) and compression (b) (Source: Lourenco 1996)

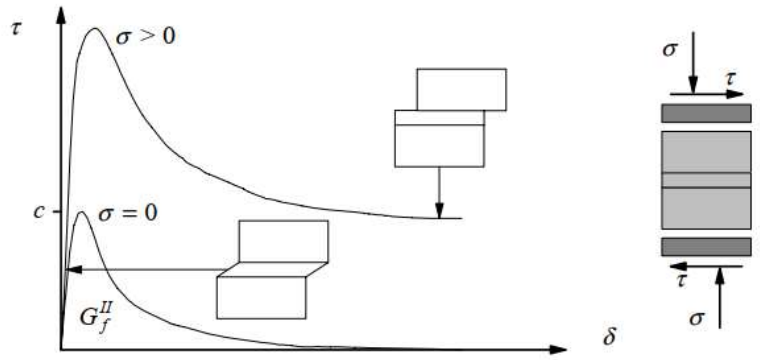

Figure 3.2: The behavior of quasi-brittle materials under shear loading with and without compression (Source: Lourenco 1996)

In Figure 3.1, the typical stress-displacement diagrams for quasi-brittle materials in uniaxial tension (a) and compression (b) are shown. Figure 3.2 shows the behavior of masonry under shear loading with and without compression. As it is seen in Figure 3.2, the increase in compressive stress increases the shear strength of masonry and affects also the failure mode. The parameters seen in Figure 3.1 and Figure 3.2 are defined in Table 3.1.

Table 3.1: Parameters in Figure 3.1 and Figure 3.2

σ:	Normal Stress	G_f:	Fracture energy (Mode I)
τ:	Shear Stress	f_c:	Compressive strength
c:	Cohesion	G_c:	Compressive fracture energy
δ:	Displacement	G_f^{II}:	Fracture energy (Mode II)
f_t:	Tensile strength		

3.1. Failure Modes of Masonry

As both types of masonry structures (units and binders) are weak in tension, a tensile failure in masonry units is highly expected especially under extreme loadings such as earthquakes. It makes the Mode I failure an essential issue to investigate. A displacement controlled test in small masonry specimens of solid clay and calcium-silicate units was done by Van der Pluijm in 1992, see Figure 3.3. An exponential tension

softening curve with a mode I fracture energy (G_f^I) between 0.005 and 0.2 (N.mm/mm^2) and tensile strength between 0.3 and 0.9 (N/mm^2) were found from these tests. (Pluijm 1992).

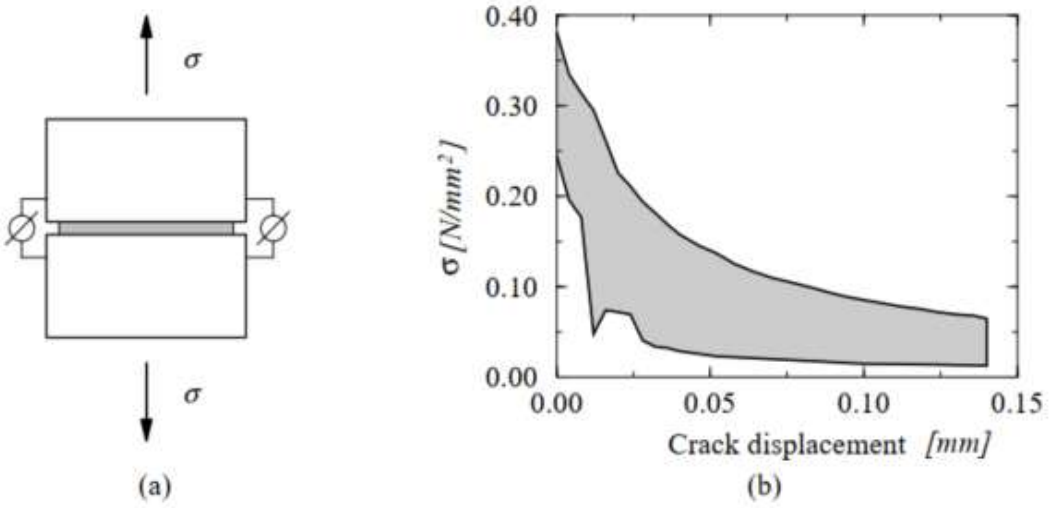

Figure 3.3: (a) Test specimen; (b) stress-crack displacement graph for solid clay brick masonry (the shaded area is for envelope results of 3 tests) (Source: Pluijm 1992)

Another essential issue is the behavior of masonry assemblage under shear force. An experiment is carried out by Van der Pluijm in 1993 to see the response of masonry joints under shear force, see Figure 3.4 and Figure 3.5. The results of the experiments suggest that, mode II fracture energy (G_f^{II}) varies between 0.01 to 0.25 (N.mm/mm^2) and the cohesion values are in the range of 0.1 to 1.8 (N/mm^2) (Pluijm 1993). Maximum and minimum values for mode I and mode II are tabulated in Table 3.2.

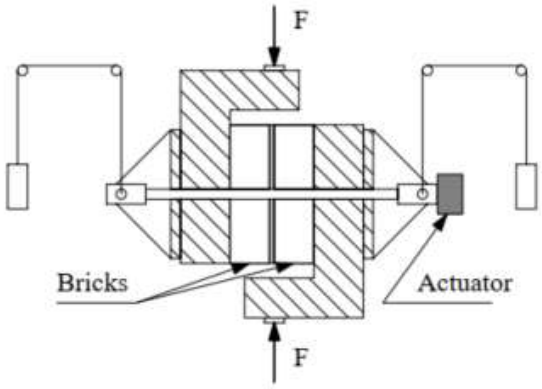

Figure 3.4: Test setup for shear response of masonry assemblage (Source: Pluijm 1993)

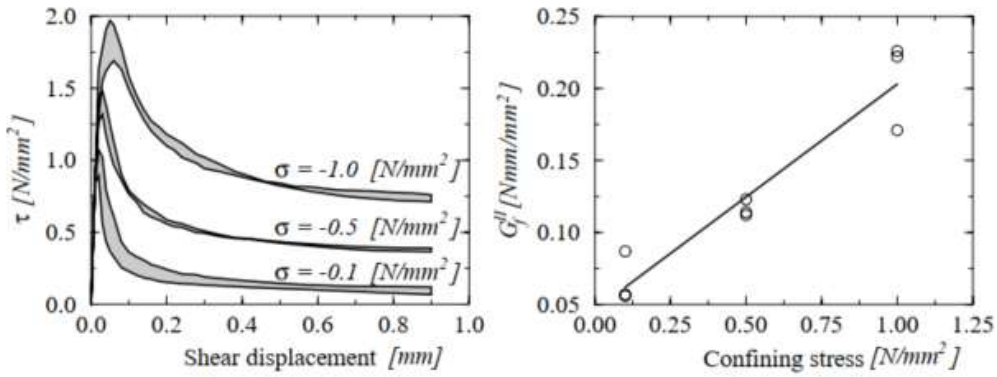

Figure 3.5: Behavior of the joints for solid clay units under shear loading (Source: Pluijm 1993)

Table 3.2: Maximum and minimum parameters for mode I and mode II failures.

Mode	Fracture Energy (N.mm/mm^2)		Strength (MPa)	
	Maximum	Minimum	Maximum	Minimum
Mode I	0.2	0.005	0.9	0.3
Mode II	0.25	0.01	1.8	0.1

As mentioned previously, the dependency of shear strength on the compressive stress can be seen in Figure 3.5. The increase in compressive stress affects the shear strength of masonry directly.

In masonry with low tensile bond strength, tensile failure generally occurs between the bed joints and the units when the tensile loading is perpendicular to the bed joints. It could be said that, in such kind of situations, the masonry tensile strength can be assumed as equal to tensile bond strength between the joint and the unit. However, if a binder with high strength and units with low tensile strength were used, tensile failure may occur in the unit. In this case, the tensile strength of the masonry can be equated to the tensile strength of the unit. (Lourenco 1996)

In 1985, a study was conducted by Backes (Backes 1985) to investigate the tensile strength of masonry, see Figure 3.6 and Figure 3.7. In these experiments, both failure types (failure in joints and failure in units) were observed.

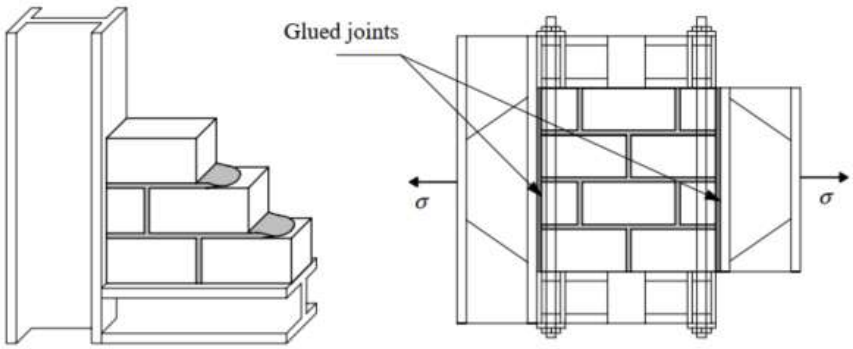

Figure 3.6: The set-up to investigate the tensile strength of masonry (Source: Backes 1985)

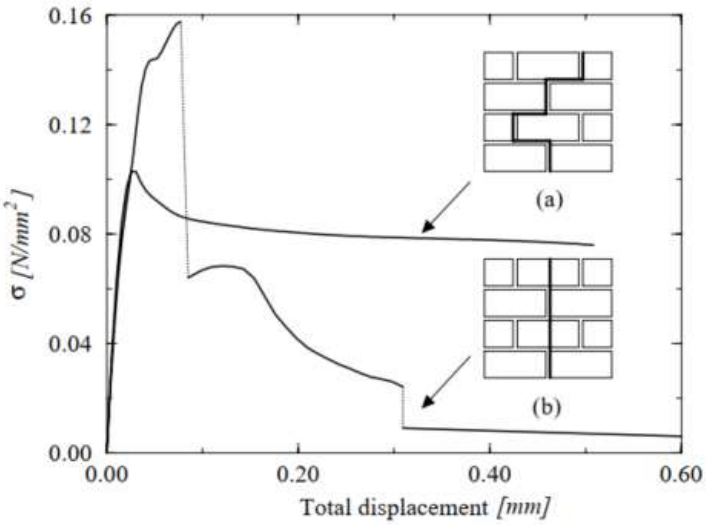

Figure 3.7: Results for both types of failures: (a) tensile failure in bed joints; (b) tensile failure in units (Backes 1985)

The compressive strength of masonry is highly influenced by the constituent elements. The main factor affecting the limits of masonry structures under compression is the difference in elastic properties of unit and mortar. (Lourenco 1996)

In historic masonry, there is a variety of compressive strength because of the different ratios of raw materials. As an example, in raw materials of clay brick units, the number of stones can increase the compressive strength of the masonry structure. The compressive strength of masonry is generally tested by using ‘stacked bond prism’, which is shown in Figure 3.8. (Lourenco 1996)

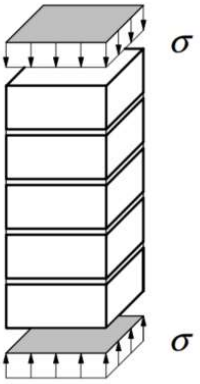

Figure 3.8: Schematic representation of ‘stacked bond prism’(Source: Lourenco 1996)

CHAPTER 4

INVESTIGATING THE CAPABILITIES OF MESO-SCALE MODELLING APPROACH

In this thesis, the meso-scale modeling approach which includes elastic and plastic properties of units and traction-separation laws embedded in cohesive contact surfaces and frictional contacts are utilized for modeling. Before the use of the meso-scale modeling approach to investigate the lighthouse, two different experiments on masonry walls were modeled to investigate the capabilities of this modeling approach. The first experiment was conducted by Rajimakers and Vermeltfoort (Rajimakers and Vermeltfoort 1992) to investigate the in-plane behavior of a masonry wall. In the second one, the out-of-plane behavior of a C-Shaped masonry wall investigated by Griffith and Vaculik (Griffith and Vaculik 2007).

Those experiments were also referred to (Abdulla, et al. 2017) using a meso-scale modeling approach. As a difference, in (Abdulla, et al. 2017), to capture cracks within bricks, the extended finite element method (XFEM) was used whereas this study has not taken this feature into account.

After validating the models by comparing with the experimental results, a parametric study was conducted to investigate the influence of different material and geometric parameters of the models.

4.1. Mechanical Behaviors of Units in Finite Element Models

Herein the constitutive models for modeling the behavior of units in 3D are described to a certain extent. In the validation phase and the modeling of the lighthouse, these constitutive models are used.

4.1.1 Elastic Behavior of Expanded Units

It is needed to adjust the elastic modulus of the expanded units to have a matched response with the masonry wall which includes units and mortar. The geometry and

elastic moduli of mortar and unit affect the adjusted elastic modulus. The following equation is used to calculate adjusted elastic modulus; (Abdulla, et al. 2017).

$$E_{adj} = \frac{HE_uE_m}{nh_uE_m + (n-1)h_mE_u} \tag{4.1}$$

The parameters of this equation are shown in Figure 4.1 and defined as:

E_{adj}: Adjusted elastic modulus of masonry assemblage (MPa)

H: Height of masonry assemblage (mm)

E_u: Elastic modulus of units (MPa)

E_m: Elastic modulus of mortar (MPa)

n: number of courses in a masonry assemblage

h_m: thickness of mortar (mm)

h_u: height of a unit (mm)

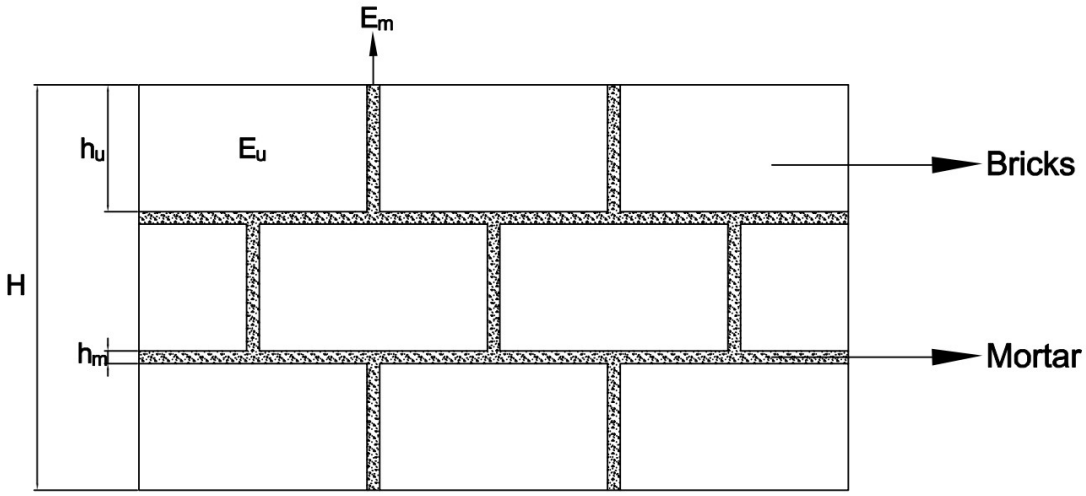

Figure 4.1: Schematic representation of a masonry assemblage.

4.1.2 Plastic Behavior of Expanded Units

An extended version of the Drucker-Prager plasticity model (Drucker and Prager 1952) is utilized to represent the inelastic behavior of masonry under compression. Drucker-Prager model (DP) is the generalization of the Mohr-Coulomb yield criterion to predict the onset of plasticity in frictional materials, such as soils and rocks.

The version available in ABAQUS is called Drucker-Prager/Cap model. Drucker-Prager yield surface is written as:

$$F_S = t - p\tan\beta - d = 0 \tag{4.2}$$

where β is the angle of friction, d is the cohesion of the material, and t is a deviatoric stress measure defined as:

$$t = \frac{q}{2}\left[1 + \frac{1}{K} - \left(1 - \frac{1}{K}\right)\left(\frac{r}{q}\right)^3\right] \tag{4.3}$$

where K is a material parameter that should satisfy $0.778 \leq K \leq 1.0$. By means of t, it is possible to capture the tension-compression asymmetry which is typically observed in frictional materials. Von Mises equivalent stress q and the third invariant of the stress tensor r are defined as:

$$q = \sqrt{\frac{3}{2}(\mathbf{S}:\mathbf{S})} \qquad r = \left(\frac{9}{2}\mathbf{S}.\mathbf{S}:\mathbf{S}\right)^{1/3} \tag{4.4}$$

Furthermore, $\mathbf{S}$ is the stress deviator,

$$\mathbf{S} = \sigma + p\mathbf{I} \tag{4.5}$$

where the hydrostatic pressure p is defined as:

$$p = -\frac{1}{3}\mathrm{trace}(\boldsymbol{\sigma}) \tag{4.6}$$

When K is taken as unity, the model reduces to the Von-Mises plasticity model. In Figure 4.2 the section of the yield surface on the p-t plane is shown.

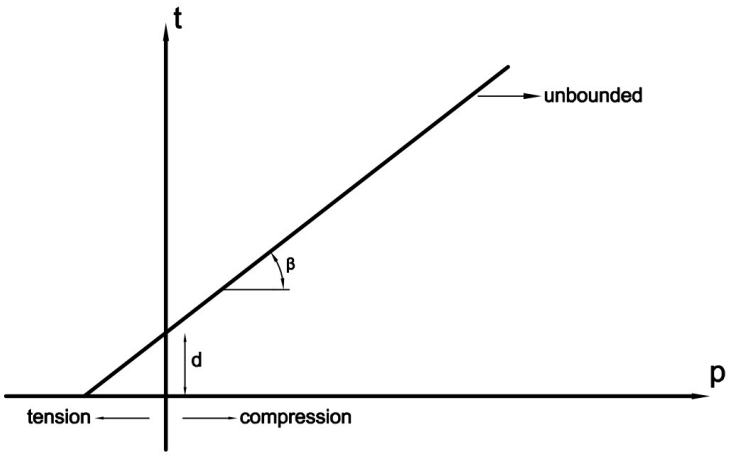

Figure 4.2: The section of the yield surface

On the compression side, the yield surface is unbounded which is not physically meaningful. To account for the limited strength on the compressive side, a cap is introduced and added to the shear dominated failure surface by a smooth transition region as shown below, see Figure 4.3.

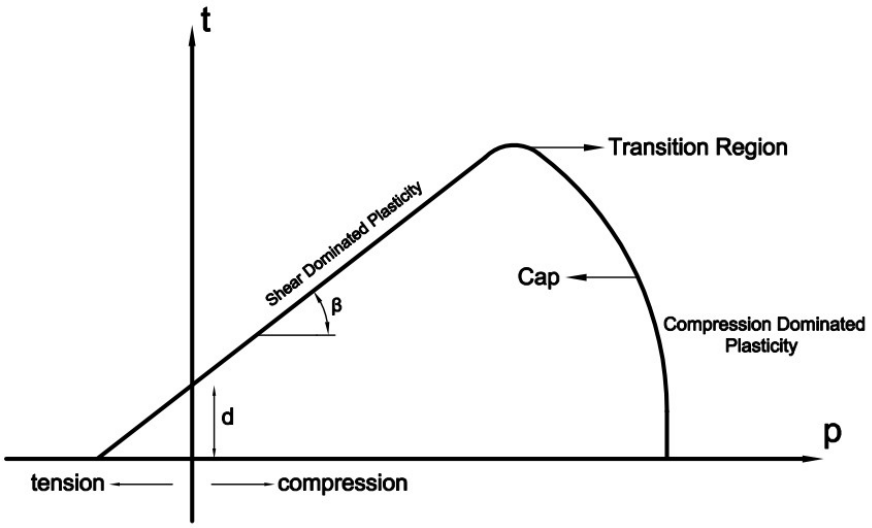

Figure 4.3: Section of yield surface with a cap

The cap portion has an elliptical shape and can harden or soften as a function of the volumetric plastic strain, defined as:

$$\varepsilon_{\mathrm{V}}^{pl} = \varepsilon_{\mathrm{xx}}^{pl} + \varepsilon_{\mathrm{yy}}^{pl} + \varepsilon_{\mathrm{zz}}^{pl} \tag{4.7}$$

The cap yield surface is written as:

$$F_c = \sqrt{(\mathrm{p} - \mathrm{p}_\alpha)^2 + \left[\frac{Rt}{(1 + \alpha - \frac{\alpha}{\cos\beta}}\right]^2} - R(d + p_\alpha tan\beta) = 0 \qquad (4.8)$$

where R is a material parameter controlling the cap shape and p_α is an evolution parameter that represents the volumetric plastic strain (ε_V^{pl}) driven hardening/softening. The hardening/softening law is a user-defined piecewise linear function relating the hydrostatic compression yield stress (p_b) to the volumetric plastic strain. The explicit form of p_α is:

$$p_\alpha = \frac{p_b - Rd}{(1 + \mathrm{R}\tan\beta)} \qquad (4.9)$$

α appearing in Eq. (4.8) is a small parameter ([0.01-0.05]) used to define a smooth transition surface, F_t, between the shear surface and the cap, expressed as:

$$F_t = \sqrt{(\mathrm{p} - \mathrm{p}_\alpha)^2 + \left[t - (1 - \frac{\alpha}{cos\beta})(d + p_\alpha tan\beta)\right]^2} - \alpha(d + p_\alpha tan\beta) = 0 \qquad (4.10)$$

The yield surfaces of the Modified Drucker-Prager/Cap model is shown in Figure 4.4.

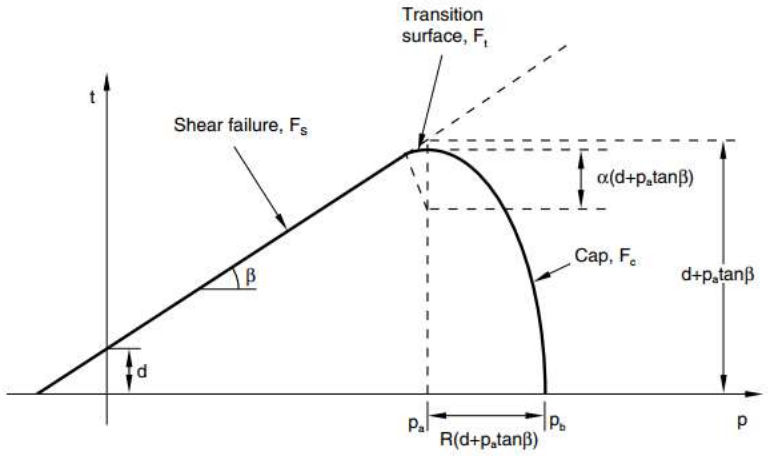

Figure 4.4: Yield surfaces of Modified Drucker-Prager/Cap model in the p-t plane (Source: ABAQUS 2013)

4.2. Mechanical Behavior of Joints in Finite Element Models

As mentioned before, the mechanical behavior of mortar layers is lumped into cohesive contact surfaces. These are special failure planes which are defined by a pair of surfaces without any gap between them.

For example, in case of a double cantilever beam test (DBCT), see Figure 4.5, which is commonly used to measure the fracture energy, the fracture propagates within the failure plane. To model this failure mode in a finite element setting, interface elements are embedded within the potential failure surface.

Upon mechanical loading, the surfaces defining the failure plane detach and opens in a progressive manner. In quasi-brittle materials, the progressive opening requires lower traction (force per unit area) values with significant energy dissipation. Depending on the material, different responses of failure planes are possible as schematically shown in Figure 4.6. Furthermore, opening in normal direction is not the only failure mode and as shown in Figure 4.7, sliding of the cohesive surfaces in tangential directions may take place. It is to be noted that under realistic loading conditions, the failure mode is of mixed-mode type.

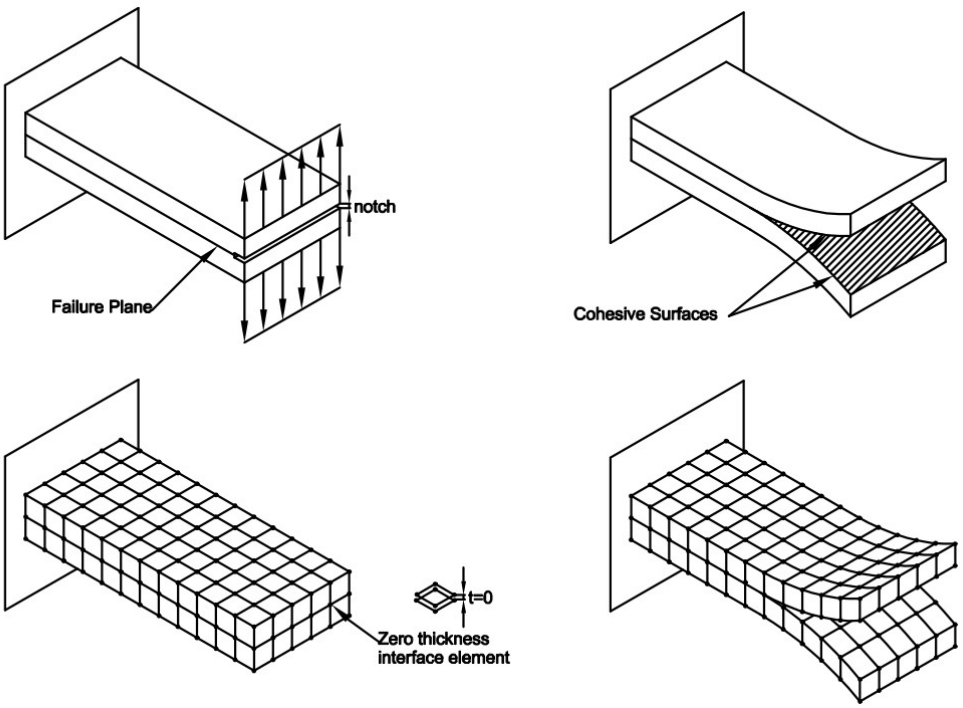

Figure 4.5: Schematic representation of DCBT modeling.

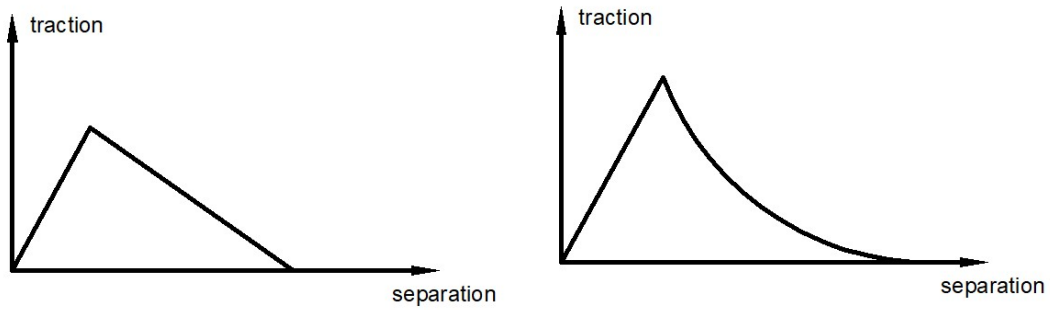

Figure 4.6: Different response of quasi-brittle materials under tensile loads.

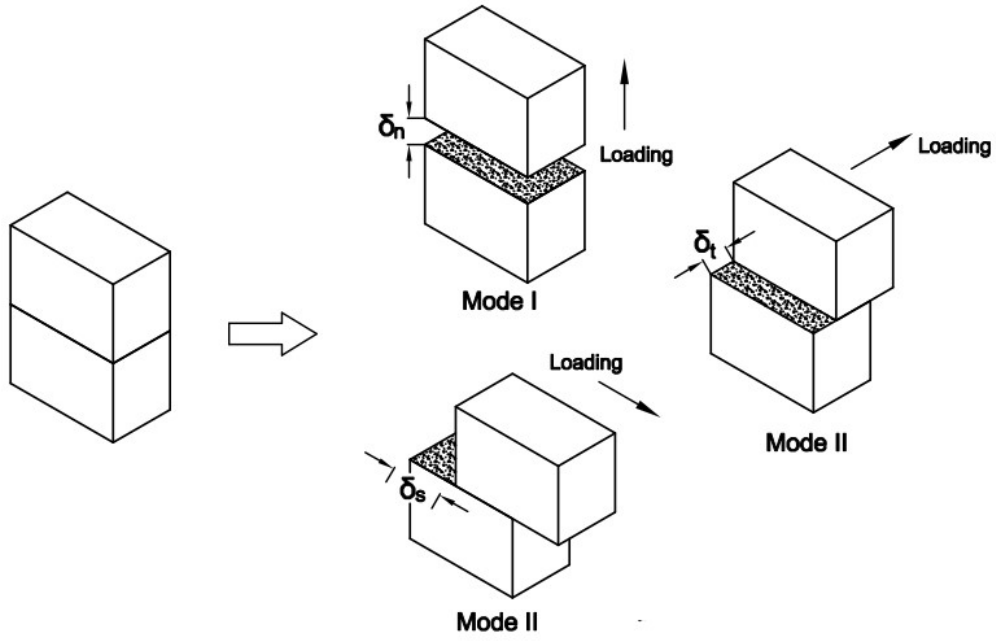

Figure 4.7: Schematic representation of failures in different modes

Nonlinear behavior of cohesive surfaces is described by traction-separation relations which are composed of an elastic part and an inelastic part. First, the elastic part is going to be addressed and then inelasticity in the form of damage is going to be introduced.

4.2.1. Elastic Behavior of Joints

Before damage initiation, the response of joints is elastic and the traction components are written as:

$$\mathbf{t} = \begin{Bmatrix} t_n \\ t_s \\ t_t \end{Bmatrix} = \begin{bmatrix} K_{nn} & 0 & 0 \\ 0 & K_{ss} & 0 \\ 0 & 0 & K_{tt} \end{bmatrix} \begin{Bmatrix} \delta_n \\ \delta_s \\ \delta_t \end{Bmatrix} = \boldsymbol{K\delta} \tag{4.11}$$

where **t** is the nominal traction vector, **K** is the elastic stiffness matrix and **δ** is the separation vector. It is obvious that there is no coupling between the opening modes since all the off-diagonal terms are zero.

The components of the stiffness matrix should be adjusted to have the same stiffness values of the original masonry joint interfaces. This calculation is done by using the following equations as proposed by (Abdulla, et al 2017).

$$K_{nn} = \frac{E_u E_m}{h_m(E_u - E_m)} \tag{4.12}$$

$$K_{ss}, K_{tt} = \frac{G_u G_m}{h_m(G_u - G_m)} \tag{4.13}$$

4.2.2 Inelastic Behavior of Joints

The inelastic behavior and failure of cohesive surfaces are described by using the damage mechanics approach which requires damage initiation and evolution criterion. The damage initiation criterion is based on the tensile and shear strength of the interface and is defined by the user. Once the damage initiation is reached, softening sets in, and "cohesive cracking" propagates along the interface until complete failure. In Figure 4.8, the typical traction-separation response of a quasi-brittle material is shown in linear form. The shaded area represents the dissipated energy by damage in cohesive surfaces under unloading/reloading cycles.

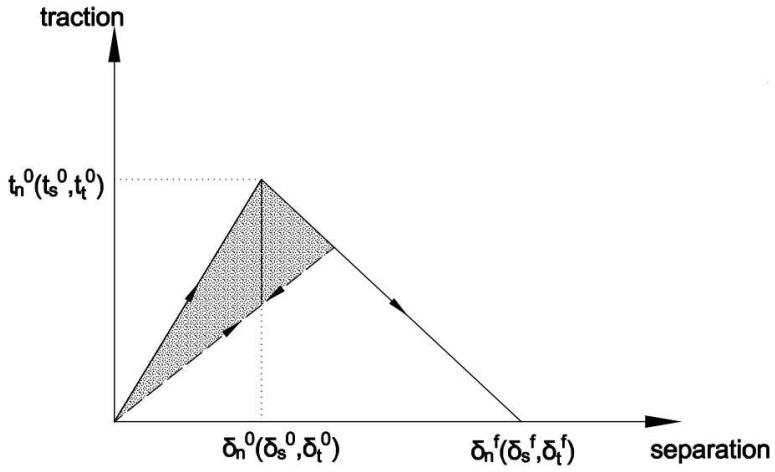

Figure 4.8: Typical traction-separation response

In this work, the quadratic stress criterion is used to define damage-initiation. The explicit form of this criterion is written as:

$$\left(\frac{t_n}{t_n^0}\right)^2 + \left(\frac{t_s}{t_s^0}\right)^2 + \left(\frac{t_t}{t_t^0}\right)^2 = 1 \tag{4.14}$$

where t_n^0 is the normal tensile strength. It is taken as equal to the normal strength of masonry joints. t_s^0 and t_t^0 are the shear strengths of the interface and they are dependent on compressive stresses developing on the interface. The ultimate shear strengths are described by a Mohr-Coulomb type failure equation as:

$$\begin{aligned} t_s^0 &= c + \mu\, \sigma_n \\ t_t^0 &= c + \mu\, \sigma_n \end{aligned} \tag{4.15}$$

When these critical values are reached, it is assumed that mode II type failure is reached and the remaining resistance is only due to friction and the critical shear stress value for sliding τ_{sliding} is expressed as:

$$\tau_{\text{sliding}} = \mu\, \sigma_n \tag{4.16}$$

In other words, after mode II failure, if the shear stress in the failed joints is larger than the critical sliding value, τ_{sliding}, the units slide relative to each other. Quadratic

stress criterion is reported to be an effective way to predict damage initiation of masonry joints under mixed-mode loading (Campilho, et al. ,2018).

After the damage initiation criterion is reached, the stiffness of the masonry joints decreases because of crack propagation which causes a reduction in strength and failure of joints. After the damage starts to evolve, the tractions are evaluated from,

$$\mathbf{t} = (1 - D)\boldsymbol{K}\delta \tag{4.17}$$

where D is the damage variable which takes a value between 0 and 1. In other words, the stiffness of the interface is reduced by (1-D) The evolution of D controls the traction-separation law and in this work, a linear damage evolution law;

$$\mathrm{D} = \frac{\delta_{\mathrm{eff}}^{f}(\delta_{\mathrm{eff}}^{max} - \delta_{\mathrm{eff}}^{0})}{\delta_{\mathrm{eff}}^{max}(\delta_{\mathrm{eff}}^{f} - \delta_{\mathrm{eff}}^{0})} \tag{4.18}$$

is used where the effective separation, δ_{eff}, and the effective separation at the complete failure, $\delta_{\mathrm{eff}}^{f}$, are given by,

$$\delta_{\mathrm{eff}} = \sqrt{\delta_{\mathrm{n}}^{2} + \delta_{\mathrm{s}}^{2} + \delta_{\mathrm{t}}^{2}} \tag{4.19}$$

$$\delta_{\mathrm{eff}}^{f} = \frac{2G^{C}}{t_{\mathrm{eff}}^{f}} \tag{4.20}$$

respectively with t_{eff}^{f} as the effective traction at damage initiation. The effective separation corresponding to the initiation of damage is represented by $\delta_{\mathrm{eff}}^{0}$ and the maximum effective separation reached throughout loading history is given by $\delta_{\mathrm{eff}}^{max}$.
The critical mixed-mode fracture energy, G^{C}, is obtained from Benzeggagh-Kenane (BK) law (Benzeggagh and Kenane 1996) which is extensively used in the literature, (Abdulla, et al. 2017). This is considered to be an effective way since the critical energies of both tangential directions are the same, (Abdulla, et al. 2017). The exponent in equation 4.21,

η, is taken as 2 since the bricks are brittle (Benzeggagh and Kenane 1996). According to the BK law, G^C is expressed as:

$$G^C = G_n^C + (G_s^C - G_n^C)\left(\frac{G_s}{G_T}\right)^{\eta} \tag{4.21}$$

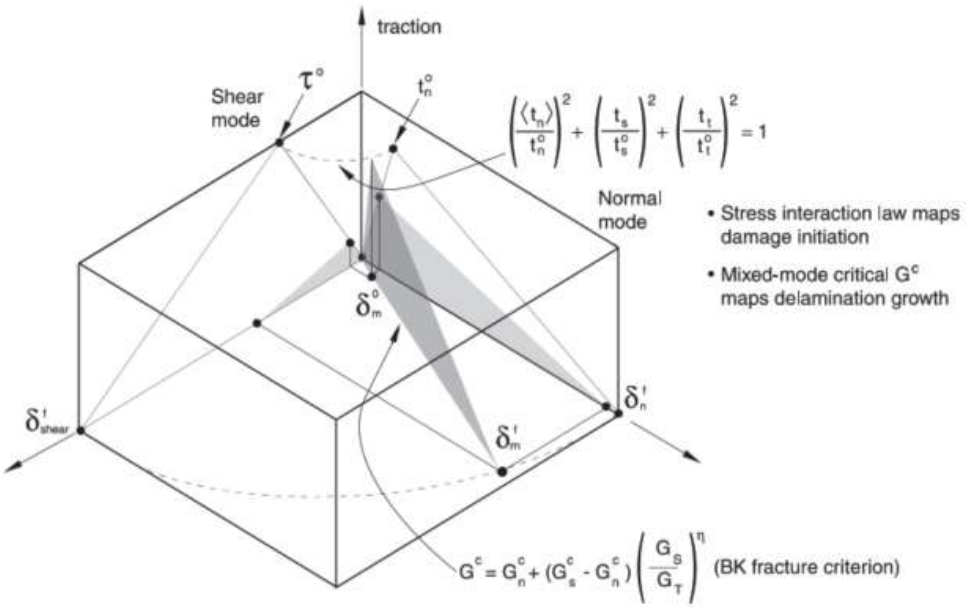

Figure 4.9: Mixed-mode response in cohesive elements. (Source: ABAQUS 2013)

For a traction-separation response with isotropic shear behavior, Figure 4.9 is an illustration of the dependency of damage initiation and evolution on mode mixity. Figure 4.9 displays the traction on the vertical axis and the values of the tensile (normal) and tangential (shear) separations along two horizontal axes. The unshaded triangles show the pure deformation cases under shear and normal excitation. To represent the mixed-mode cases, shaded triangles are used.

4.3. Meso-Scale Modelling of a Wall: In Plane Behavior

The experimental work of Rajimakers (1992) is used as a reference to validate the finite element model. Since the report of the experiment is not accessible, all the information about the experimental setup, loading protocol and results are obtained from (Abdulla, et al. 2017).

The dimensions of the wall are shown in Figure 4.10. The wall consists of 18 layers of bricks each of which are 210 mm in length, 52 mm in height and 100 mm in thickness. They were aligned in a row and bonded with mortar of 10 mm thickness. The mortar includes cement, lime and sand with a volumetric ratio of 1:2:9, respectively. The wall was restrained from the top and bottom face by means of steel profiles. Pressure was applied from the top as shown in Figure 4.10 and kept constant throughout the loading history. After it has reached its maximum value, the top steel profile is pushed horizontally.

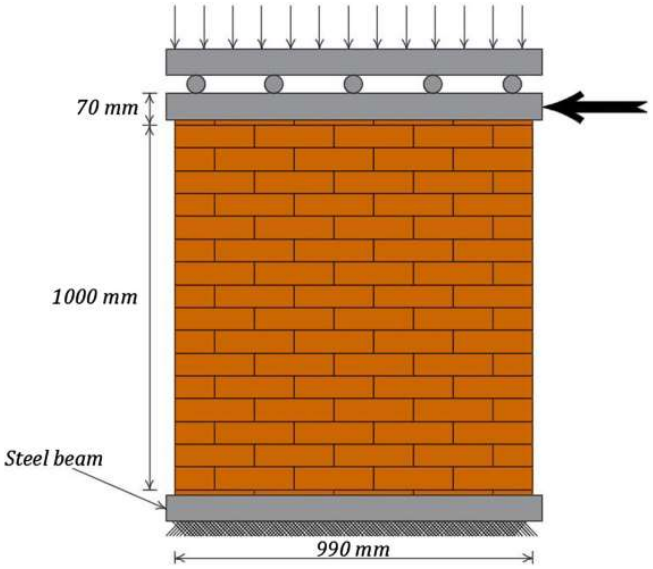

Figure 4.10: Wall tested by Rajimakers and Vermeltfoort (Source: Abdulla, et al. 2017).

There were three shear walls (J4D, J5D, and J6D) in this experiment. Compressive stress of 0.3 MPa was applied on J4D and J5D, whereas this value was raised to 1.21 MPa for J6D. Then the walls were pushed 4 mm horizontally from the right end of the top steel profile. In the following section, the wall named J4D is modeled. (Abdulla, et al. 2017).

4.3.1. Finite Element Model

First the geometry of the wall is created and divided into 18 layers. Each layer is divided into 4.5 bricks and the overall layout of the brick arrangement matches to that of the tested wall. In order to ease the model preparation phase, an external program is used which detects the interactions between bricks and assigns surface-to-surface contacts

between them in an automatic manner. This reduces the time needed to prepare the model. The model at two different stages are shown in Figure 4.11.

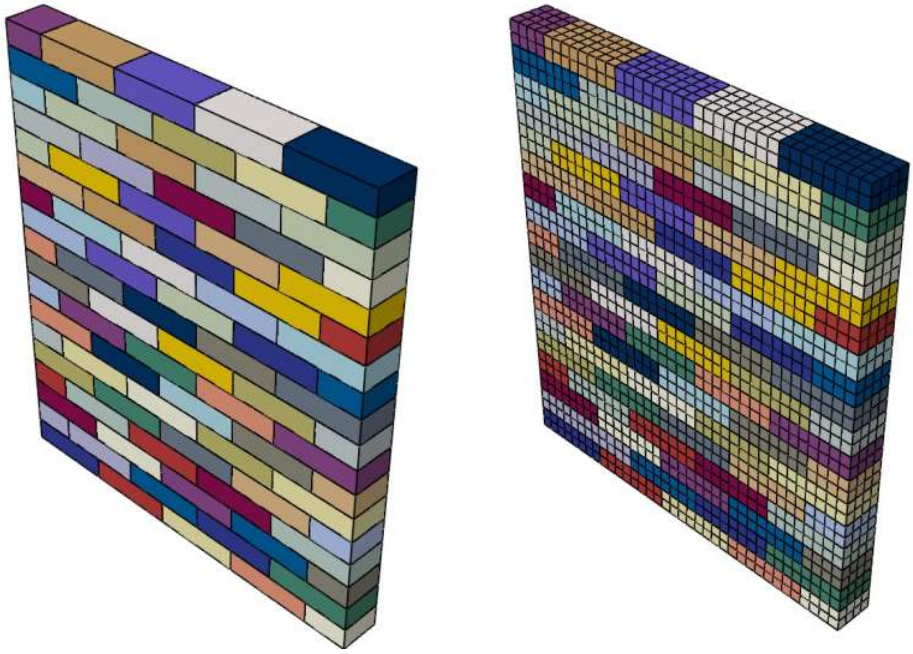

Figure 4.11: Finite element model of the shear wall using bricks with different sections

After that, the parameters which are given in Table 4.1 is used to see if the modeling approach has the capability to simulate the in-plane behavior of the masonry wall. In addition to that parameters, as mentioned before, the non-linear behavior of bricks under compression is defined by using Drucker Prager/Cap model. To define Drucker Prager/Cap model, it is needed to have the absolute plastic strain values and corresponding yield stress values under compression. Therefore, the elastic strain values are extracted from the total axial strain values by using the modulus of elasticity of the expanded units, see Figure 4.12.

Table 4.1: The parameter tables for units and cohesive surfaces (Source: Abdulla, et al. 2017)

Units	
E_{brick} (MPa)	16700
ν	0.15
E_{mortar} (MPa)	780
E_{adj} (MPa)	4050
Flow Stress Ratio, R	1
Friction Angle, β	36
Dilatation Angle, ψ	13

Joints	
K_{nn} (N/mm^3)	82
K_{ss} (N/mm^3)	36
K_{tt} (N/mm^3)	36
t_n^{max} (MPa)	0.25
G_{IC} (N/mm)	0.018
c (MPa)	0.35
μ	0.75
G_{IIC} (N/mm)	0.125

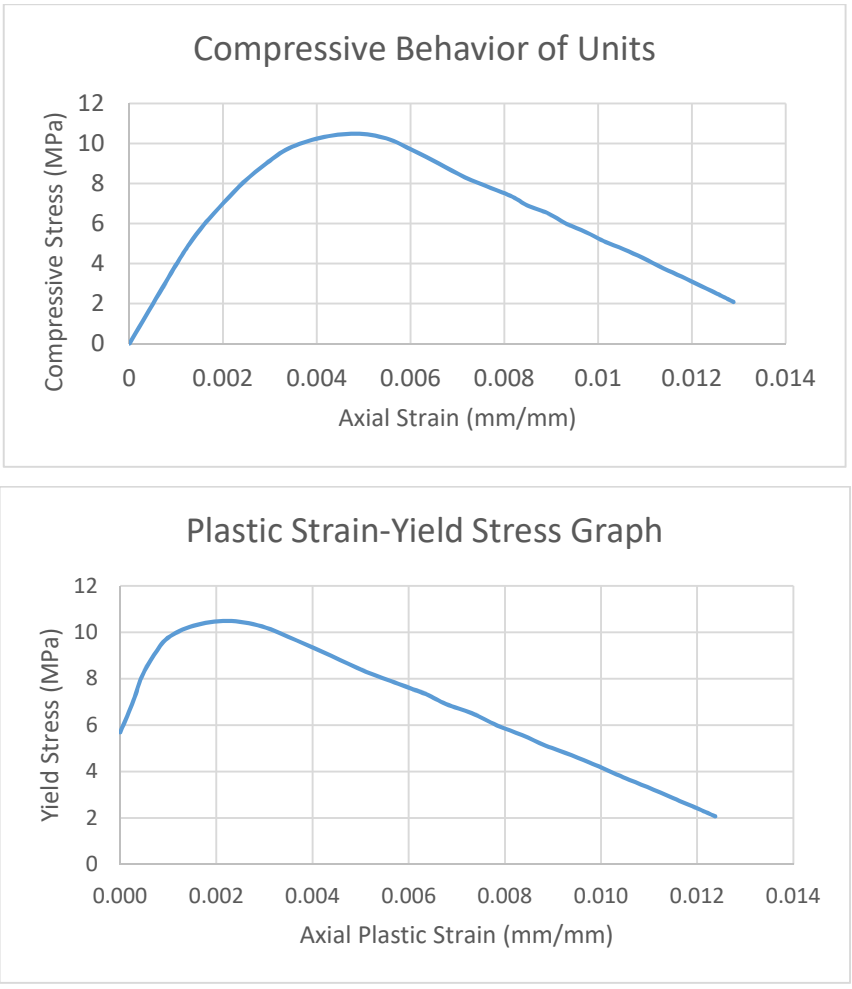

Figure 4.12: Compressive behavior of bulk units and plastic strain-yield stress graph (Source: Abdulla, et al. 2017)

The nodes at the bottom part of the wall and the side surface of the corner brick was simply supported. For simulating the initial stress, an equivalent displacement value (0.12 mm) applied to the top part of the wall and kept constant throughout the loading history. After that, 4 mm of lateral displacement was applied to the top surface of the wall. These boundary conditions and loading protocol can be seen in Figure 4.13. Dynamic time history analyses were conducted by using direct implicit time integration algorithm (Hilber-Hughes-Taylor) of ABAQUS with built-in integration parameters. In all analyses, adaptive time increments were used. Initial increment size, minimum increment size and maximum increment size are selected as $2x10^{-11}$, $1x10^{-11}$, and 0.005 respectively.

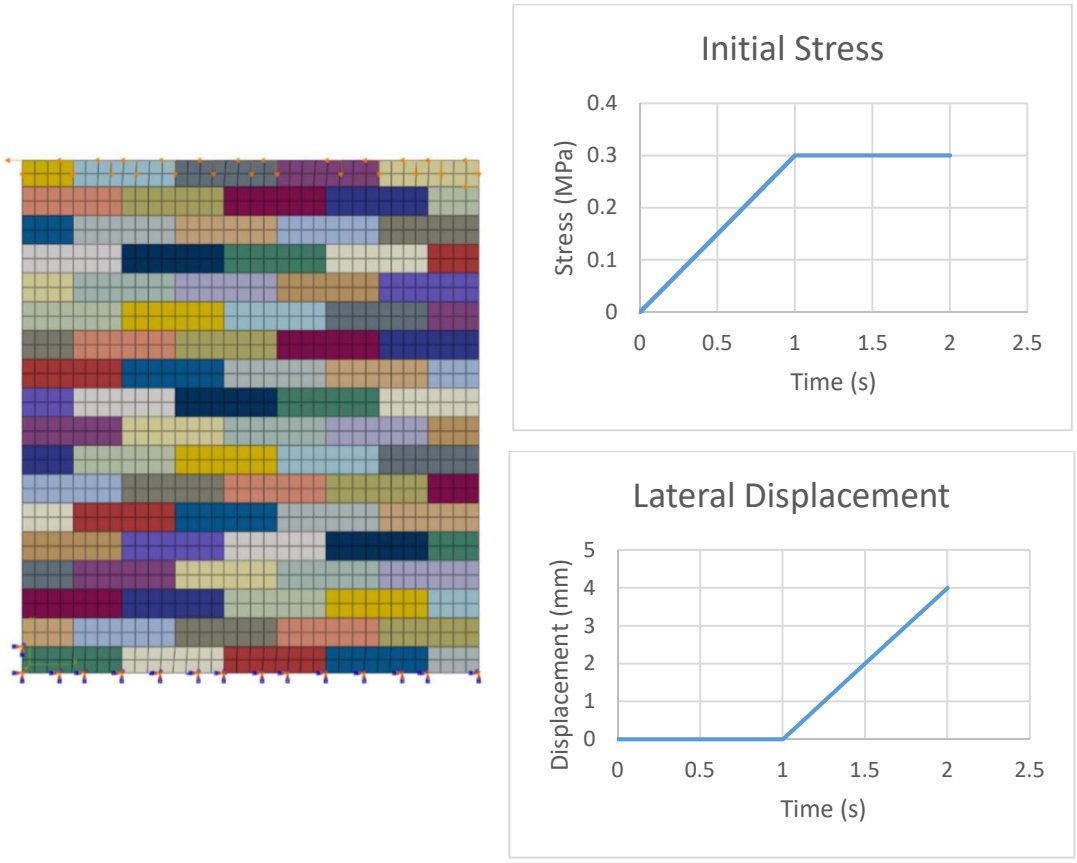

Figure 4.13: Boundary Conditions and Loading Protocol

The finite element model consists of 5184 linear hexahedral elements (C3D8). Viscous regularization which responds roughly to numerical damping, is used to avoid the convergence problems. As the viscosity parameter, 0.002 is used to reproduce the results in (Abdulla, et al. 2017).

4.3.2. Results

In Figure 4.14, the failure pattern obtained from the finite element analysis and the experimental results are compared. Both have a diagonal crack that starts from the point where the lateral load is applied. In addition to this good agreement in failure pattern, force-displacement graphs are presented in Figure 4.15.

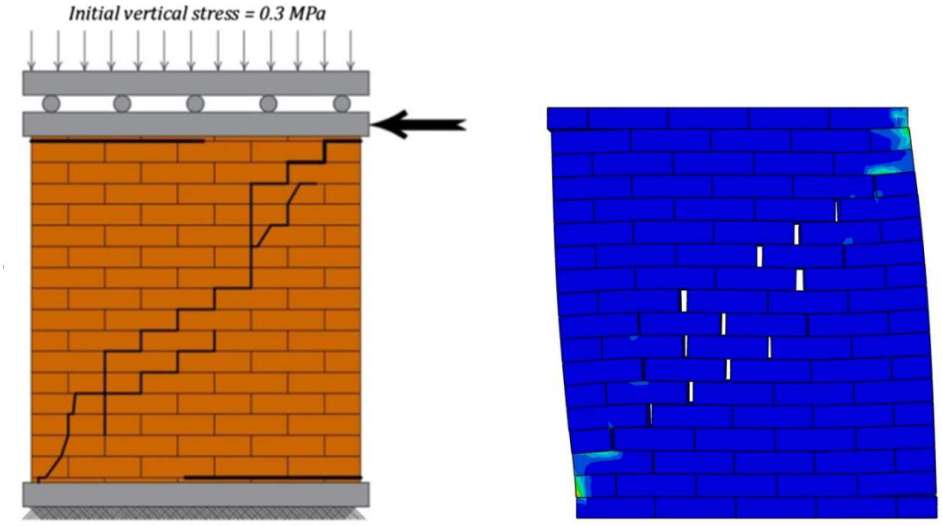

(a) (b)

Figure 4.14: Comparison of failure patterns: (a) experimental (Source: Abdulla, et al. 2017); (b) Finite element model with plastic strain concentrations (scale factor = 20)

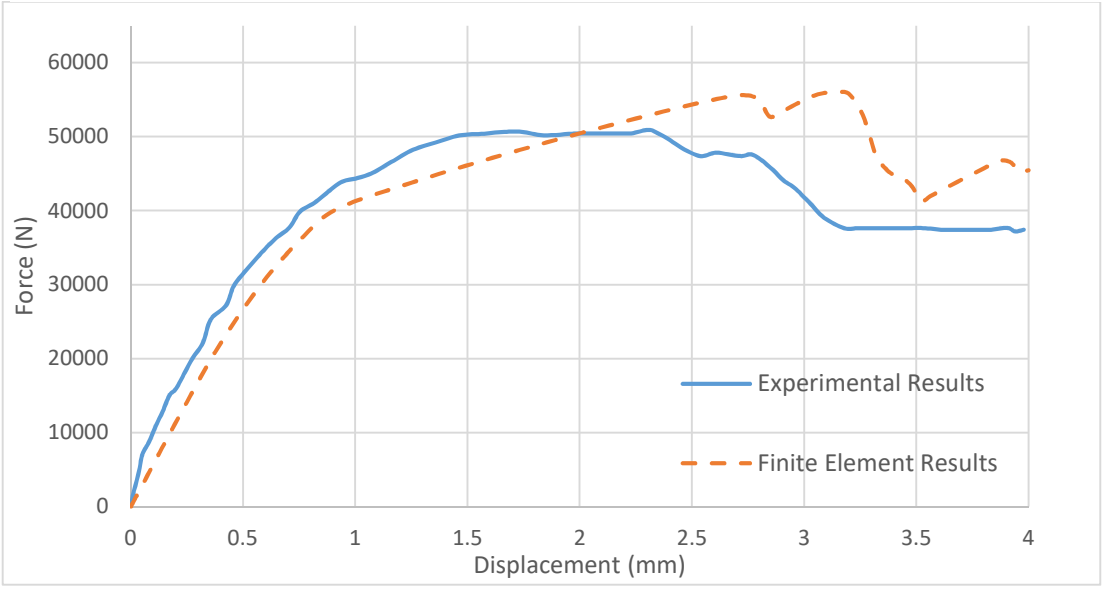

Figure 4.15: Comparison of force-displacement relationships

As shown in Figure 15, initial slopes of two graphs are close to each other. In addition to that, the peak value of finite element results is higher about %10 than the experimental results. This is assumed as an acceptable difference while comparing finite element results with the experimental results.

Following this initial stage, a parametric study was conducted to see the influence of the normal and tangential fracture energies by increasing and decreasing the reference values by 50%. In addition to that, the effect of the analysis method, and the effect of the viscosity parameter were investigated.

All the simulations were done by using quasi-static analyses in (Abdulla, et al. 2017). However, in this study, the dynamic/implicit method was used. In order to see the difference between quasi-static and dynamic/implicit analyses, the same model was used.

It has to be noted that, in all analyses linear traction-separation law is used for cohesive contact surfaces. By using exponential traction-separation law, the failure modes could not be captured.

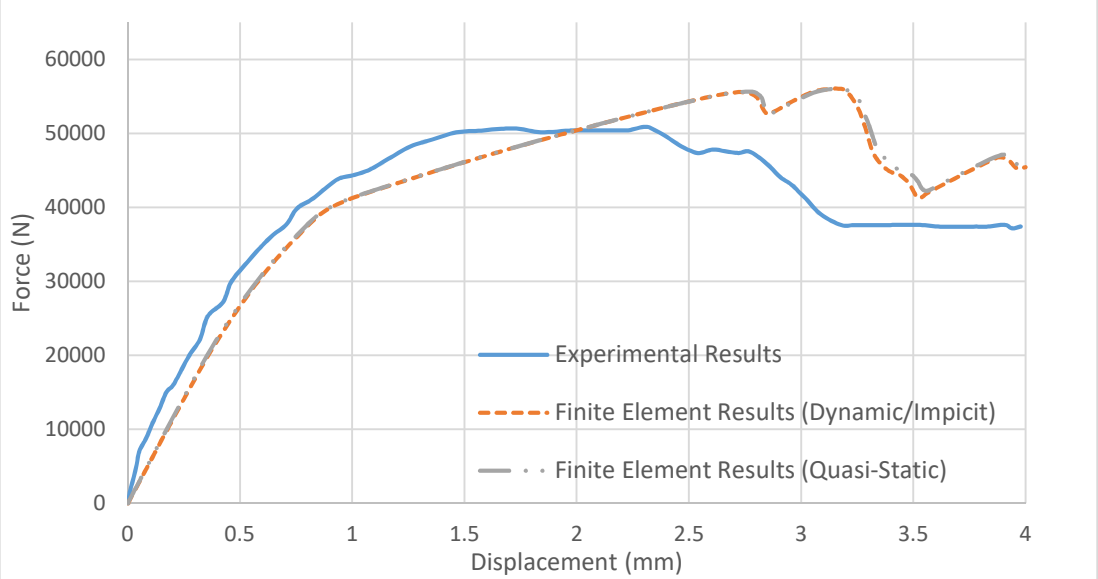

Figure 4.16: Comparison of quasi-static and dynamic/implicit analyses

According to the results presented in Figure 4.16, it can be seen that dynamic analysis which lasts 2 seconds gives close results to quasi-static analysis. In addition to that, the results showed that change in normal fracture energy is not influential for the in-plane behavior of the wall. Although the change in tangential fracture energy does not affect the initial slopes, it has a significant influence on strength (peak values) of the wall against in-plane loading. Increasing tangential fracture energy by 50% of, increased the

peak value about 5 kN. The relationship is the same if the tangential fracture energy decreased by %50. The comparisons can be seen in Figure 4.17 and 4.18.

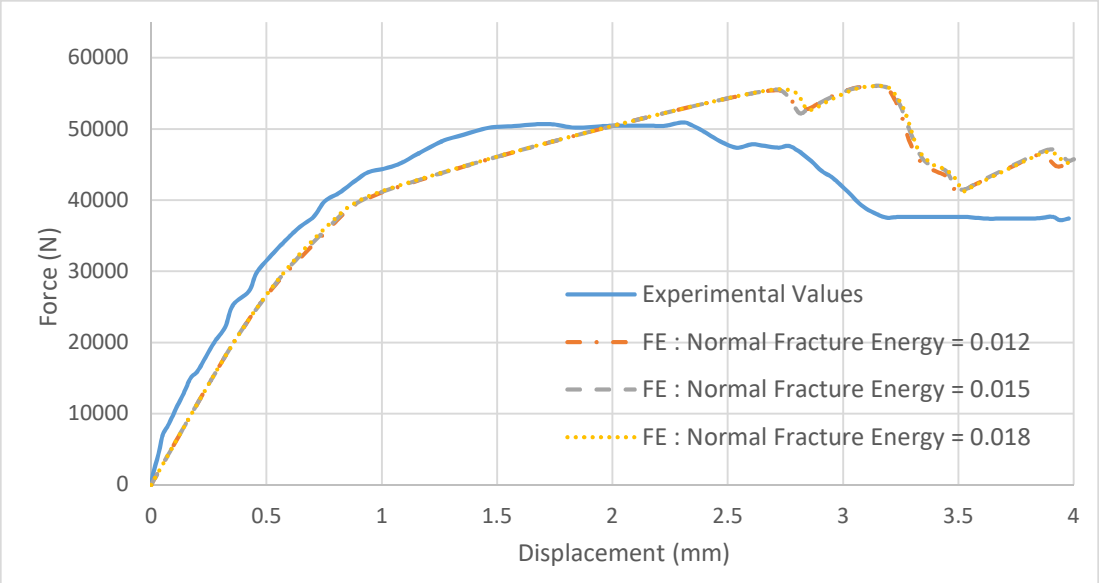

Figure 4.17: Comparison of analyses by using different normal fracture energies on cohesive surfaces.

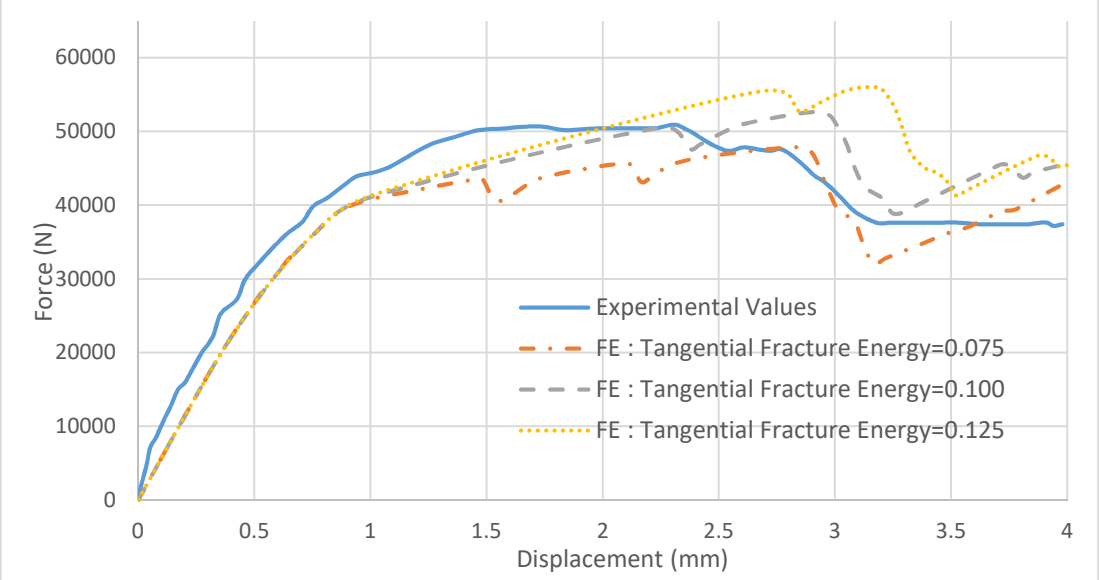

Figure 4.18: Comparison of analyses by using different tangential fracture energies on cohesive surfaces.

The influence of the viscosity parameter is investigated by creating three different models with viscosity parameter values of 0.0002, 0.002, and 0.02, respectively. It is observed that viscosity affects both the response of the wall and the computational cost.

The increase in viscosity reduces the computational cost but makes the results unreliable. In the model in which the viscosity was taken as 0.02, the failure mode of the wall could not be captured. The fluctuations observed in the later stages of loading become invisible when viscosity is taken as 0.02 as shown in Figure 4.19.

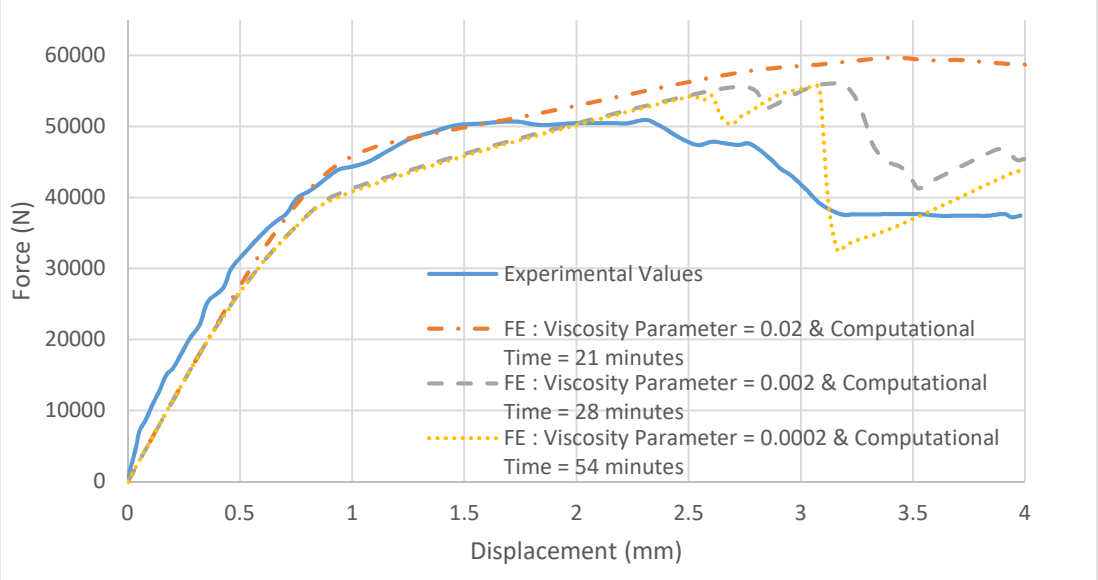

Figure 4.19: Comparison of analyses by using different viscosity parameters.

4.4. Meso-Scale Modelling of C-Shaped Wall: Out-of-Plane Behavior

Second validation analysis was conducted to see whether the meso-scale modeling approach is suitable to simulate the out-of-plane behavior of masonry walls. For this analysis, the experiment which was conducted by Griffith M., Vaculik J. (Griffith and Vaculik 2007) was chosen. This experiment was also mentioned in (Abdulla, et al. 2017).

In this experiment, an C-Shaped (plane view) wall was tested under out-of-plane loading. The wall consisted of one main portion and two flanges, see Figure 4.20. The main portion of the C-shaped wall had 4 meters of length and 2.5 meters of height and the flanges had 0.45 meters of length and 2.5 meters of height. The thickness of the wall was 110 mm in all cases. The wall was built by using 10-hole cored bricks which has 230 mm of length, 76 mm of height, and 110 millimeters of thickness. The bricks were bonded with mortar which has a thickness of 10 mm (Abdulla, et al. 2017).

In the experiment, the top and bottom portion of the C-shaped wall was simply supported along the entire length. The free edges of the wall were also restrained against

lateral movements by steel channel sections. The loading was done by applying pressure to the outer face of the main portion by means of an airbag. Detailed drawings and schematic representation of the experiment are shown in Figure 4.20, 4.21, and 4.22.

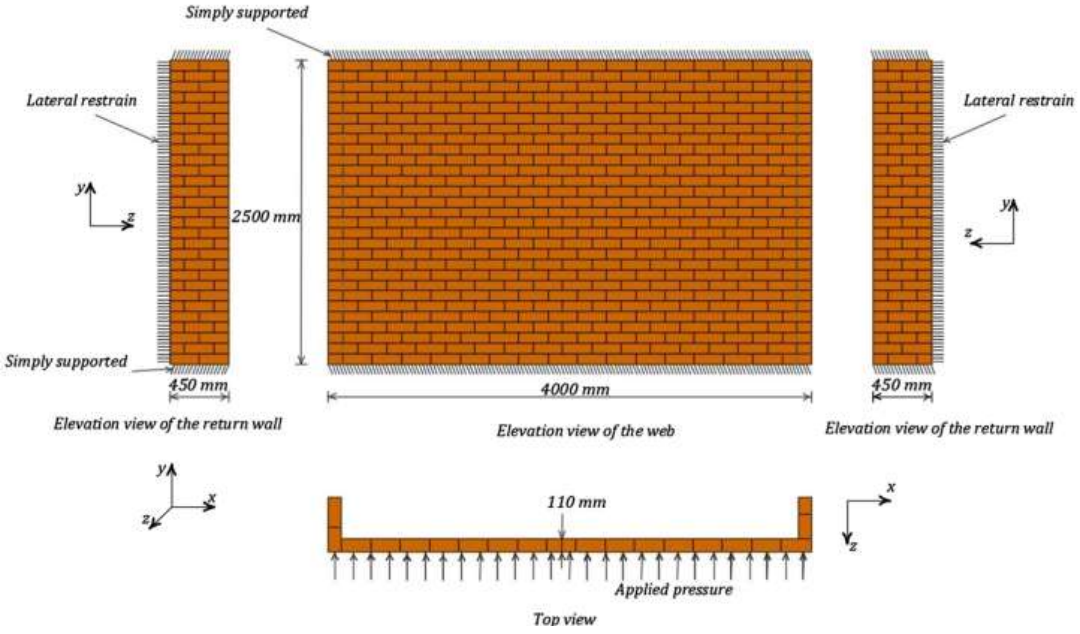

Figure 4.20: Geometry of the C-shaped wall. (Source: Abdulla, et al. 2017).

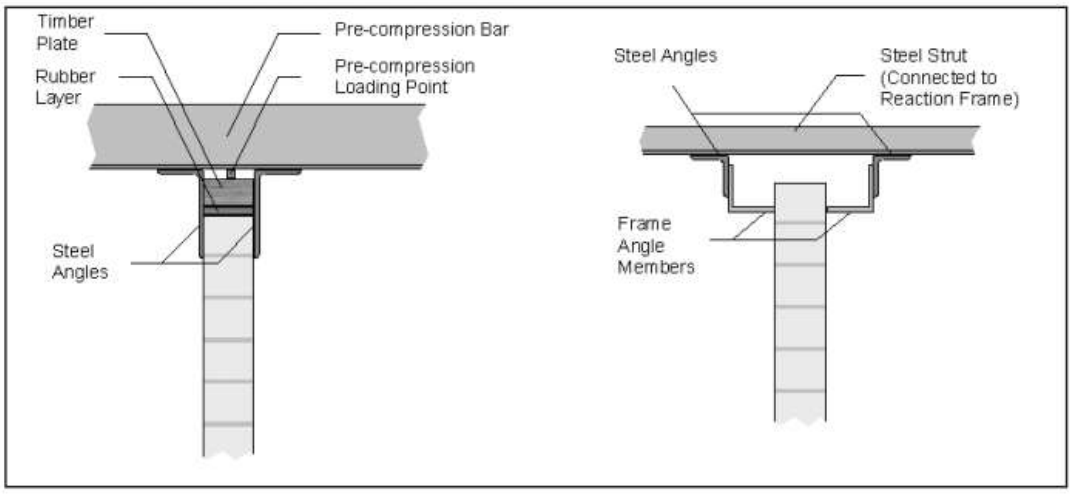

Figure 4.21: Detailed drawings of the experiment. (Source: Griffith and Vaculik 2007)

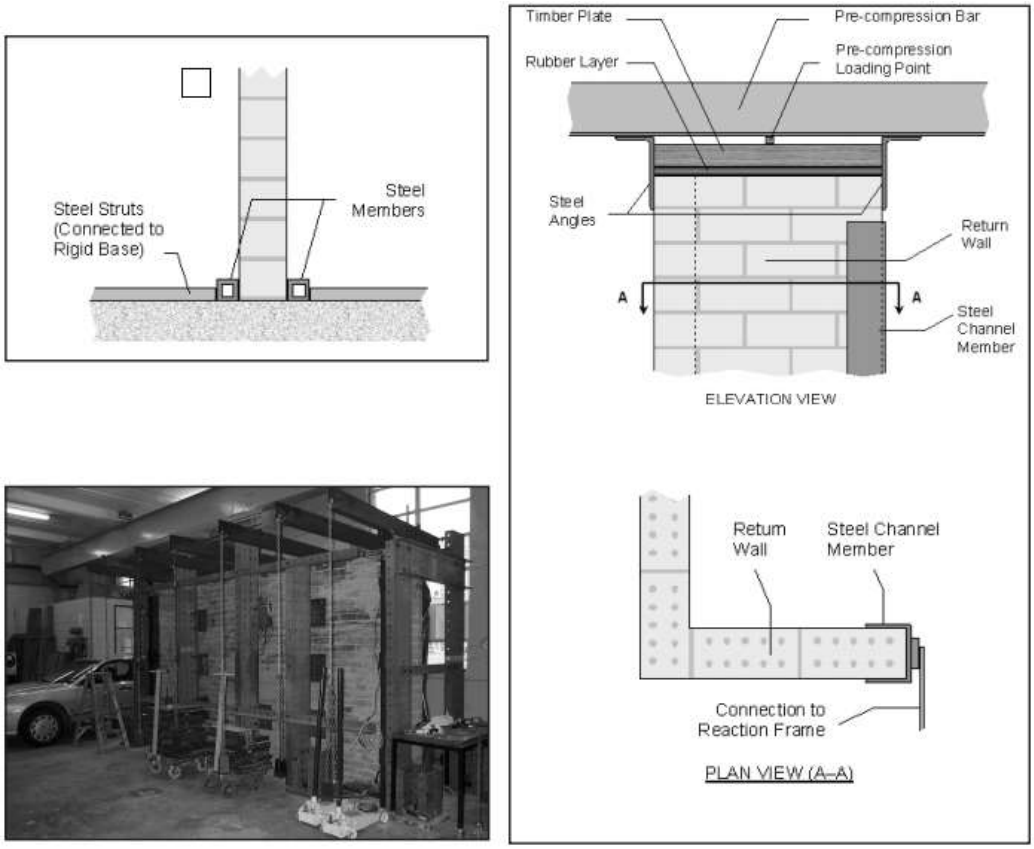

Figure 4.22: Detailed drawings of the experiment. (Source:Griffith and Vaculik 2007)

4.4.1. Finite Element Model

While preparing the base model, as in the first model, the geometry of the wall was created. After creating the general geometry and partitions, different named sections which have the same elastic and plastic properties assigned to each part. By using the same external program with the first validation model, surface-to-surface contacts were created. The discretized base model with different sections is shown in Figure 4.23.

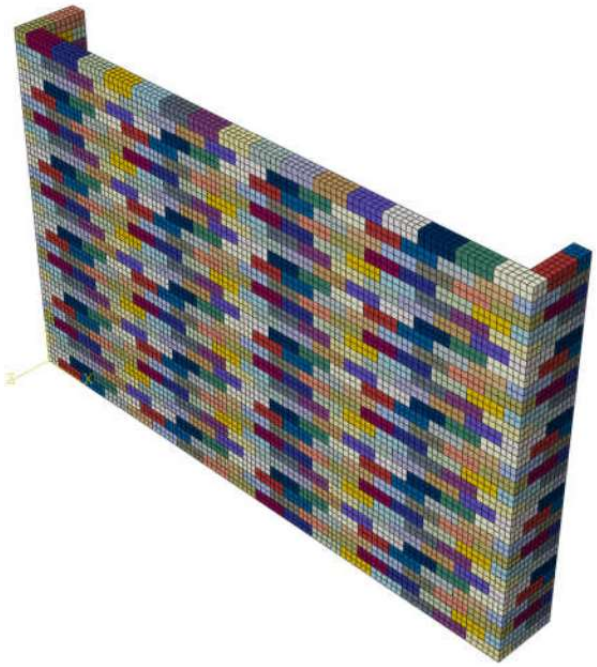

Figure 4.23: Numerical model of C-shaped wall with meshed bricks

After that, the parameters in (Abdulla, et al. 2017) were used to define the elastic and plastic properties of cohesive surfaces and units, see Table 4.2. As in the first model, the absolute plastic strains and corresponding yield stress are needed to define Drucker-Prager Plasticity/Cap model on expanded units. These values are obtained by using the same procedure with the first model, see Figure 4.24.

Table 4.2: The parameter table for units and cohesive surfaces. (Source: Abdulla, et al. 2017)

Joints	
K_{nn} (N/mm^3)	42
K_{ss} (N/mm^3)	17
K_{tt} (N/mm^3)	17
t_n^{max} (MPa)	0.12
G_{IC} (N/mm)	0.012
c (MPa)	0.17
μ	0.75
G_{IIC} (N/mm)	0.04

Units	
E_{brick} (MPa)	52700
ν	0.15
E_{mortar} (MPa)	420
E_{adj} (MPa)	3540
Flow Stress Ratio, R	1
Friction Angle, β	36
Dilatation Angle, ψ	13

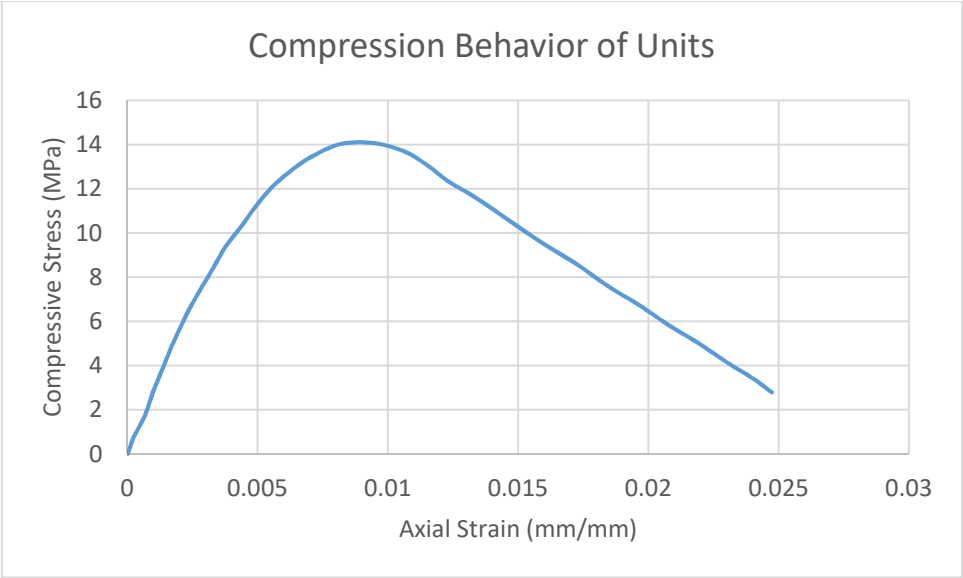

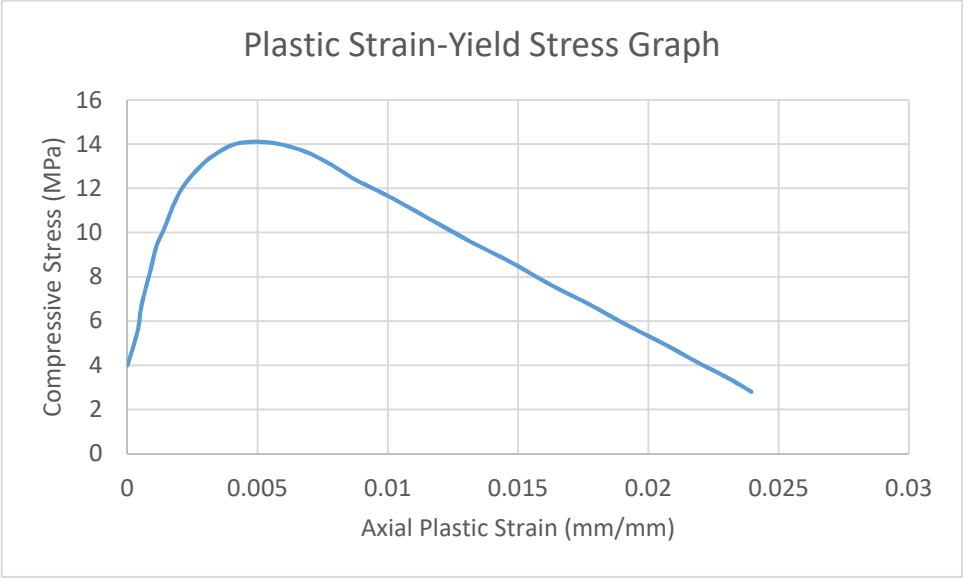

Figure 4.24: Compressive behavior of bulk units and plastic strain-yield stress graph for Drucker Prager/Cap model. (Abdulla, et al. 2017)

The nodes in the middle of the top and bottom face of the wall were simply supported motivated by the the detailed drawing of the experiment. It is thought that the bottom and the top surface of the C-Shaped wall are restrained against motion but not against small rotations. The free edges of the wall were restrained against out-of-plane direction from the middle points. After that, the pressure (3.04 kPa) was applied to the outer face of the C-shaped wall. As the loading protocol, a ramp function with a duration of 5 seconds was chosen. The loading protocol and the numerical model with constraints and loading can be seen in Figures 4.25.

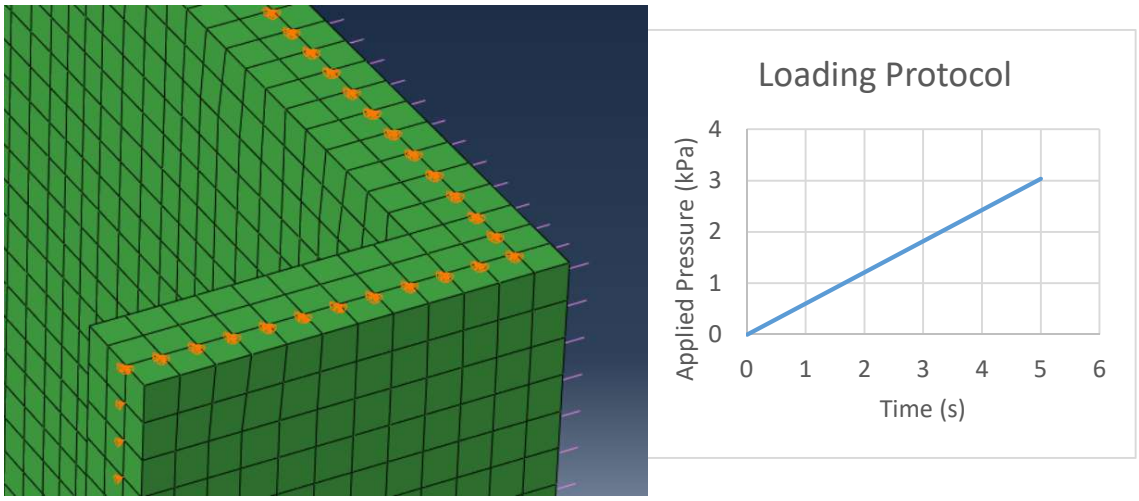

Figure 4.25: The nodes where the boundary conditions applied and loading protocol.

As in the first experiment, the viscosity parameter is selected as 0.002. The finite element model consists of 20358 linear hexahedral elements of type C3D8. Initial increment size, minimum increment size and maximum increment are selected as the same with the first validation model.

4.4.2. Results

The results showed that the failure pattern was similar to that in the experiment, see Figure 4.26. In the experimental and finite element results, the crack pattern started from the corners and joined at the center of the main portion. In addition to this good agreement, the comparison of pressure-displacement graphs is presented in Figure 4.27.

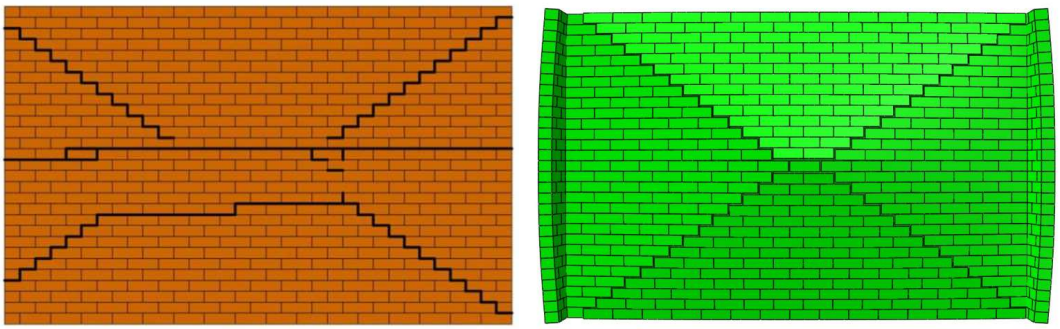

(a) (b)

Figure 4.26: Comparison of failure patterns: (a) experimental (Source: Abdulla, et al. 2017) ; (b) numerical (scale factor = 10)

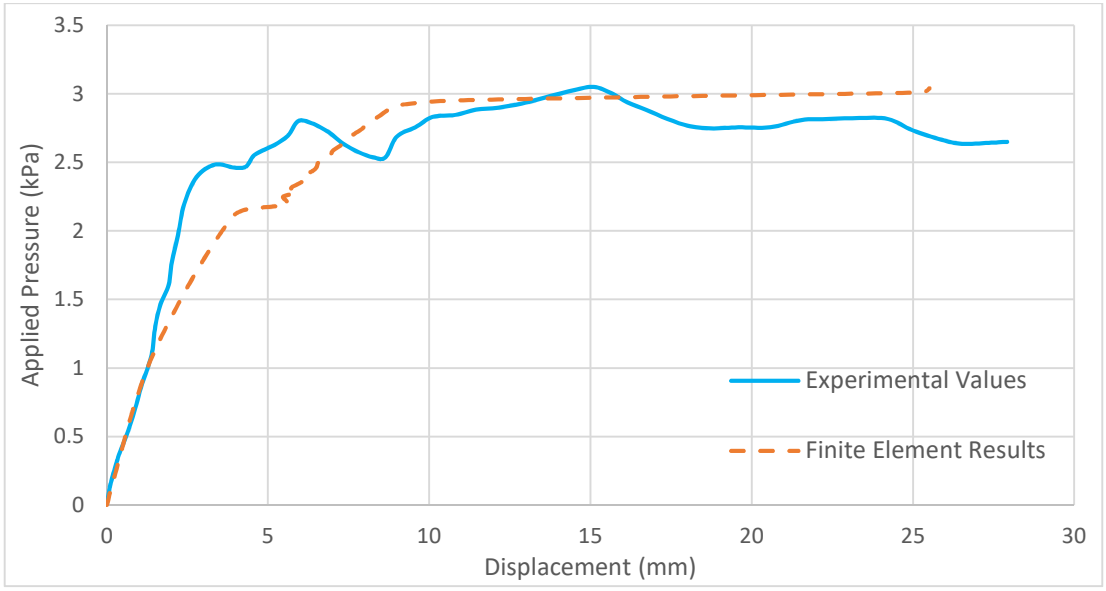

Figure 4.27: Comparison of relationships between the out-of-plane displacement of the center point and applied pressure in numerical an experimental results

Following this initial stage, a parametric study was conducted to see the influence of the normal and tangential fracture energy on the out-of-plane behavior of the masonry wall. As in the first validation, the effect of the viscosity parameter was also investigated.

The results showed that an increase and decrease in normal and tangential fracture energy by 50% did not change the response significantly. The difference of the responses with different fracture energies can be seen in Figure 4.28 and 4.29.

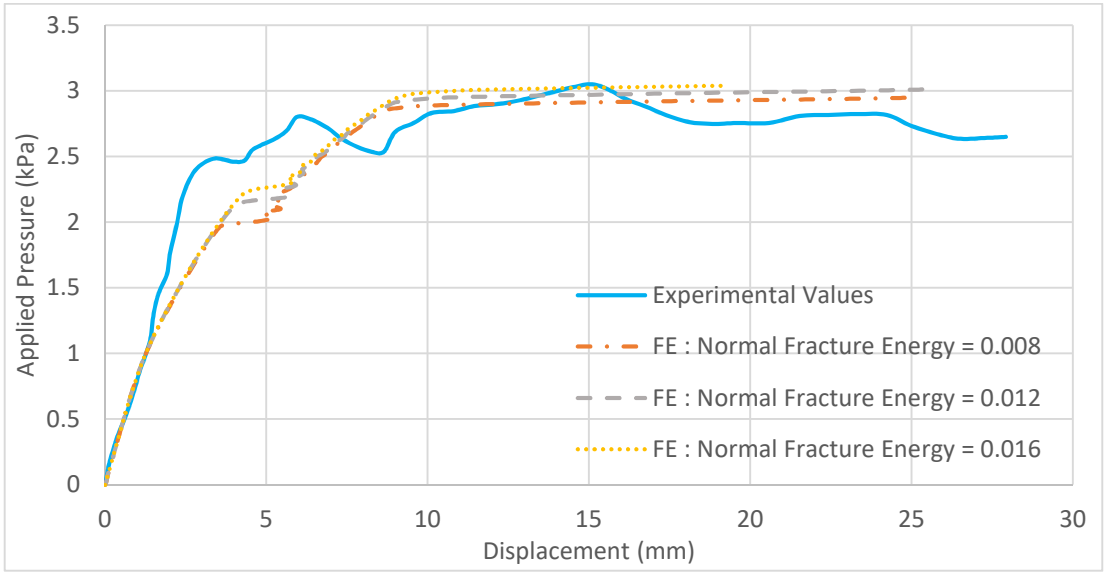

Figure 4.28: Comparison of analyses by using different normal fracture energies on cohesive surfaces.

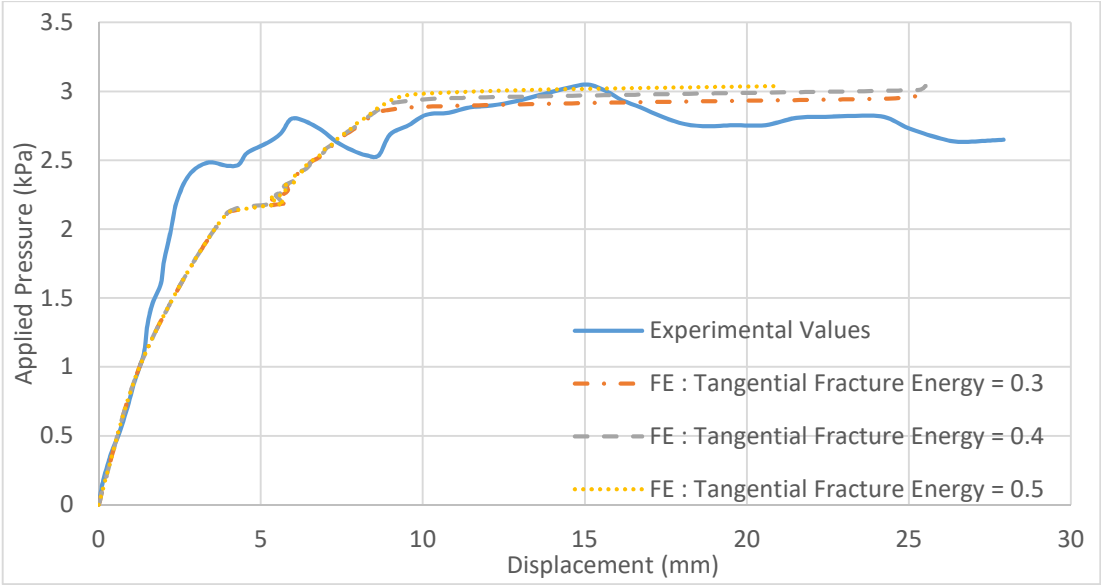

Figure 4.29: Comparison of analyses by using different tangential fracture energies on cohesive surfaces.

As in the first numerical validation, using a higher viscosity parameter, reduced the computational time. However, when the viscosity parameter is taken as 0.02, the failure pattern could not be captured. Figure 4.30 shows the response of different numerical models with different viscosity parameters.

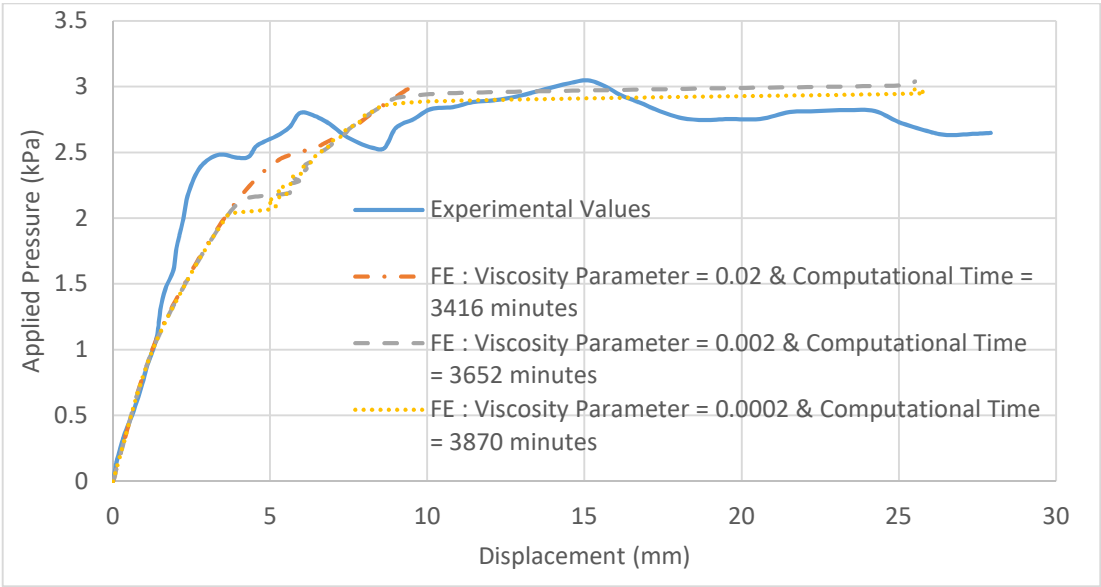

Figure 4.30: Comparison of analyses by using different viscosity parameters.

4.5. Choice of Viscosity Parameter

The damping introduced by viscous dissipation is controlled by viscosity parameter. This numerical effect should be tuned carefully since this might have an effect on the physical response of the structure, see Figure 4.19 and 4.30. Unfortunately, the proper value of viscosity parameter is problem dependent and to the author's knowledge, general guidelines for the selection of viscosity parameter do not exist. However, a set of analysis can be conducted to select the suitable viscosity parameter. After obtaining a sufficiently large viscosity parameter (with which the analysis is completed), the analysis can be repeated by a smaller viscosity value, for example by halving the viscosity parameter. If the analysis could be completed by this new value, the same procedure can be repeated until the critical viscosity parameter with which the analysis could not be completed, is identified.

CHAPTER 5

ANALYSES OF AN ANCIENT LIGHTHOUSE USING MESO-SCALE MODELING

The main purpose of this work is to investigate the seismic behavior of an ancient lighthouse using a meso-scale finite element model. In this chapter, general information about the lighthouse, the components of the finite element model and the associated parameters, the earthquakes used as the base excitations are presented, and the results of the analysis are discussed.

5.1 General Information About the Lighthouse

The lighthouse is located in the Ancient City of Patara in the province of Antalya and named as Patara Lighthouse. It is the oldest known lighthouse and thought that the lighthouse was built by Emperor Nero in 64-65 AD. This lighthouse is an important legacy that should be passed on to future generations in terms of its cultural, architectural and aesthetic values (Özkut 2009).

The current state of the lighthouse can be seen in Figure 5.1. In its original form, the lighthouse consists of a body part of approximately 20 meters and a cap part of 5 meters in height. The illustration of the original form of the lighthouse and the side view are shown in Figure 5.2.

Figure 5.1: The current situation of the lighthouse

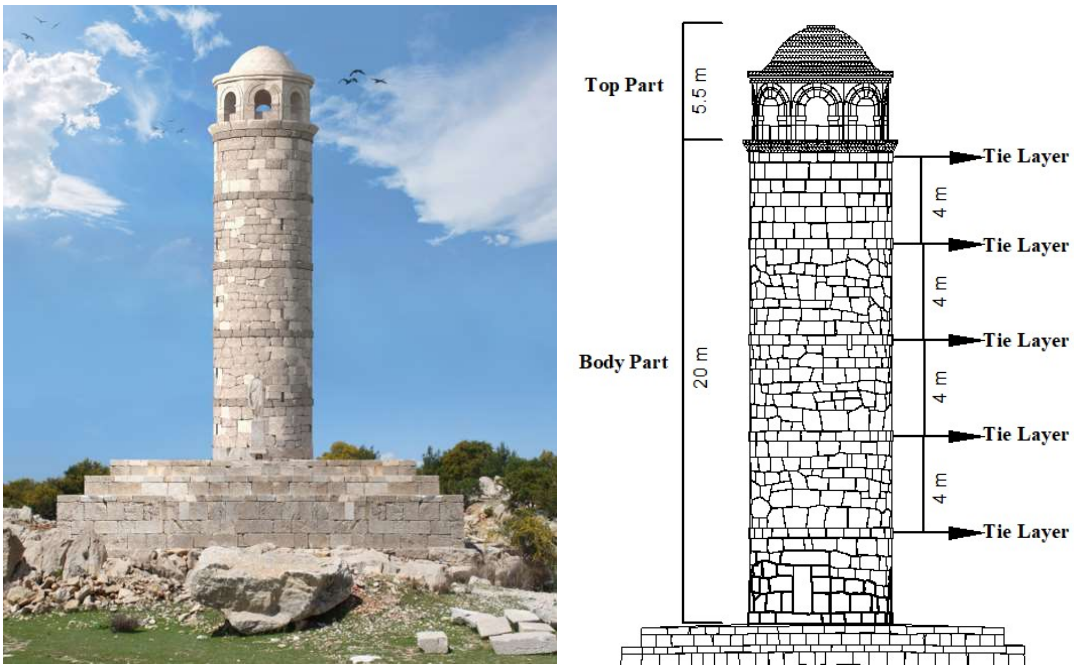

(a) (b)

Figure 5.2: The estimated view of original lighthouse (a); the side view drawing with approximate dimensions (Source: Deniz Alkan Mühendislik 2020) (b)

As shown in Figure 5.3, the cross-section consists of an outer shell, an inner shell, stairs and the core.

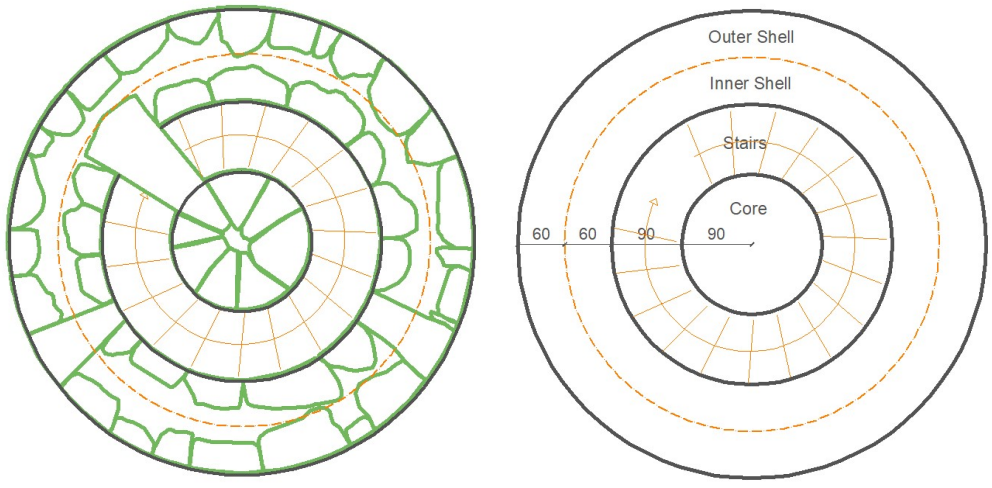

(a) (b)

Figure 5.3: The original regular section of lighthouse (Source: Deniz Alkan Mühendislik 2020) (a); parts of section (b) (dimensions are in cm)

The basis parameters for the elastic design spectrums (for ZA type of soil and DD2 as earthquake ground motion level) according to the TEC 2018 are obtained as S_s=0.991, S_1=0.264, S_{DS}=0.793, S_{D1}=0.211, PGA=0.431 g, PGV=21.389 cm/sec from https://tdth.afad.gov.tr using the coordinates of Ancient City of Patara. It is noted that these parameters are not used in the following analysis.

5.2 Finite Element Model

While modeling the lighthouse, creating the whole geometry in one step was not a simple task. The main reasons for that are the shape of the cap part and the spiral stairs in the lighthouse. Therefore, it is assumed that there are 35 regular layers and 5 tie layers (appears after 8 regular layers) within the body part of the lighthouse. The regular layers and tie layers are divided into 46 parts and 28 parts, respectively. After the discretization process, differently named sections are assigned to each part. Examples of the regular layers and the tie layers are shown in Figure 5.4.

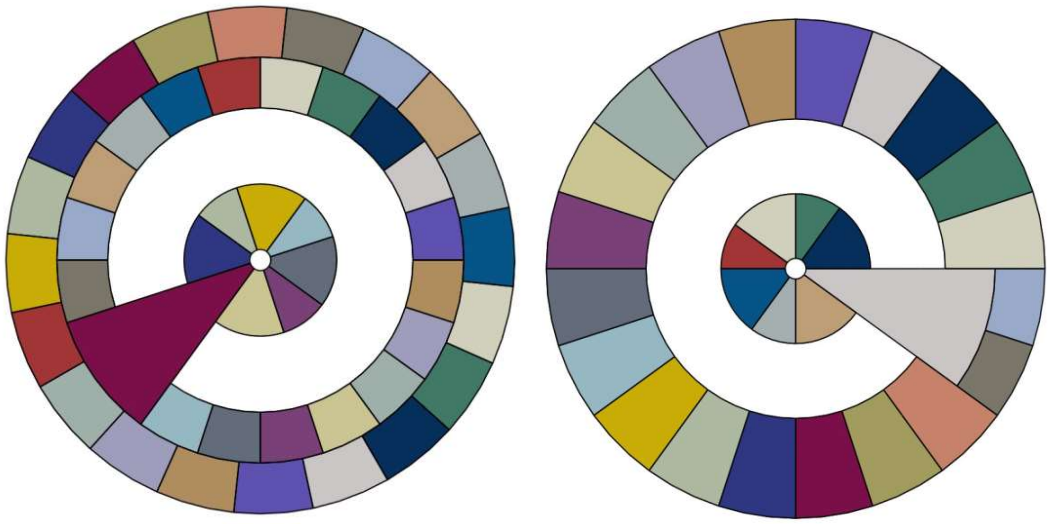

(a) (b)

Figure 5.4: Plan view of layers with different sections: (a) regular layer; (b) tie layer

To construct the main body of the lighthouse, single layer is used as the building block. Each layer is rotated by 18 degrees and put on top of the previous one as shown in Figure 5.5. By following this procedure, it has become possible to build the outer shell, inner shell, stairs and the core. In Figure 5.6, the rotations of layers are shown by removing the outer shell from view.

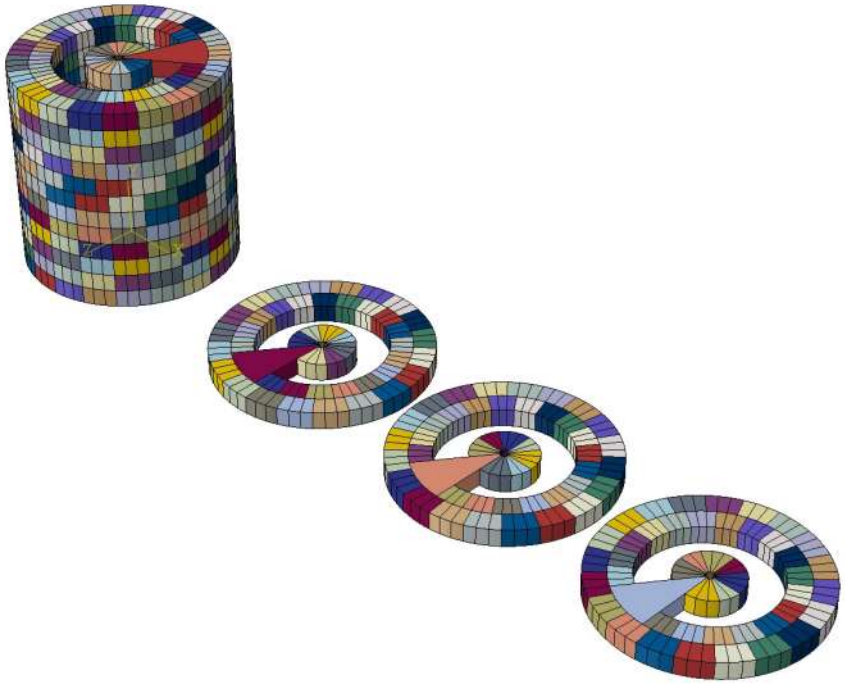

Figure 5.5: Modelling process of the body part

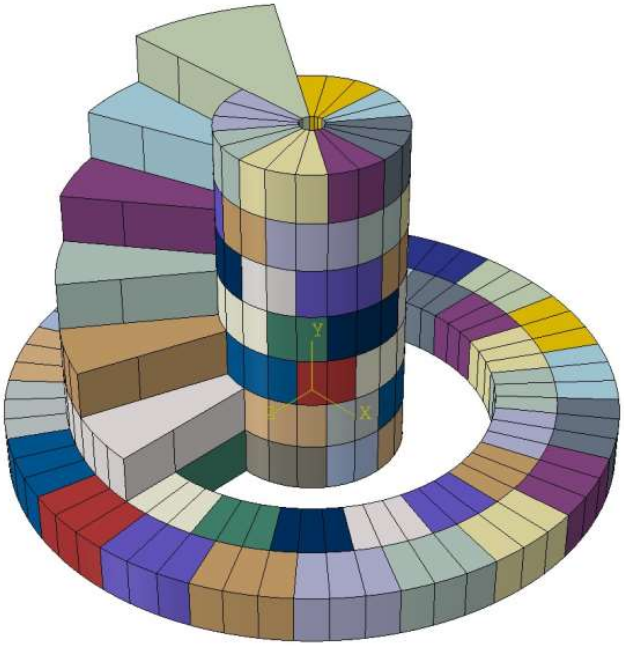

Figure 5.6: The rotations of layers.

After putting the whole layers on top of each other, they are merged in the assembly section of ABAQUS. Then, by using the external program which was used in

validation models, the cohesive contact surfaces between the units (parts) are created. Because of the complex shape of the cap part, it is treated as a monolithic continuous part as shown in Figure 5.7.

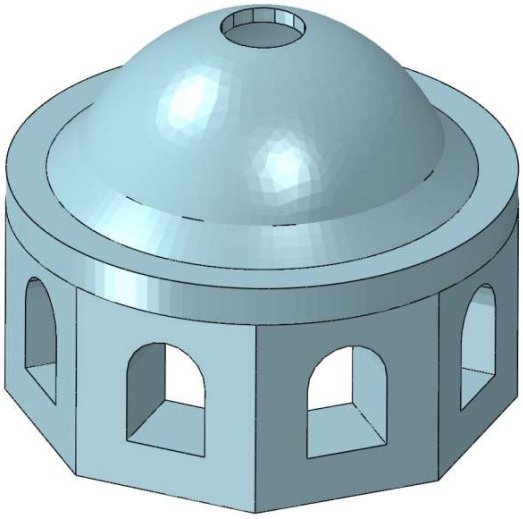

Figure 5.7: The numerical model of the cap part

In the preliminary studies of this thesis, the geometry of the body part is created without openings. After getting unrealistic results with the model without openings, it is decided to create the door and windows with reference to the original geometry of the lighthouse. After creating the “door” and “windows” in the body part, as shown in Figure 5.8, in the last step, the body of the lighthouse and the cap part are attached by using “tie constraint”. The final form of the model is shown in Figure 5.9.

.

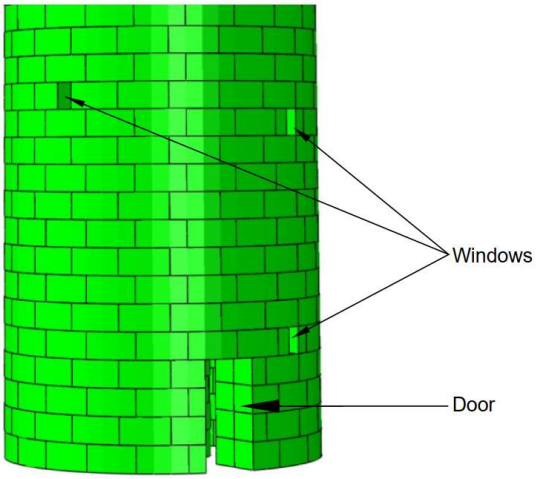

Figure 5.8: The “openings” in the numerical model.

Figure 5.9: The final form of the geometry of the numerical model.

5.2.1 The Material Parameters

In all analyses, linear traction-separation law is used to define the mechanical behavior of the joints and Drucker-Prager/Cap plasticity model is used to define the mechanical response of the bulk units. The known and calculated parameters using equations mentioned in Chapter 4 are given in Table 5.1.

Table 5.1: The known and calculated parameters

Units	
E_u (Mpa)	20490
ν	0.25
E_m (Mpa)	19230
E_{adj} (Mpa)	19672.5
Density (kg/m^3)	2636
Flow Stress Ratio, R	1
Friction Angle, β	36
Dilatation Angle, ψ	13

Joints	
K_{nn} (N/mm^3)	15635
K_{ss} (N/mm^3)	70003.6
K_{tt} (N/mm^3)	70003.6
μ	0.75

As in the validation models, the absolute plastic strains and corresponding yield stress values are needed to define Drucker-Prager/Cap plasticity model. However, the compression behavior of the units is not known. The only available data for the mechanical characteristics of the stones and mortar are obtained from an internal report. These are the elasticity modules of stones and mortar (20490 MPa and 19230 MPa, respectively) and the compressive strengths (80.1 MPa and 21 MPa, respectively). Therefore, modified Kent and Park model is used to describe the stress-strain behavior of stones, inspired by (Kaushik, et al. 2007) where the behavior of bricks was modeled by modified Kent and Park model. At first, the plastic strains are calculated with the model given in (Kaushik, et al. 2007) directly by extracting the elastic strains. However, the results show negative plastic strain values which are not physically possible. Therefore, some parameters given in (Kaushik, et al. 2007) are changed considering the compressive strength and modulus of elasticity of units. The model in (Kaushik, et al. 2007) are defined by the following equations

$$f_m = 1.067 f_m' \left[\frac{2\varepsilon_m}{0.002} - \left(\frac{2\varepsilon_m}{0.002} \right)^2 \right] \quad \text{for } 0 \leq \varepsilon_m \leq 0.0015 \text{ (rising curve)} \tag{5.1}$$

$$f_m = f_m'[1 - Z_m(\varepsilon_m - 0.0015)] \quad \text{until } 0.2 f_m' \text{ (descending curve)} \tag{5.2}$$

and

$$Z_m = \frac{0.5}{\left[\frac{3 + 0.29 f_j}{145 f_j - 1000} \right] - 0.002} \tag{5.3}$$

where f_m and ε_m represents the compressive stress and strain in masonry, respectively. f_m' is the compressive strength of masonry and f_j' is the compressive strength of mortar.

Since there is no information about compressive strength of masonry prism which consists of stones and mortar, the compressive strength (f_m') is assumed as equal to the compressive strength of the stone. The “updated” model are defined by the following equations.

$$f_m = 1f'_m\left[\frac{2\varepsilon_m}{0.0077} - \left(\frac{2\varepsilon_m}{0.077}\right)^2\right] \quad \text{for } 0 \le \varepsilon_m \le 0.0077 \text{ (rising curve)} \tag{5.4}$$

$$f_m = f'_m[1 - Z_m(\varepsilon_m - 0.0077)] \quad \text{until } 0.2f'_m \text{ (descending curve)} \tag{5.5}$$

where

$$Z_m = \frac{0.5}{\left[\frac{3 + 0.29f_j}{145f_j - 1000}\right] - 0.004} \tag{5.6}$$

By using the equations (5.4), (5.5) and (5.6) the compressive behavior of the units are obtained. Then, by extracting the elastic strains from the total strains, absolute plastic strain values and corresponding yield stress values are obtained, see Figure 5.10 and 5.11.

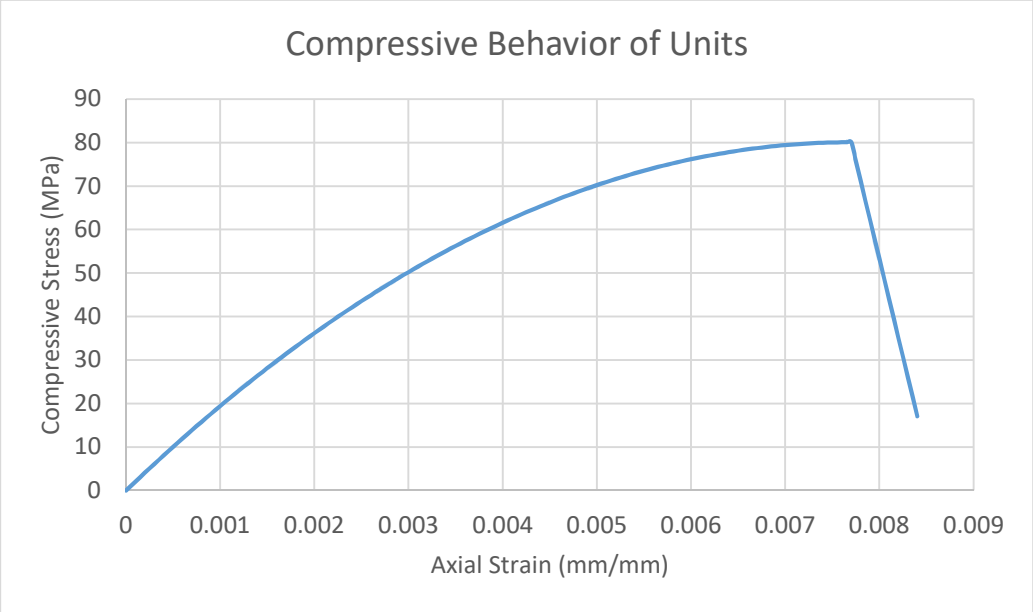

Figure 5.10: Compressive behavior of units

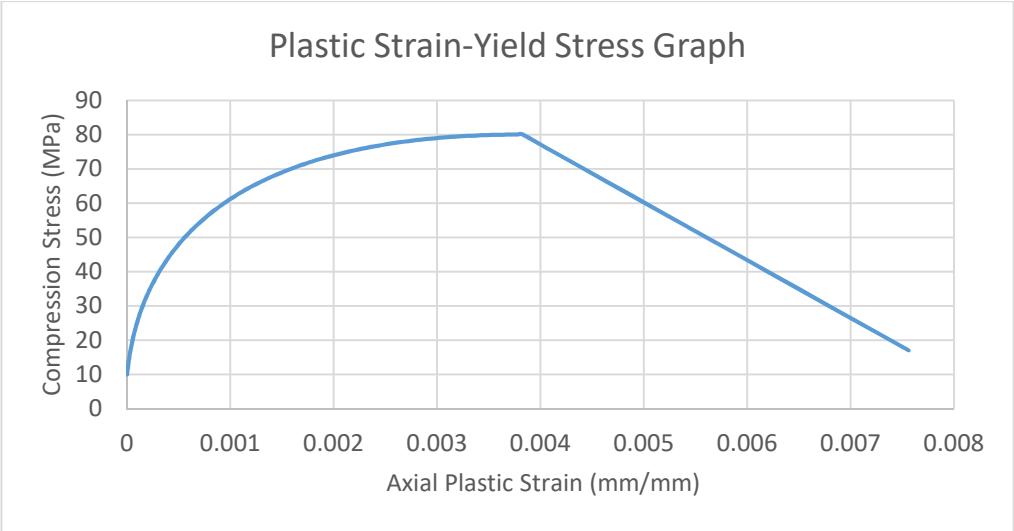

Figure 5.11: Plastic strain-yield stress graph for Drucker Prager/Cap model

Since there is no information about the tensile strength of the mortar, except the cohesion values, 3 different models are created by using the parameters given in Table 3.2. The cohesion values are taken as 1.4 of tensile strengths (Lourenco 1996). One of them (L1) has the upper limit parameters, the second model (L2) has the lower limit parameters. In the last one, half of the lower limit parameters are used to investigate the influence of the tensile strength and the fracture energies of the mortar on the seismic behavior of the lighthouse in more detail. These parameters are shown in Table 5.2.

Table 5.2: The strength and fracture energy values of cohesive contact surfaces for 3 different models

Parameters	**Model L1**	**Model L2**	**Model L3**
Tensile Strength (MPa)	0.9	0.3	0.15
Cohesion (MPa)	1.26	0.42	0.21
Normal Fracture Energy (Nmm/mm^2)	0.02	0.005	0.0025
Tangential Fracture Energy (Nmm/mm^2)	0.25	0.01	0.005

In real structure, there is big stone above the door as shown in Figure 5.1. Therefore, the strength and fracture energy values of the cohesive surfaces shown in Figure 5.12, magnified by 10 to be sure about that the cohesive surfaces do not separate.

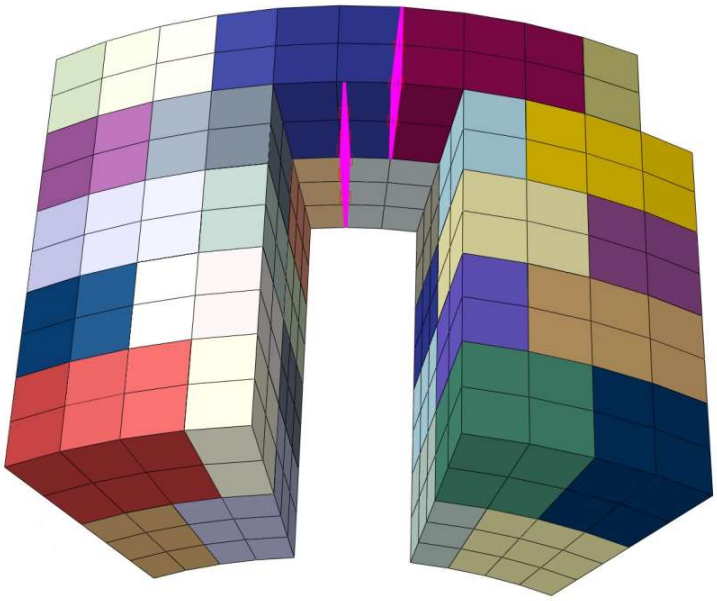

Figure 5.12: The cohesive surfaces with magnified (10 times) properties

Unlike the previous validation studies, the effect of the normal compressive stress on the tangential strength of the horizontal joints (see Figure 2.7) is considered more precisely. The tangential strengths of every level are increased with the compressive stress on the layer by multiplying it with the friction coefficient according to the equation (4.15). Friction coefficient, μ, is taken as 0.75 similar to the previous validation models. The normal compressive stresses are calculated by considering the total weight of the layers above that layer and the weight of the cap part. These values are given in Table 5.3. However, in vertical joints (see Figure 2.7), the tangential strength is defined as the cohesion value. The variation of tangential strength along the layer for 3 different models are shown in Figure 5.13, 5.14 and 5.15, respectively.

Table 5.3: Properties of Lighthouse

Area of 1 Layer (m^2)	21.4
Height of 1 Layer(m)	0.5
Density (kg/m^3)	2636
Weight of 1 Layer (tons)	28.2
Weight of Cap Part (tons)	118.85

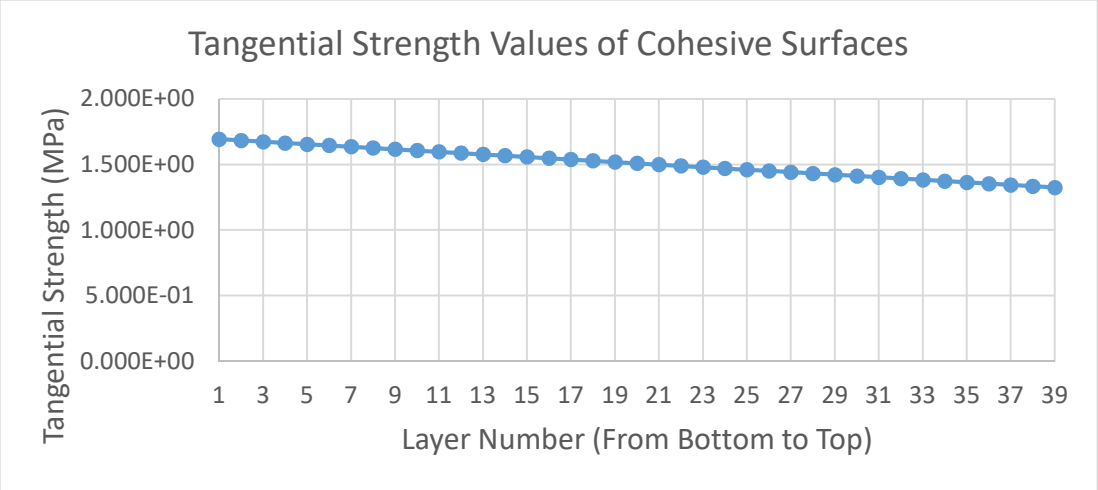

Figure 5.13: Tangential Strength Values of Cohesive Surfaces in L1

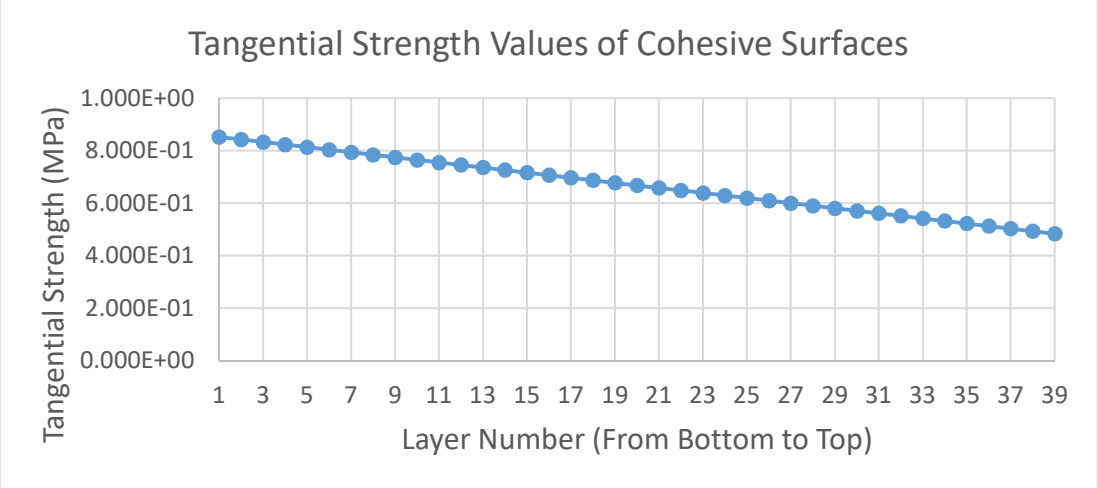

Figure 5.14: Tangential Strength Values of Cohesive Surfaces in L2

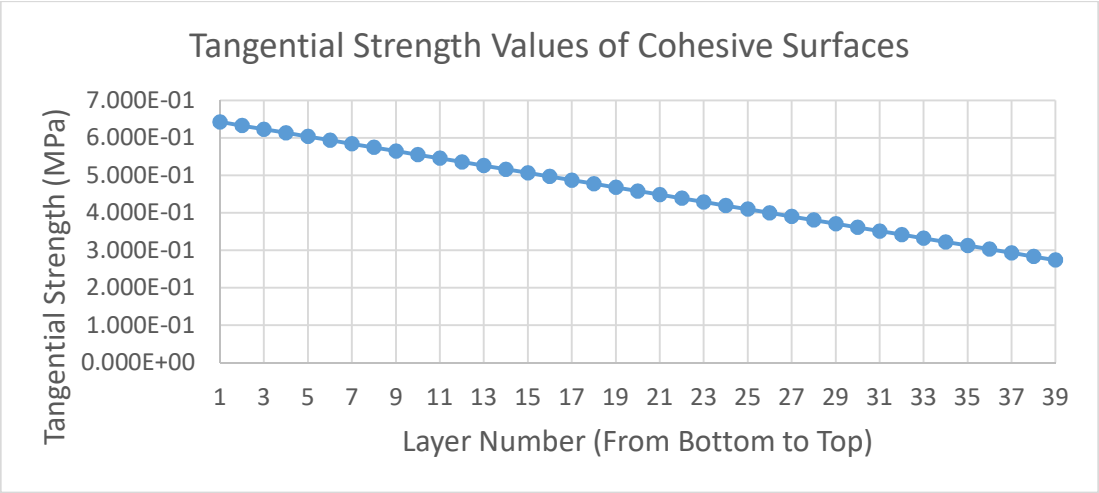

Figure 5.15: Tangential Strength Values of Cohesive Surfaces in L3

5.2.2 Basic Dynamic Characteristics of the Lighthouse

The total mass of the lighthouse is 1247 tons. In order to get an insight about basic dynamic characteristics of the structure, a monolithic linear elastic model is built and the mode shapes are determined. This model ignores interfaces between units and a unique modulus of elasticity, E=19672.5 MPa, is used. In Figure 5.16, the first four mode shapes are shown. The partial symmetry of the lighthouse caused that the first two mode shapes are very similar to each other.

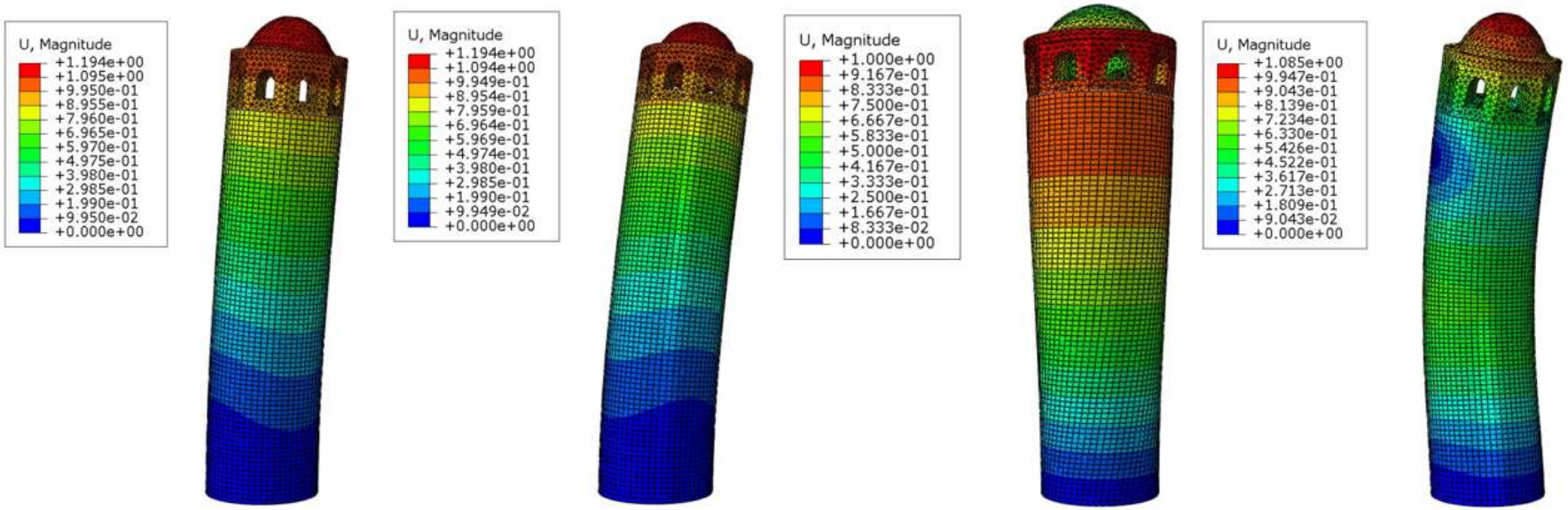

Figure 5.16: From left to right ; mode shape 1 (frequency:4.6778 cycles/second), mode shape 2 (frequency: 4.6829 cycles/second), mode shape 3 (frequency: 19.282 cycles/second), mode shape 4 (frequency: 21.594 cycles/second

5.2.3 Earthquake Records Used in Analyses

In order to investigate the behavior of the lighthouse under seismic excitations, realistic seismic events have to be selected and used in finite element analyses. In this study, Erzincan Earthquake (1992) and Kocaeli Earthquake (1999) are chosen to be applied to the lighthouse model. The earthquake records are taken from PEER NGA-West2 Strong Motion Database (Ancheta, et al. 2013).

After site investigation, it is observed that the lighthouse was built on rock. Therefore, the type of the soil under the lighthouse was assumed to be ZA according to the Turkish Earthquake Code 2019. All the earthquakes are scaled according to the spectrum of ZA in TEC 2019 by using SeismoMatch Software (https://seismosoft.com). This software offers two "matching algorithms" and the one proposed by Al Atik and Abrahamson (Al Atik and Abrahamson 2010) is selected. This algorithm is using an improved tapered cosine function as the adjustment function and prevents drift in velocity and displacements, see (Al Atik and Abrahamson 2010) for details. The comparison of raw and scaled (matched with ZA) data (acceleration values and Spectrums) for earthquakes are given in Appendix A.

5.3 Results

In this section, the models with different cohesive contact properties (L1, L2 and L3) is discussed by means of energy dissipations during 2 different earthquake records. The mentioned energy dissipations in the models are:

- Dissipated energy by damage in cohesive contact surfaces,
- Dissipated energy by plasticity in bulk units,
- Dissipated energy by the friction between cohesive contact surfaces after a local failure,

Due to the computational cost and convergence problems, all analyses is aborted at the last time the analyses have reached or at the time when the separation at joints can be seen clearly.

5.3.1 Results of The Analyses by Using the Model "L1"

In the analyzes made with the Erzincan earthquake, the first mechanism to occur is the damage mechanism on cohesive contact surfaces with a steep slope. Immediately after, friction and plasticity mechanisms start, see Figure 5.16. After 6.6th second, a rapid increase in dissipated energy by friction between units is seen. This increase means that relative sliding of a significant mass portion occurred between 6.6th second and 6.9th second, see Figure 5.17. At the end of 9th second, the plastic strains accumulate at the bottom part of the outer shell. The separations are seen at the bottom portion of the lighthouse, see Figure 5.18.

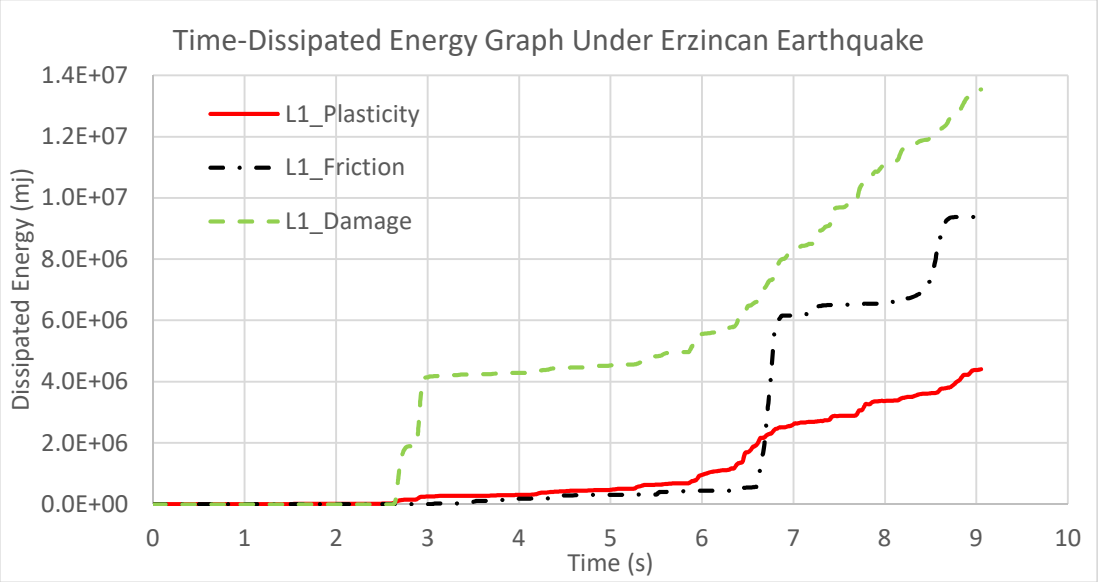

Figure 5.17: Dissipated Energy Values Caused by Different Mechanisms during Erzincan Earthquake History.

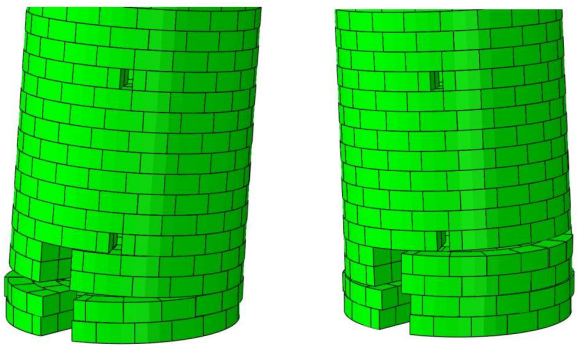

(a) (b)

Figure 5.18: Deformed Shape (scale factor = 15) of "L1" at 6.6th second (a) and 6.9th second (b) of Erzincan Earthquake History.

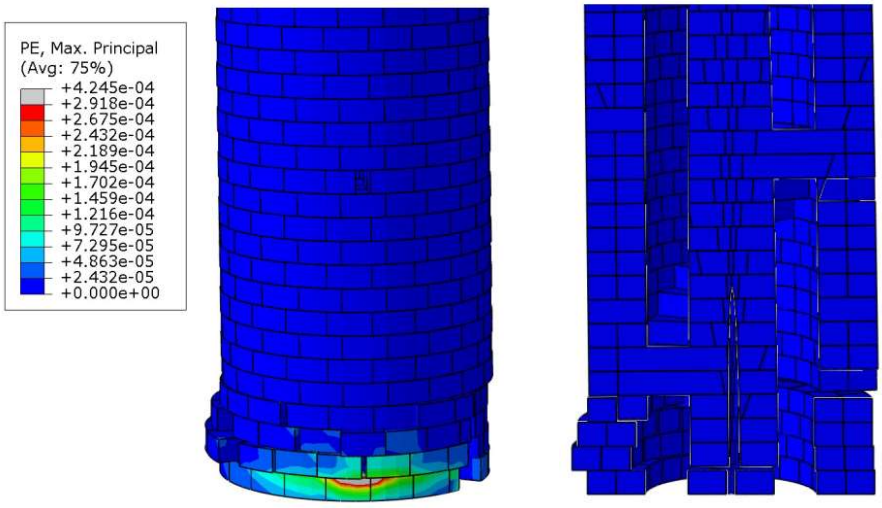

Figure 5.19: Plastic Strain Values and Deformed Shape (scale factor = 15) of "L1" at 9th second of Erzincan Earthquake History.

During Kocaeli Earthquake History, the first seen mechanism is damage in cohesive contact surfaces, as in previous analysis. It stars at the 9.9th second with a steep slope. Immediately after that, the increase in dissipated energy by the other mechanisms can be seen. Although the dissipated energy due to the friction changes instantaneously at 12.8th second and 14.25th second, the other dissipation mechanisms have more stable patterns, see Figure 5.19. This instantaneous change is a result of sliding of the almost whole structure, see Figure 5.20. The amounts of dissipated energy by friction and damage are closer to each other compared with the previous model (with Erzincan Earthquakes). It means that, the response of the lighthouse under Kocaeli Earthquake has earlier local problems (separations and slidings on joints).

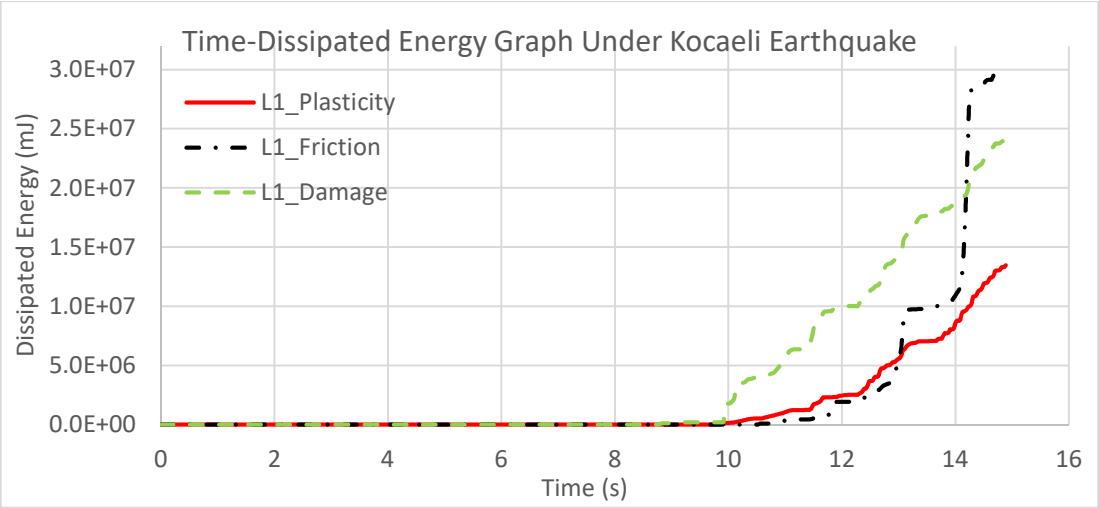

Figure 5.20: Dissipated Energy Values Caused by Different Mechanisms during Kocaeli Earthquake History.

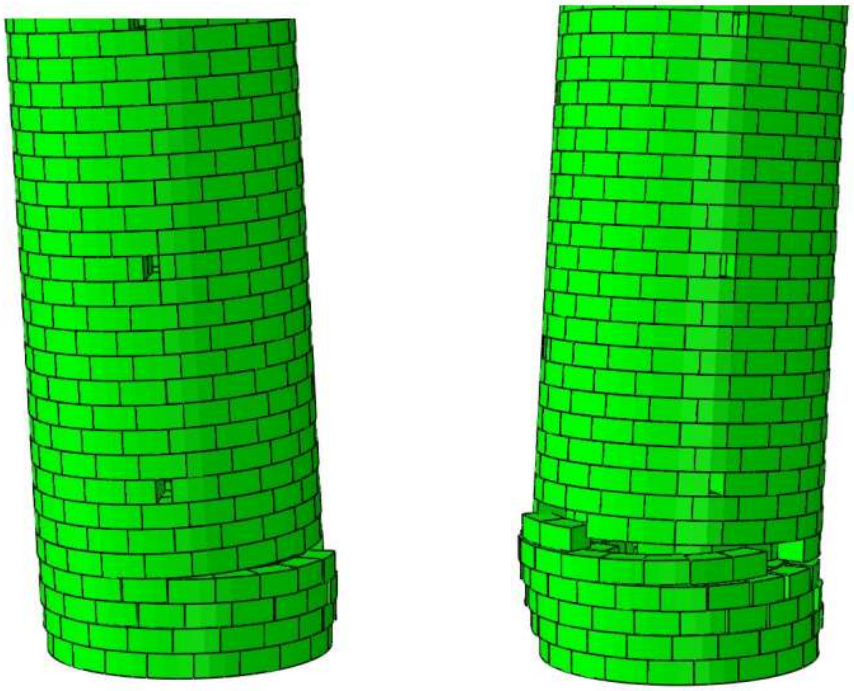

(a) (b)

Figure 5.21: Deformed Shape (scale factor = 10) of "L1" at 12.8th second (a) and 14.85th second (b) of Kocaeli Earthquake History

It can be said that, the failure (separation of joints and sliding) and plastic strains are occurred at the bottom portion of the structure during Kocaeli Earthquake history, see Figure 5.21.

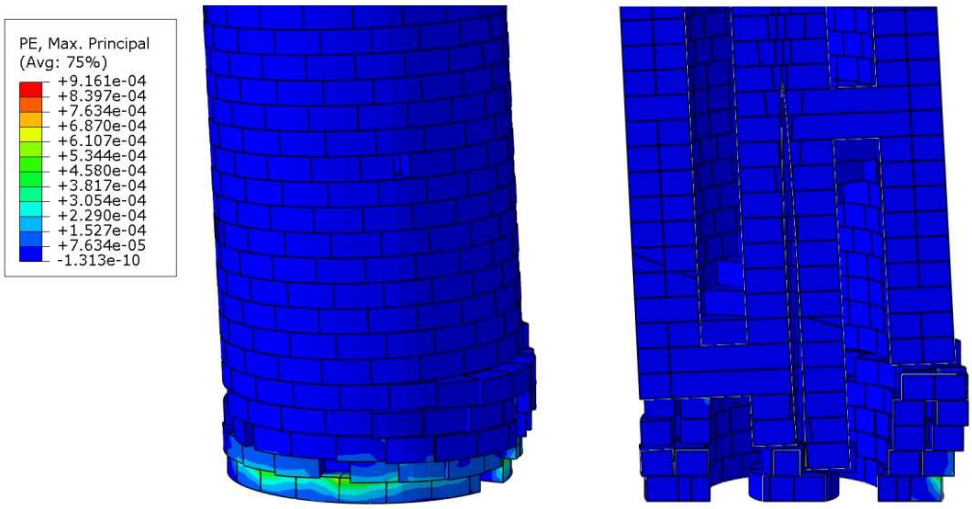

Figure 5.22: Plastic Strain Values and Deformed Shape (scale factor = 10) of "L1" at 14.85th second of Kocaeli Earthquake History.

5.3.2. Results of The Analyses by Using the Model "L2"

In the analyses with Erzincan Earthquake, the dominancy of dissipation by damage is still valid see Figure 5.22. The contribution of other mechanism is significantly less than the damage mechanism. As in the analysis with "L1" the plastic strains and sliding of units concentrate at the bottom of the lighthouse, see Figure 5.23. By investigating the Figure 5.23, it can be stated that separated stones and shifted layers are only seen in the bottom portion of the structure. In addition to that, there is a significant increase in number of separated layers compared with the analysis with "L1".

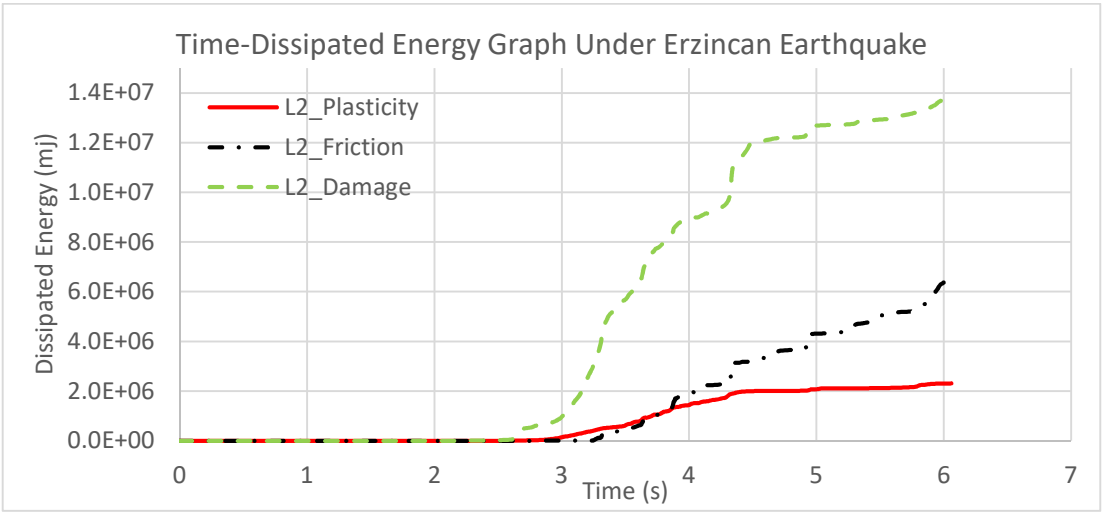

Figure 5.23: Dissipated Energy Values Caused by Different Mechanisms during Erzincan Earthquake History.

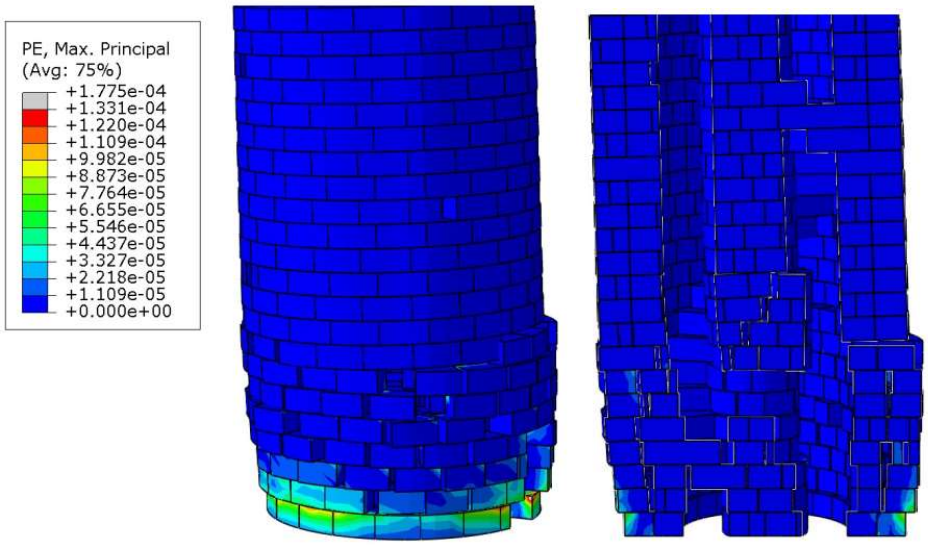

Figure 5.24: Plastic Strain Values and Deformed Shape (scale factor = 15) of "L2" at 6.2nd second of Erzincan Earthquake History.

The analyses with Kocaeli Earthquake suggests that, the dominant mechanism is still damage in cohesive contact surfaces. The dissipation by damage starts at the 8.4th second and after 10th second, rises with a steep slope. At 10.2nd second, the friction and plasticity mechanisms starts with lower slopes. In the Figure 5.24, the comparison of dissipated energy by these three mechanisms is given. At the 12.5th second, it is observed that the plastic strains and separations are concentrated at the bottom portion, see Figure 5.25.

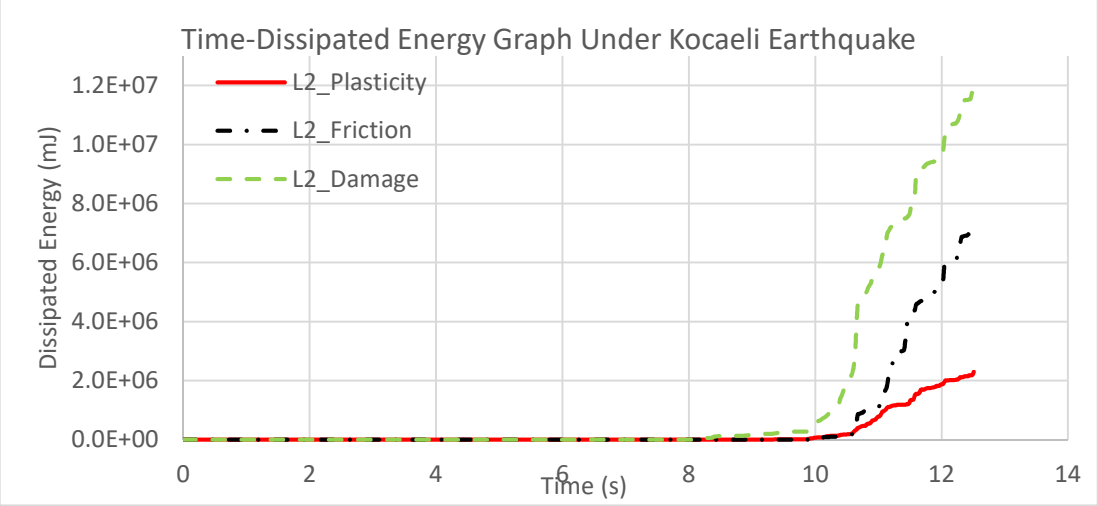

Figure 5.25: Dissipated Energy Values Caused by Different Mechanisms during Kocaeli Earthquake History.

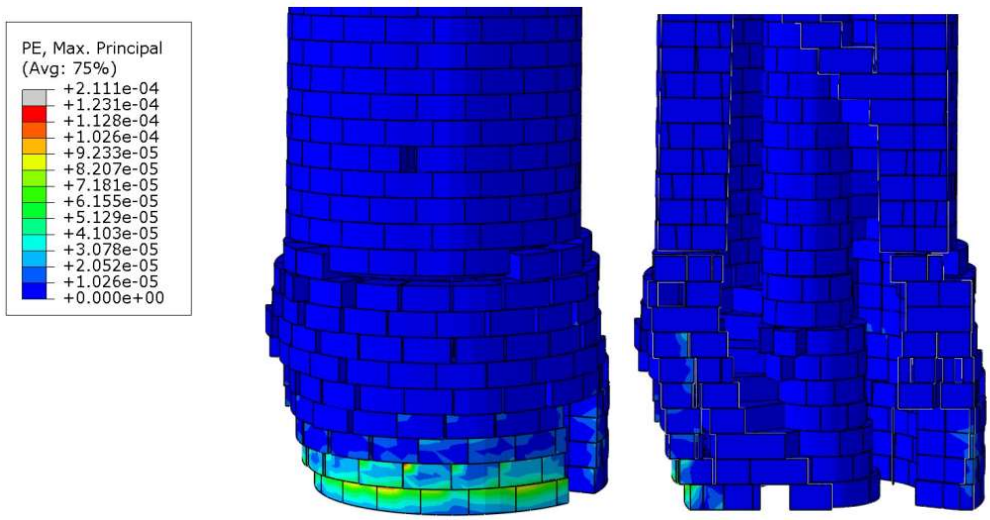

Figure 5.26: Plastic Strain Values and Deformed Shape (scale factor = 15) of "L2" at 12.5th second of Kocaeli Earthquake History.

5.3.3. Results of The Analyses by Using the Model "L3"

In the analyses with Erzincan Earthquake, before the 5th second, the dominant mechanism is damage in cohesive contact surfaces as seen in Figure 5.26. However, towards 5th second, frictional dissipation caught up and slightly after, almost half of the structure from bottom was fallen into pieces. The deformed shape and distribution of plastic strains are shown in Figure 5.27.

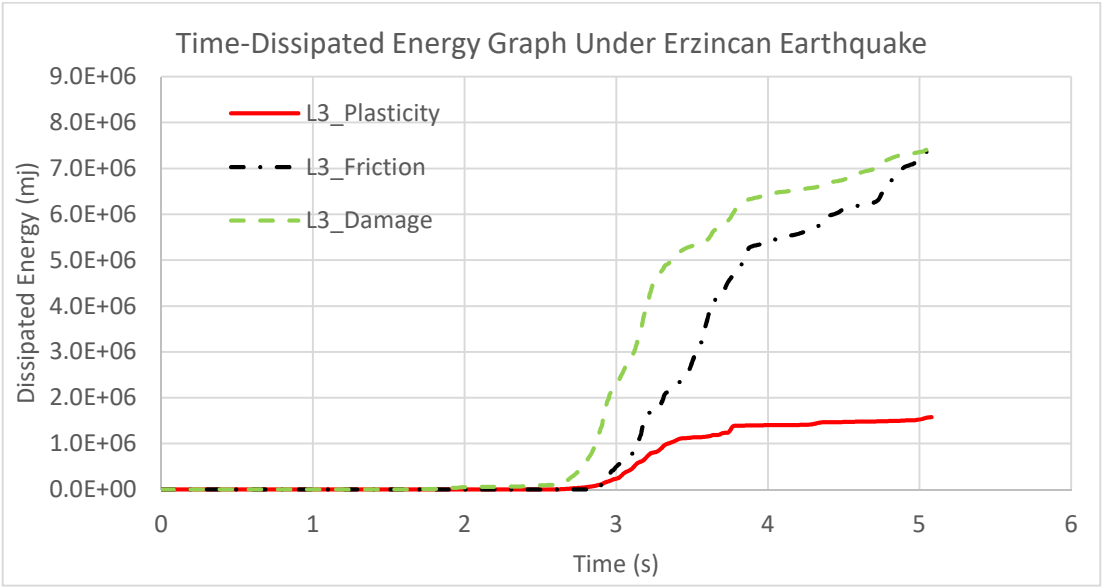

Figure 5.27: Dissipated Energy Values Caused by Different Mechanisms During Erzincan Earthquake History.

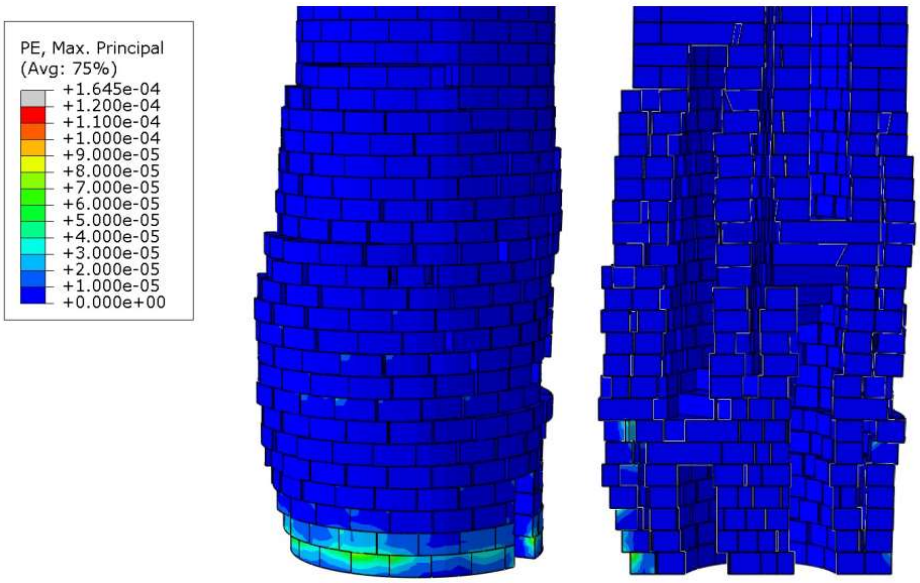

Figure 5.28: Plastic Strain Values and Deformed Shape (scale factor = 15) of "L3" at 5th Second of Erzincan Earthquake History.

In case of Kocaeli Earthquake, the behavior is similar to previous results. Up to 11.5th second, the dominant mechanism is damage in cohesive contacts. However, after that point, dissipated energy by friction is more than the dissipated energy by damage. Influence of plasticity is very low compared with the other mechanisms, see Figure 5.28. At the 11.8th second, the distribution of plastic strains and the separations of joints from middle to bottom of the lighthouse can be seen in Figure 5.29.

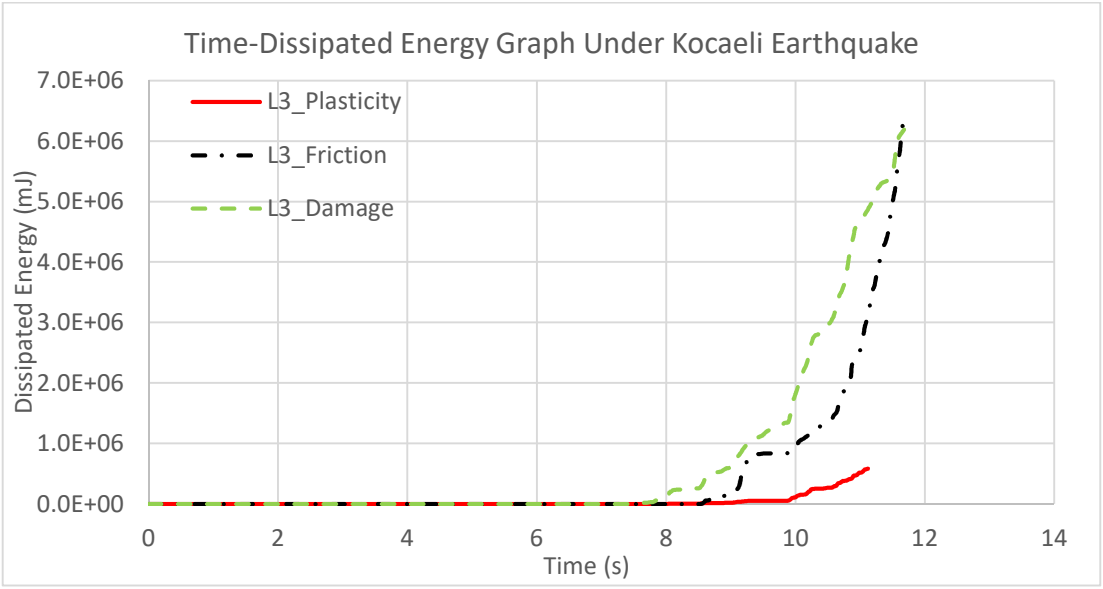

Figure 5.29: Dissipated Energy Values Caused by Different Mechanisms During Kocaeli Earthquake History.

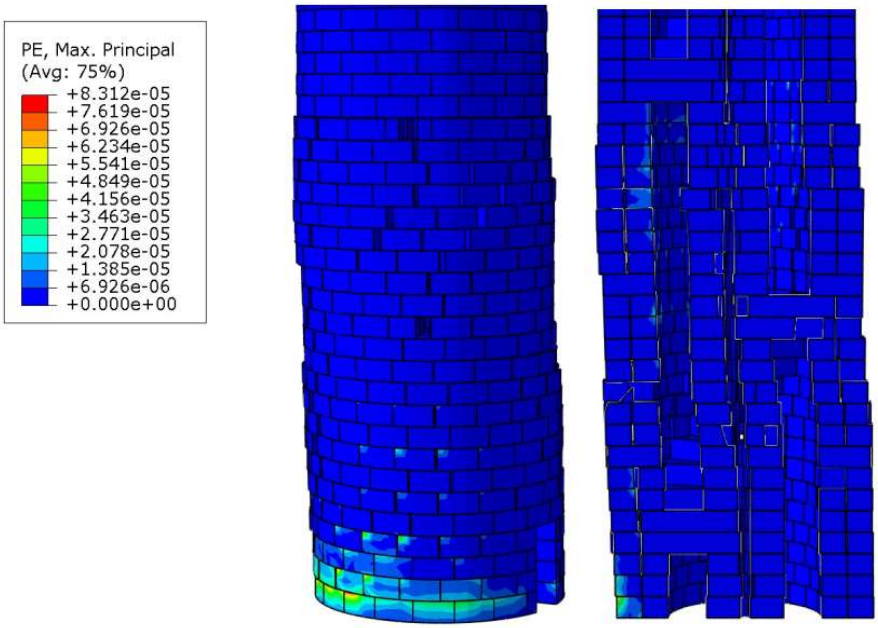

Figure 5.30: Plastic Strain Values and Deformed Shape (scale factor = 15) of "L3" at 11.8th Second of Kocaeli Earthquake History.

5.4. Comparison of Models with Different Properties of Cohesive Contact Surfaces

5.4.1. Dissipated Energy by Friction

In Figure 5.30 and 5.31, the comparison of 3 models (L1, L2 and L3) in terms of dissipated energy by friction during two different earthquakes is given. By comparing the times when the dissipated energy by friction started to increase, it can be said that, using stronger cohesive surface contacts (which represents mortar) delays the failure of the structure.

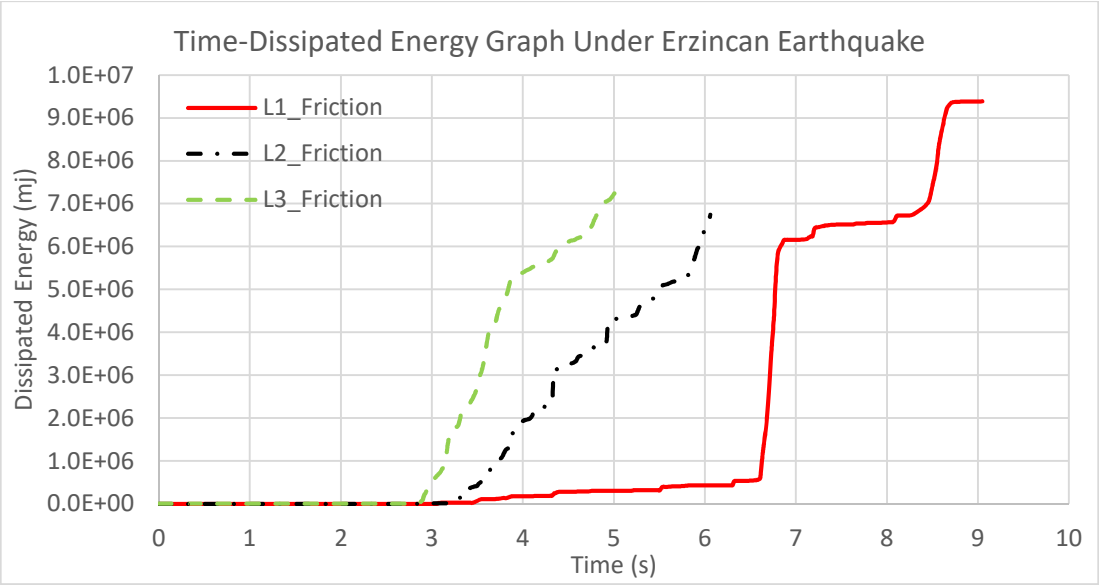

Figure 5.31: Dissipated Energy by Friction During Erzincan Earthquake

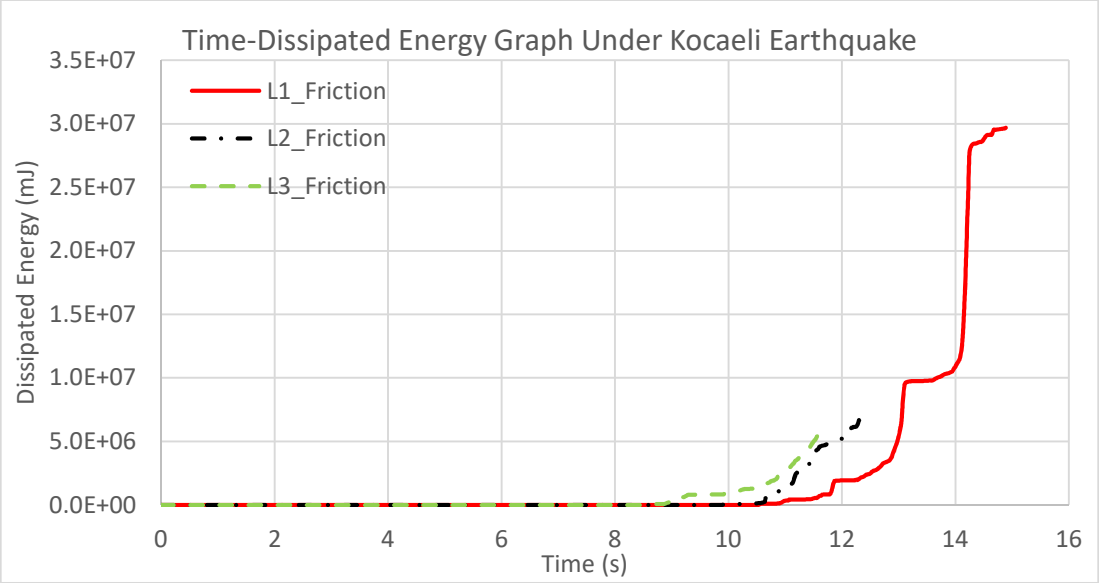

Figure 5.32: Dissipated Energy by Friction During Kocaeli Earthquake

5.4.2. Dissipated Energy by Damage in Cohesive Surfaces

On the basis of the comparisons given in Figure 5.32 and 5.33, any consistent relationship between dissipated energy by damage and properties of cohesive contact surfaces could not be identified. However, as mentioned previous section, it is the first mechanism started to dissipate energy in all cases.

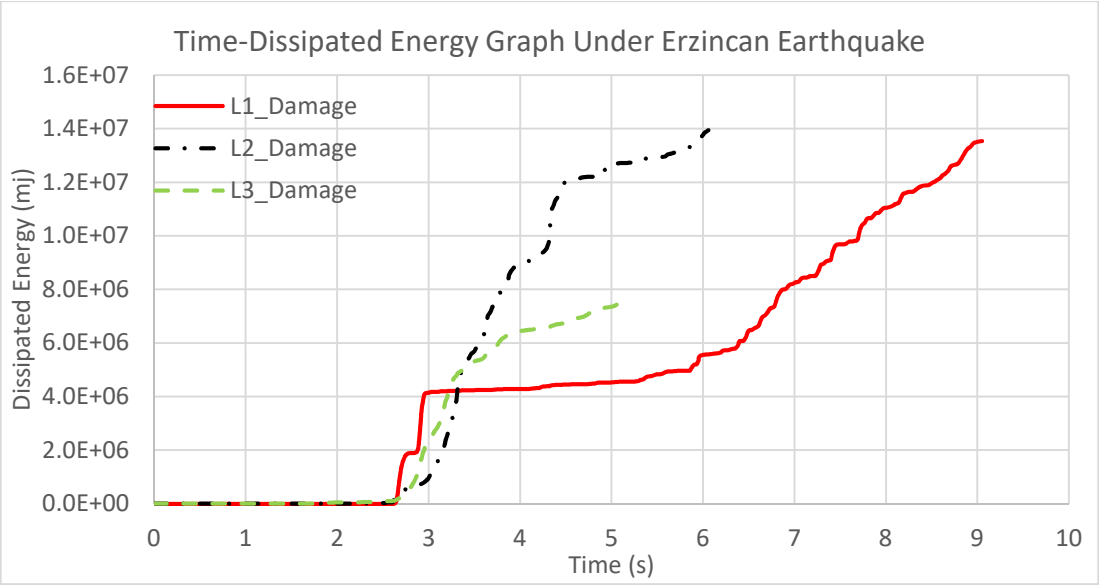

Figure 5.33: Dissipated Energy by Damage in Cohesive Contact Surfaces During Erzincan Earthquake

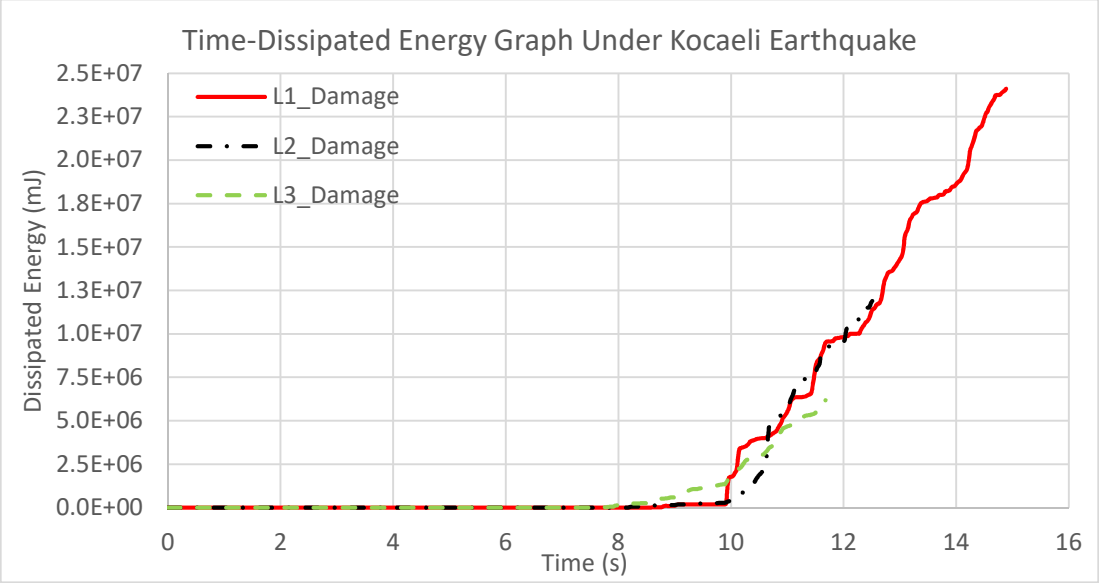

Figure 5.34: Dissipated Energy by Damage in Cohesive Contact Surfaces During Kocaeli Earthquake

5.4.3. Dissipated Energy by Plasticity

In Figure 5.34 and 5.35, comparisons of dissipated energy by plasticity on bulk units between three models (L1, L2 and L3) during different earthquakes are given. This mechanism is the less effective one compared with the other mechanisms. According the to the comparisons shown in Figure 5.34 and 5.35, there is not any consistent trend.

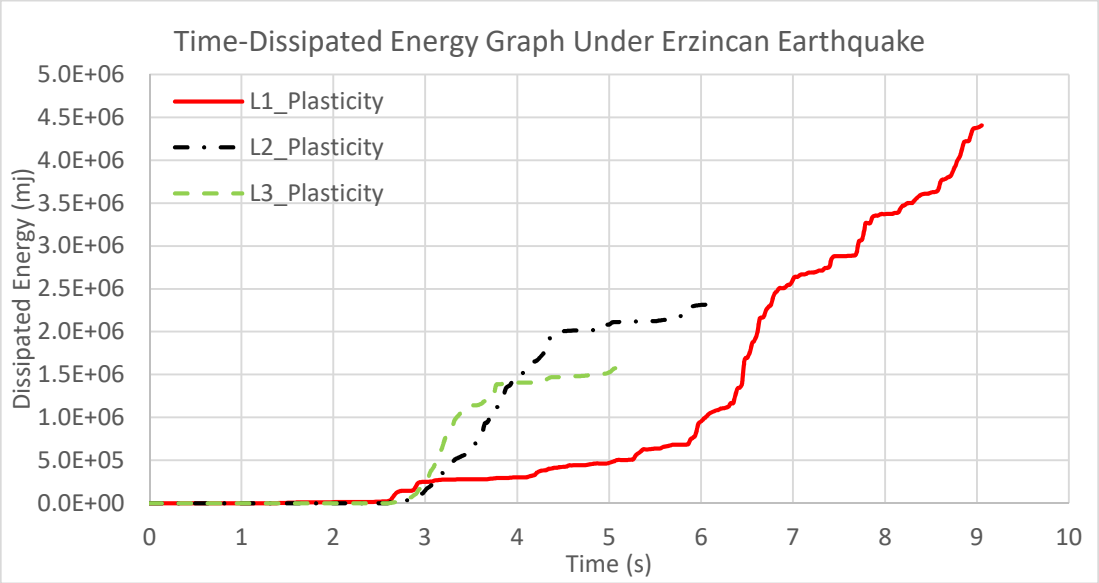

Figure 5.35: Dissipated Energy by Plasticity on Bulk Units During Erzincan Earthquake

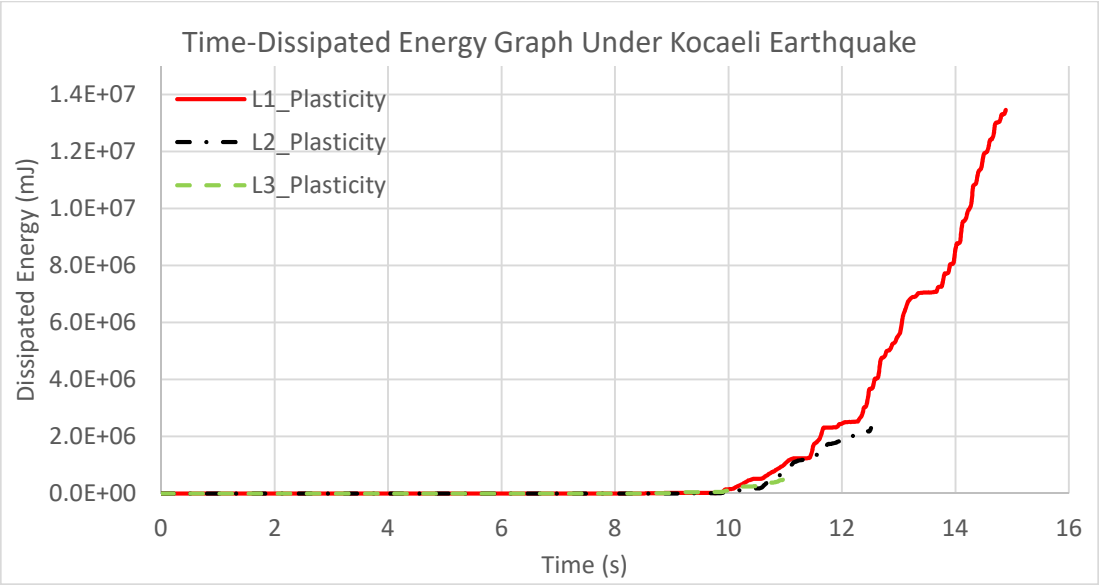

Figure 5.36: Dissipated Energy by Plasticity on Bulk Units During Kocaeli Earthquake

5.5. Failure Modes of the Models

In all analyses, the lighthouse fails under design (scaled according to ZA) earthquakes. The failure starts at the bottom and by following the stair pattern continues

to the top of the lighthouse. Different instants of this failure process are shown in Figure 5.37 and 5.38. In addition to that, in the models with weaker cohesive contact surfaces, the separated number of layers are more than the models with stronger cohesive contact surfaces. In Figure 5.36, deformed configurations of “L1”, “L2” and “L3” models under the same earthquake record are shown.

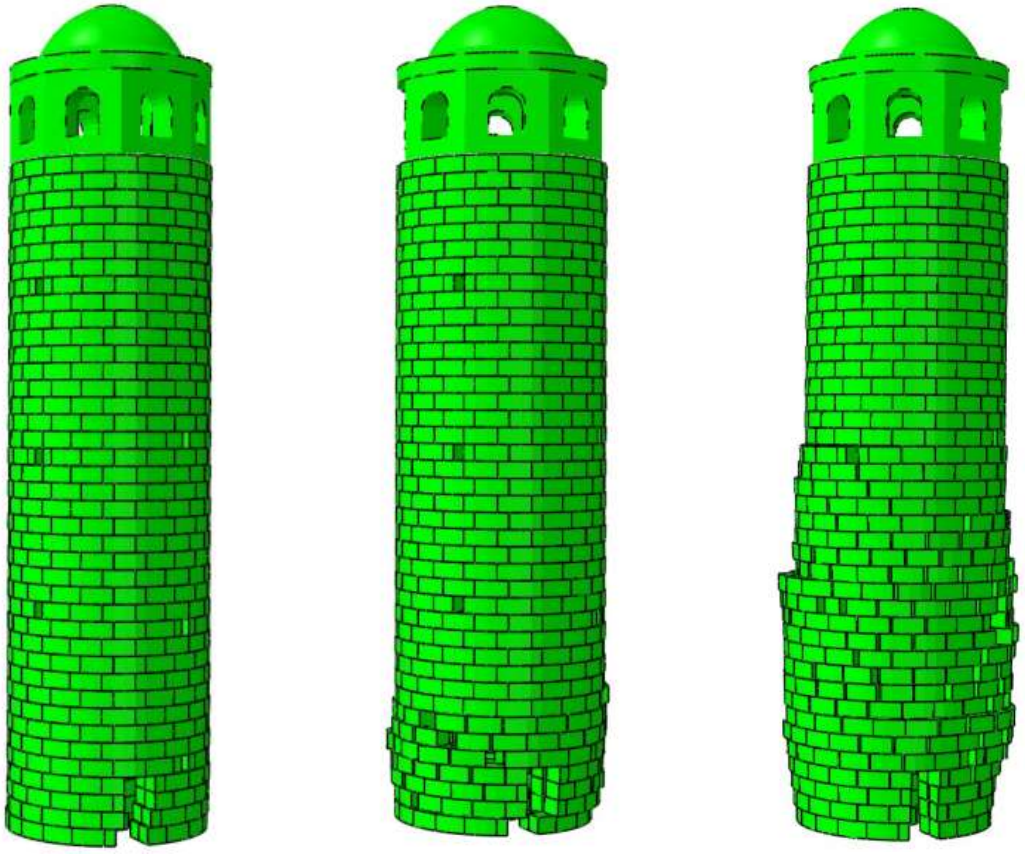

(a) (b) (c)

Figure 5.37: Failure modes of (a) L1, (b) L2 and (c) L3 at the 5.2th second of Erzincan Earthquake

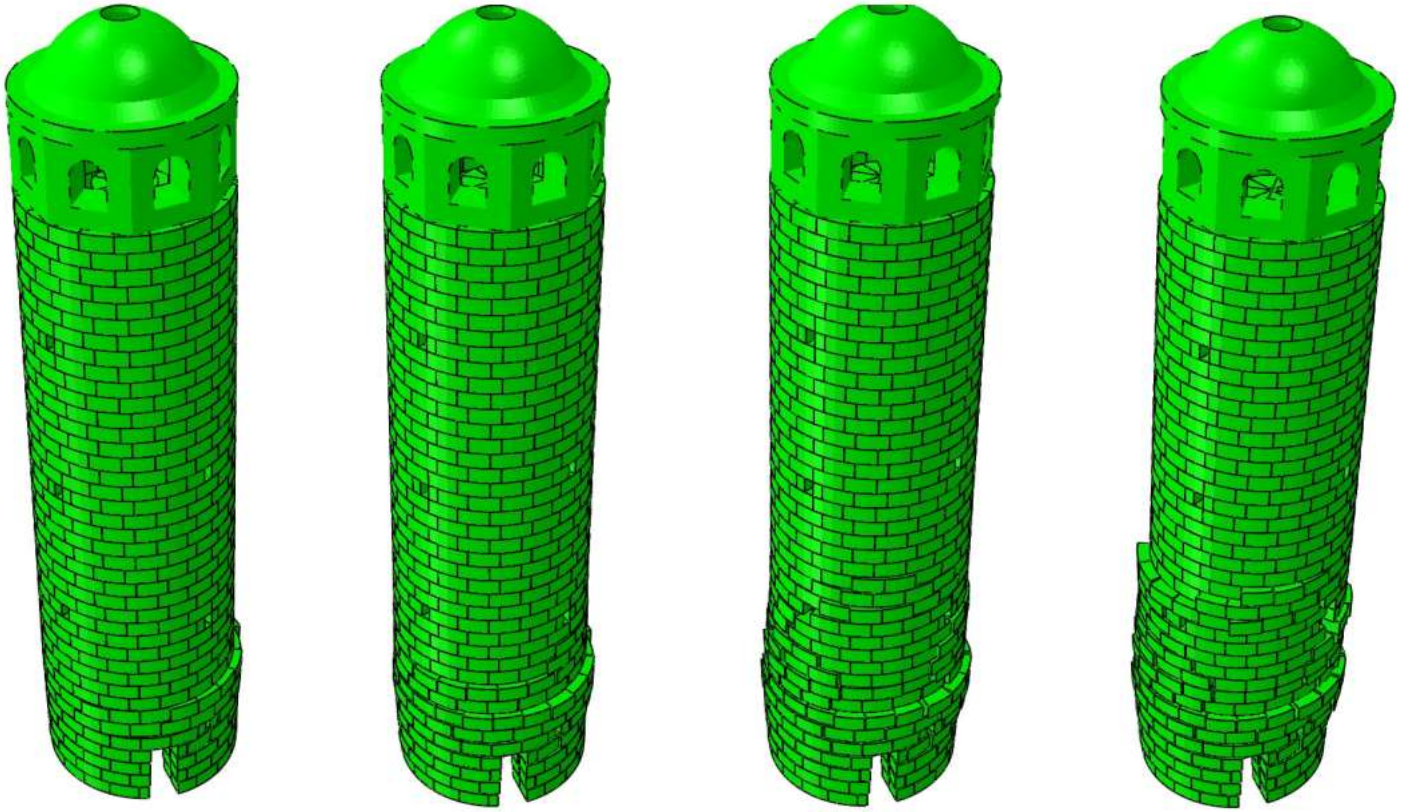

Figure 5.38: From left to right: Deformed states of L3 during Erzincan Earthquake at t=3.2, t=3.3, t=3.4 and t= 3.45, respectively (scale factor = 15)

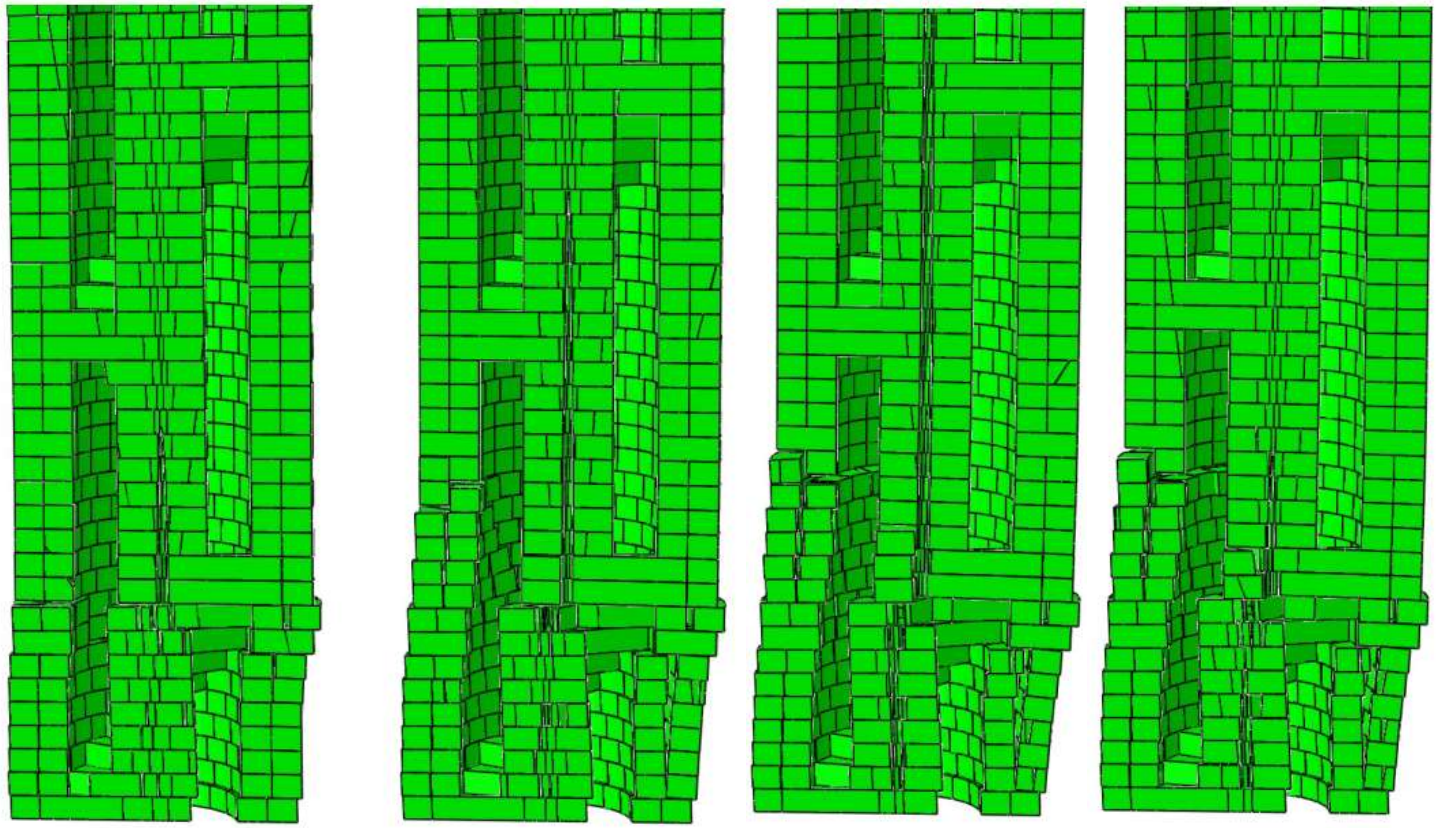

Figure 5.39: From left to right: Cut view of Deformed states of L3 during Erzincan Earthquake at t=3.2, t=3.3, t=3.4 and t= 3.45, respectively

(scale factor = 15)

5.6. Analyses with Scaled Down Erzincan Earthquake Records

In order to determine the earthquake that the lighthouse can withstand, in addition to previous studies, models “L1” and “L2” are investigated under scaled down Erzincan Earthquake (scaled according to the ZA) records. Since the lighthouse fails under design earthquakes, the “matched” accelerograms given in Appendix A are multiplied by 0.25, 0.3, 0.35 and utilized in analyses.

According to the results give in Figure 5.39, the dominant dissipation mechanism is plasticity on bulk units. However, the dissipated energy values are much smaller compared with the results under design earthquake. Since the acceleration values becomes smaller after 4.3rd second of the earthquake, see Figures A.1 and A.3, the increase in dissipated energy by plasticity stops. In the analysis with “L1” and scale factor as 0.25, there is no separation and damage in cohesive surface contacts. Therefore, the lighthouse (L1) can stand this earthquake.

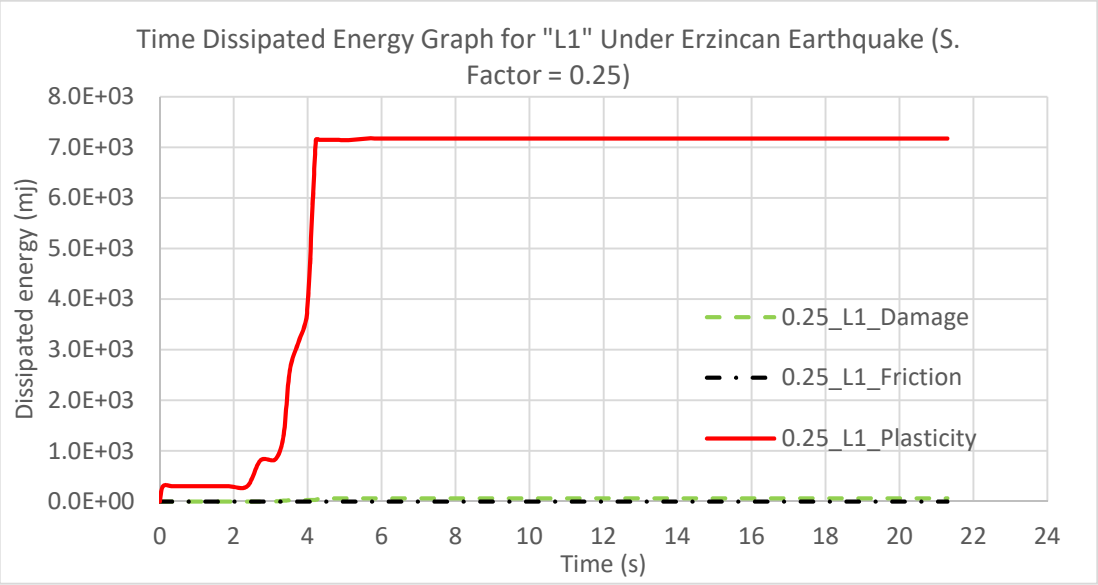

Figure 5.40: Dissipated Energy Values Caused by Different Mechanisms in “L1” During Erzincan Earthquake History (Scale factor = 0.25).

In the Figure 5.40, the dissipated energy values for different mechanisms in model "L2" are given. According to the results, the dominant mechanism is damage in cohesive contact surfaces. However, there is no dissipated energy by friction. It means that stones do not slide at any level of the lighthouse. Therefore, it can be said that the lighthouse with weaker mortar (cohesive surface properties of L2, see Table 5.2) can stand this earthquake.

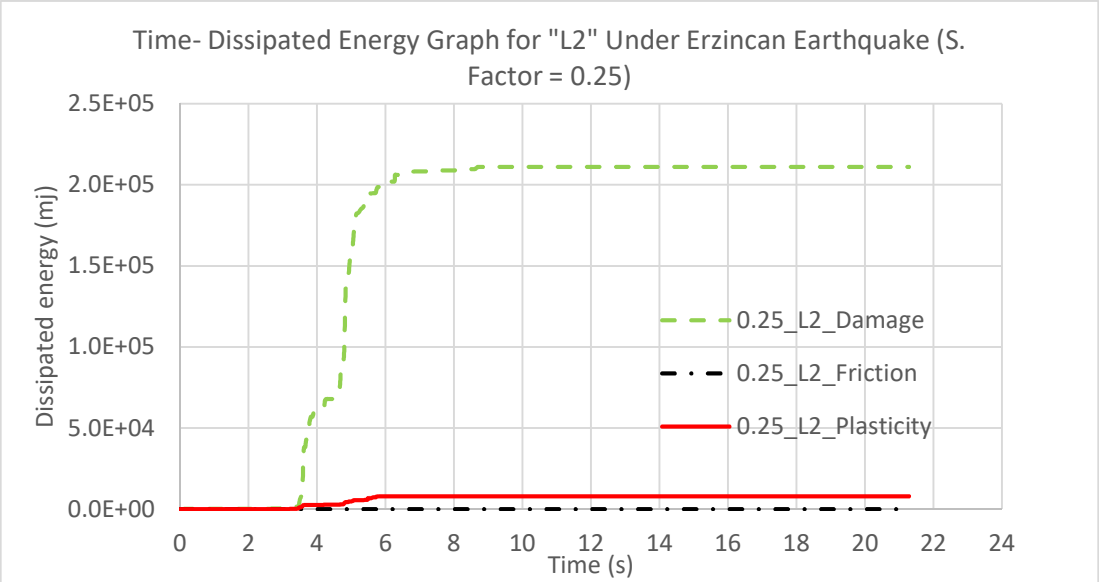

Figure 5.41: Dissipated Energy Values Caused by Different Mechanisms in "L2" During Erzincan Earthquake History (Scale factor = 0.25).

As shown in Figure 5.41, the dominancy of damage mechanisms does not change when the scale factor is equal to 0.3. However, the amount of dissipated energy by damage increased to about 90 times. Compared with the analyses with scale factor as 0.25, after 3.4th second, there is an increase in dissipated energy by plasticity. The amount of this dissipated energy is very low compared with the damage mechanism. There is no separation between stones in the lighthouse. It can be understood from that the dissipated energy by friction is equal to zero. Therefore, the lighthouse with stronger mortar (cohesive surface properties of L1, see Table 5.2) can survive this earthquake without having any separation at joints.

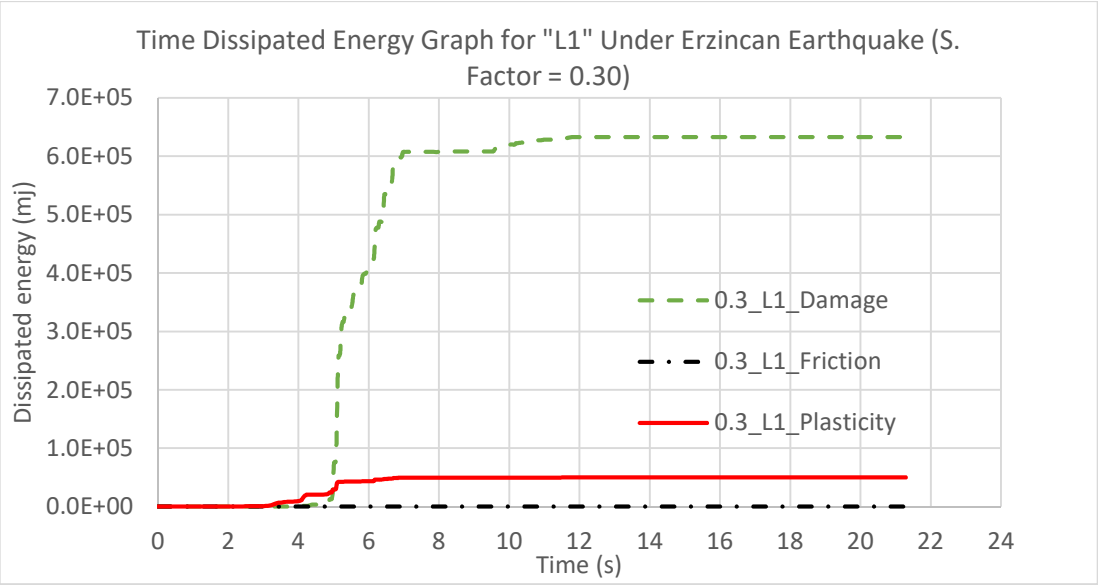

Figure 5.42: Dissipated Energy Values Caused by Different Mechanisms in "L1" During Erzincan Earthquake History (Scale factor = 0.3).

The results of analyses with "L2" and Erzincan Earthquake (scale factor = 0.30) is shown in Figure 5.42. According to the results, the damage in cohesive contact surfaces is the dominant mechanism. Differently from previous analyses, there is an increase in dissipated energy by friction mechanism. It means that there are stones sliding over each other. In Figure 5.43, the deformed shape of "L2" is given. According to this shape, the shifted layers of stones can be detected by investigating the different color contours which means displacement values of nodes. Therefore, it can be said that the lighthouse with weaker mortar can not resist this earthquake without having any sliding layers or separated individual stones. The magnitudes of shifting between layers change from 2 mm to 5 mm approximately.

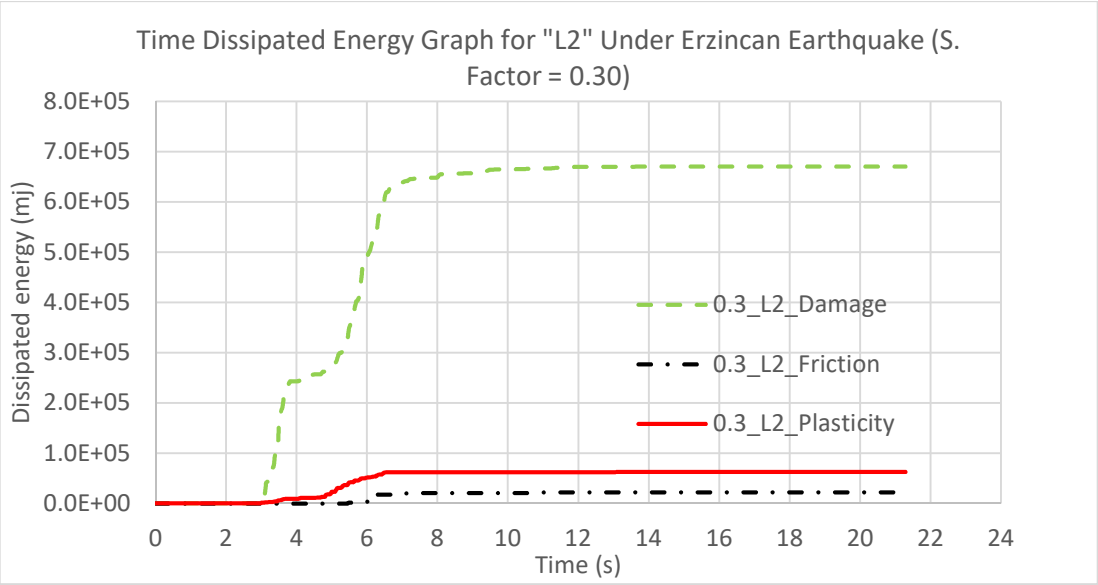

Figure 5.43: Dissipated Energy Values Caused by Different Mechanisms in "L2" During Erzincan Earthquake History (Scale factor = 0.3).

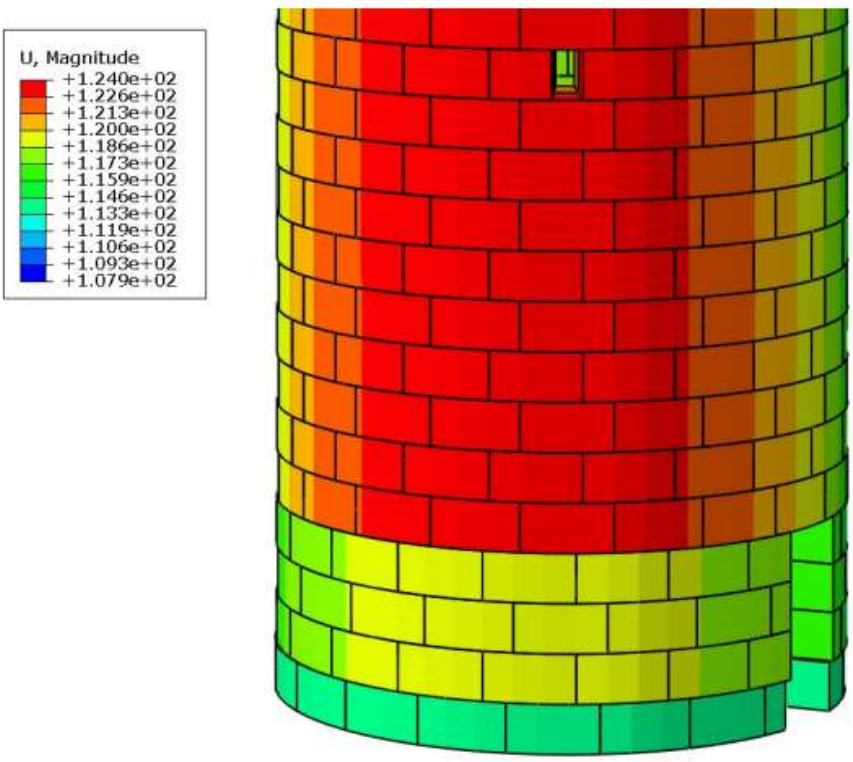

Figure 5.44: Deformed shape of "L2" at the end of Erzincan Earthquake with scale factor equals to 0.3. (The deformations are enlarged 15 times)

From Figure 5.44, it can be stated that the largest energy dissipating mechanism is damage in cohesive contact surfaces. Compared with the previous analyses with “L1”, dissipated energy by plasticity increased to about 3 times. Differently from previous analyses, an increase in dissipated energy by friction is observed after 5.4th second of the earthquake. It means that some cohesive contact surfaces failed and individual stones or layers have started to slide. In the deformed shape, see Figure 5.45, the sliding of the lighthouse can be seen clearly by investigating the difference in contour colors which shows the displacement values of nodes. Therefore, it can be said that the lighthouse with stronger mortar can not resist to this earthquake without losing mortar at some points. The magnitude of shifting at the bottom is about 17 mm.

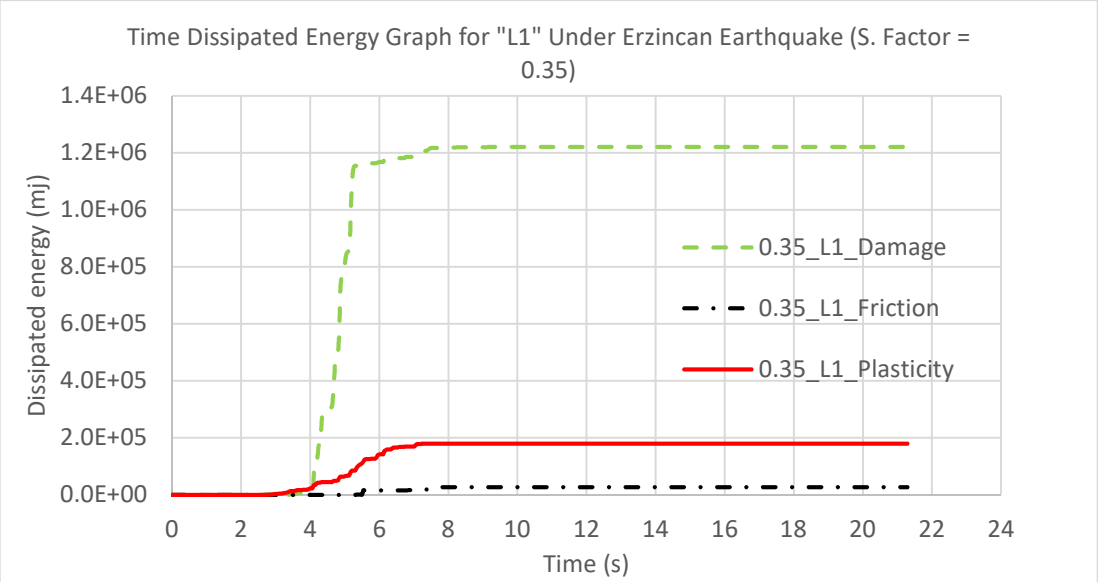

Figure 5.45: Dissipated Energy Values Caused by Different Mechanisms in “L1” During Erzincan Earthquake History (Scale factor = 0.35).

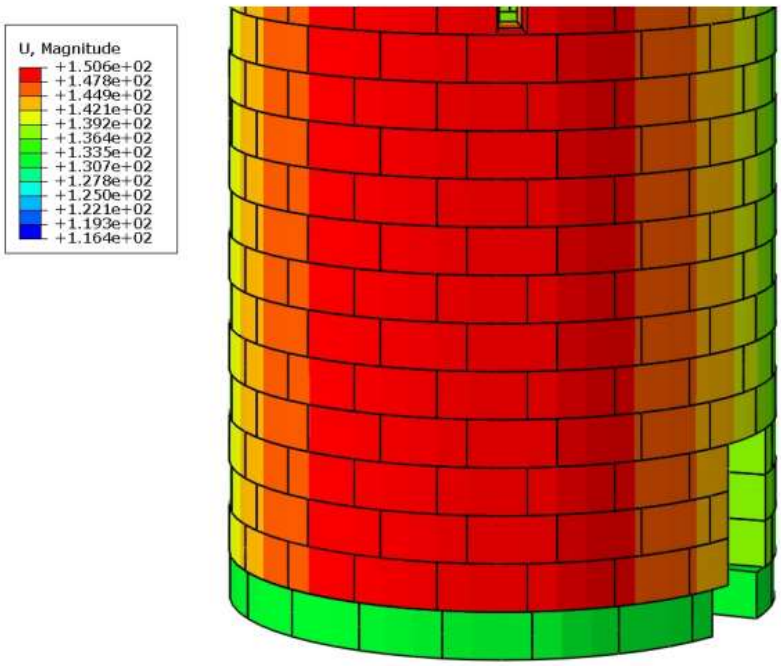

Figure 5.46: Deformed shape of "L1" at the end of Erzincan Earthquake with scale factor equals to 0.35. (The deformations are enlarged 15 times)

The results of analyses with "L2" and Erzincan Earthquake (scale factor = 0.35) is shown in Figure 5.46. In this case, the largest fraction of energy is dissipated by damage mechanism. Compared with the previous analysis with "L2" (with scale factor as 0.3), an expected increase in dissipated energy is observed. It means that, the lighthouse with weaker mortar can not stand this earthquake without having separated joints. The magnitude of shifting between layers can reach to 8 mm approximately. This value is smaller than the analysis with "L1" by using the same earthquake. However, there are more separated layers in this analysis compared with the results of model "L1". The deformed configuration of "L2" under Erzincan Earthquake (scale factor = 0.35) is given in Figure 5.47.

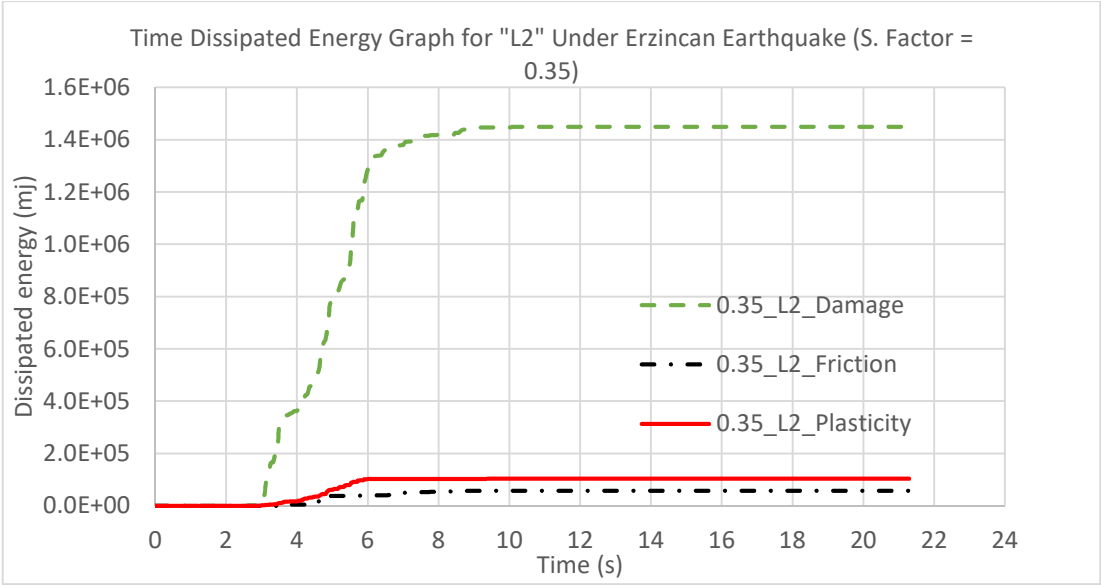

Figure 5.47: Dissipated Energy Values Caused by Different Mechanisms in "L2" During Erzincan Earthquake History (Scale factor = 0.35).

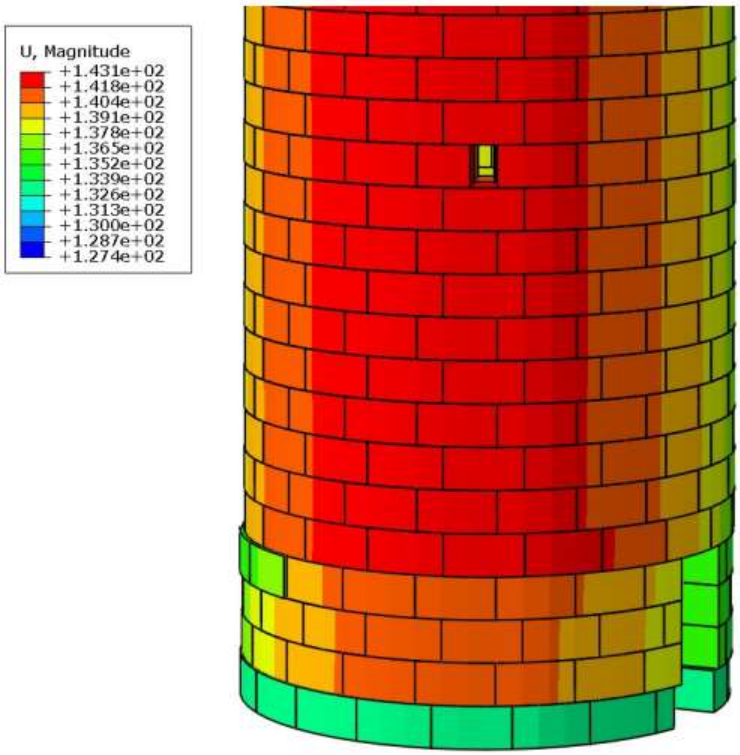

Figure 5.48: Deformed shape of "L2" at the end of Erzincan Earthquake with scale factor equals to 0.35. (The deformations are enlarged 15 times)

According to these results, the model “L1” starts to receive permanent damages when exposed to 35% of the design earthquake, which should be re-evaluated and repaired if necessary. It is the same for model “L2” when exposed to 30% of design earthquake. Considering the observations from previous studies with %100 of design earthquakes, if the lighthouse with mortar properties within these ranges is rebuilt, more serious damages are inevitable as a consequence.

CHAPTER 6

CONLUSIONS AND FUTURE WORK

6.1 Conclusions

In this thesis, the capabilities of meso-scale modeling technique for masonry structures are investigated by means of two experimental studies from the literature and by predicting the seismic response of an ancient lighthouse. One of the experiment investigates the in-plane behavior of a rectangular wall by using a displacement-controlled setup and in the second experiment, the out-of-plane behavior of a wall with a C-shape on plan view was investigated by using a force-controlled setup. After validating the models by comparing with the experimental results, a parametric study was conducted to assess the influence of fracture energies and viscosity parameter. In addition to that, earthquake response of an ancient lighthouse with 3 different parameter sets were investigated. In these analyses, 2 different earthquakes (Erzincan Earthquake and Kocaeli Earthquake scaled according to ZA) were used. Furthermore, the maximum level of earthquake that the lighthouse can stand was tried to be obtained by conducting some additional analyses with scaled records of Erzincan Earthquake. The main findings of the current study can be summarized as follows:

- Modeling a structure with meso-scale modeling technique consumes significant amount of time both during preparation of model and analyses phases. Its use for the analysis and design of ordinary masonry structures seems to be unpractical. However, as far as valuable and unique masonry structures are concerned, the findings of the current study suggest that this approach can be an instrumental tool to predict the seismic response. Although not attempted in this study, investigation of different strengthening options that require detailed analyses can be conducted within this framework. Although in that respect, the current study is a preliminary study.
- A comparison between quasi-static and dynamic/implicit analyses was done in the first validation model. It has been observed that dynamic analysis which lasts 2 seconds gave almost the same results with the results of quasi-static analyses.

- According to the parametric study in first validation model, 50% increase and decrease in normal fracture energy did not affect the in-plane behavior of the wall. On the other hand, the in-plane behavior of the wall was influenced by 50% increase and decrease in tangential fracture energy significantly. The changes in tangential fracture energies affected the strength of the wall by 10% approximately in direct proportion.
- Increasing the viscosity parameter in analyses reduced the computational costs but it has been observed that it may make the results unreliable.
- According to the parametric study in second validation, it was observed that %50 increase and decrease in normal fracture energy and tangential fracture energy, did not make any considerable change in out-of-plane of the wall.
- In the analyses with the finite element models of lighthouse, it has been observed that, openings in the lighthouse should be taken into account in finite element model to get more realistic results.
- By means of the finite element results, it can be stated that, the lighthouse which has the mortar with the properties as in model “L1”, “L2” and “L3”, could not resist the design earthquake.
- The dominant mechanism which dissipates energy during earthquake history was the damage in cohesive contact surfaces in finite element models of the lighthouse.
- In such a complex model, the presence of separations at joints may be understood by looking at the dissipated energy values at desired instant of analysis.
- In all analyses with the finite element models of the lighthouse, the plastic strains were accumulated at the bottom portion of the structure.
- When the cohesive contact surfaces got stronger, it delayed the failure of the structure.
- At the same time of the same earthquake, there were more separated stones and sliding layers if the structure has weaker cohesive contact surfaces.
- In the analyses with scaled down Erzincan Earthquake records, separations of joints were observed in the results of analysis with the model “L1” and %35 of the design earthquake. The model “L1” had started to receive permanent separations at joints during %30 of the design earthquake. Beyond these earthquakes, increases in damages and separations are expected. However, the earthquake level that corresponds to the collapse of the lighthouse has not been determined and still needs some further analyses.

6.2 Recommendations for Future Work

- In this thesis, all the analyses were conducted by using dynamic-implicit method. Although an explicit analysis does not fit perfectly to the problem in hand, such an analysis would give the complete response under any earthquake record.
- The definition of cracks in bulk units may be investigated explicitly by defining potential crack surfaces.
- Meso-scale modeling technique may be used in masonry structures which does not have any mortar or have mortar in partial regions.
- In ancient masonry structures, there are some structural details such as shear keys and some metallic component that are used for connection purposes. With a mesoscopic modelling technique, the influence of such details can be investigated.
- Especially in unique and ancient structures, modeling the structure with this technique may be instrumental for structural improvements, strengthening and restoration processes.

APPENDIX A

The earthquake records used in Chapter 5 are scaled by using Seismomatch Software (https://seismosoft.com) with respect to the spectrum of ZA (soil type) in Turkish Earthquake Code. The original and matched accelerograms and spectrums are given in Figure A.1 to Figure A.8.

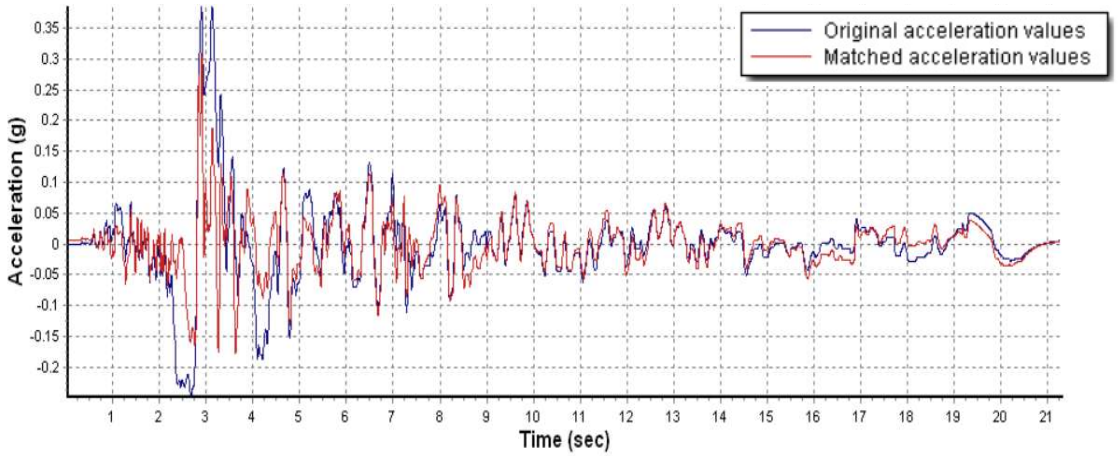

Figure A.1: Original and matched acceleration data of Erzincan Earthquake (North-South direction)

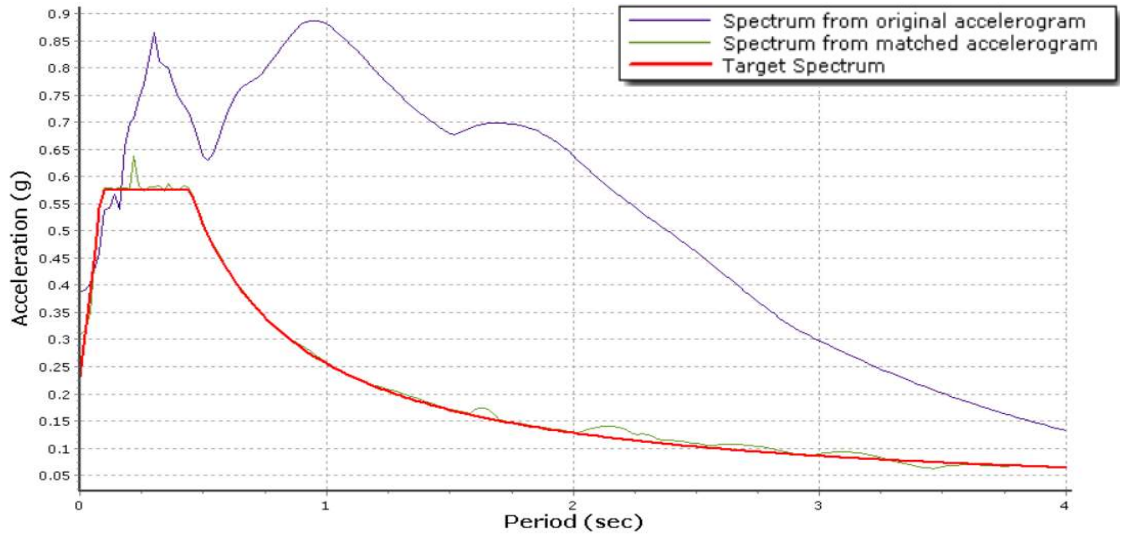

Figure A.2: Spectrums of Erzincan Earthquake (North-South direction)

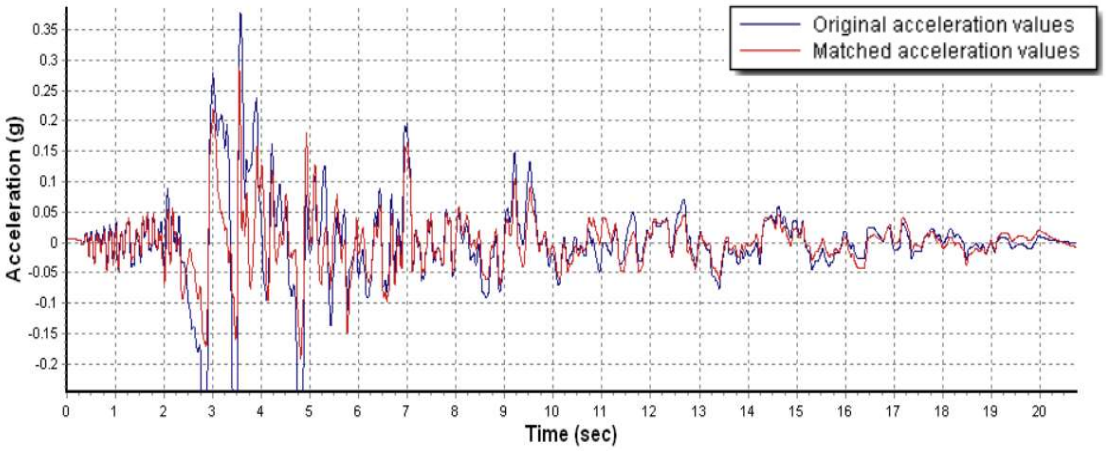

Figure A.3: Original and matched acceleration data of Erzincan Earthquake (East-West direction)

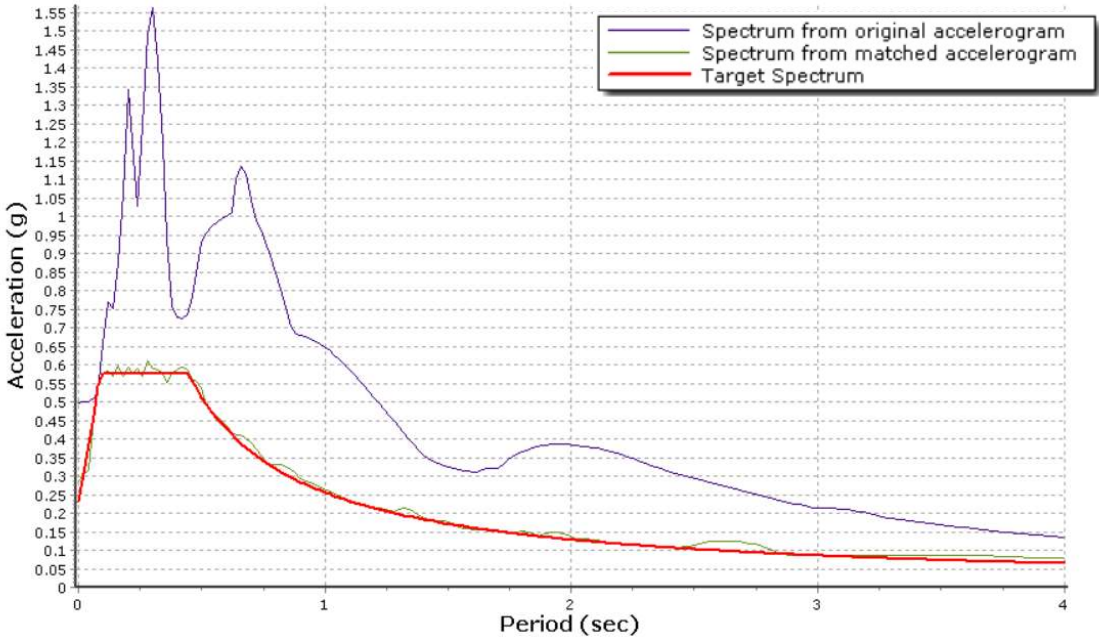

Figure A.4: Spectrums of Erzincan Earthquake (East-West direction)

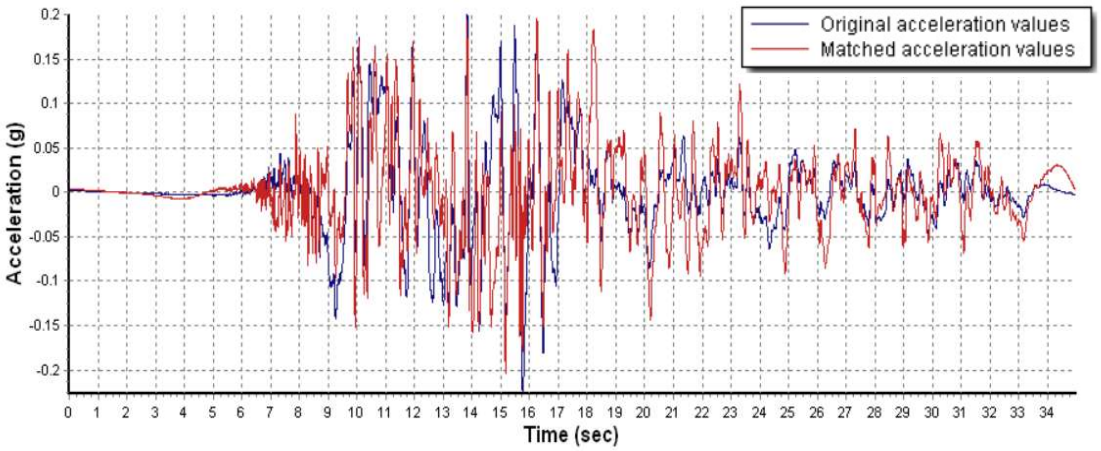

Figure A.5: Original and matched acceleration data of Kocaeli Earthquake (North-South direction)

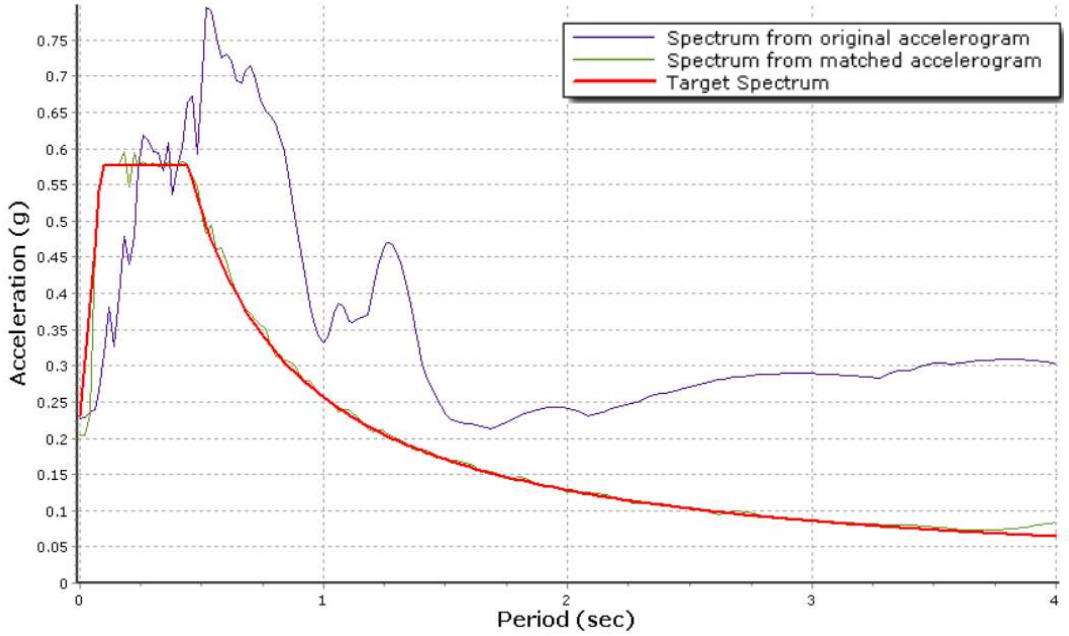

Figure A.6: Spectrums of Kocaeli Earthquake (North-South direction)

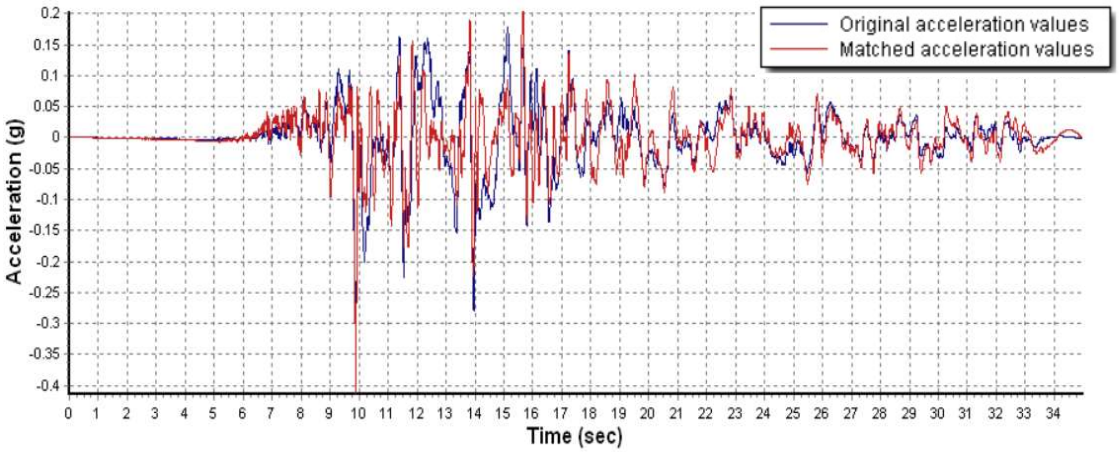

Figure A.7: Original and matched acceleration data of Kocaeli Earthquake (East-West direction)

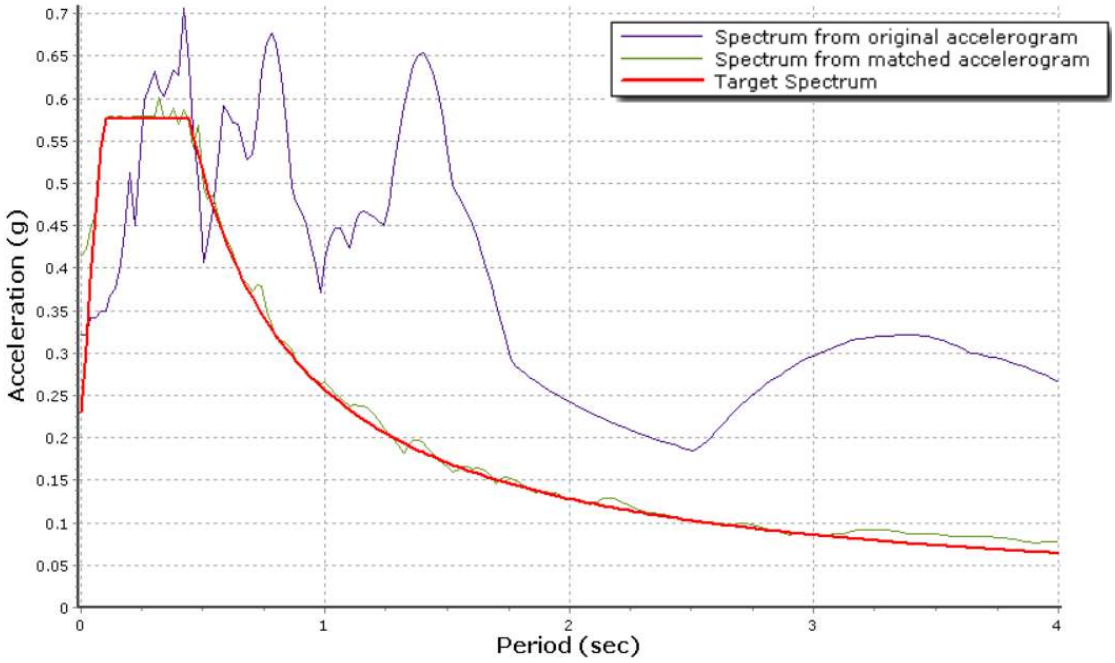

Figure A.8: Spectrums of Kocaeli Earthquake (East-West direction)

REFERENCES

Abbas, Ali Laftah, and Maan H. Saeed. "Representation of The Masonry Walls Techniques By Using FEM." *Australian Journal of Basic and Applied Sciences*, 2017: 39-48.

Abdulla, Kurdo F., Lee S. Cunningham, and Martin Gillie. "Simulating masonry wall behaviour using a simplified micro-model approach." *Engineering Structures , 151. pp.*, 2017: 349-365.

Alatik, Linda, ve Norman Abrahamson. "An improved method for nonstationary spectral matching." *Earthquake Spectra*, 2010: 601-617.

Al-Chaar, Ghassan K., and Armin Mehrabi. "Constitutive models for nonlinear finite element analysis of masonry prisms and infill walls." *DTC Document: Engineer Research and Development Centre-Construction Engineering Resarch Laboratory*, 2008.

Amer, Osama, Basam Saad, and Ahmed Karim. "Finite element anlyses for seismic performance asseessment of historical masonry buildings: the case of Omar Toson Place (Cairo,Egypt)." *Mediterranean Archaeology and Archaeometry, Vol. 17, No 3*, 2017: 13-26.

Ancheta, Timothy D., et al. *PEER NGA-West2 Database.* PEER Report 2013/3, Berkeley: Pasific Earthquake Research Center: University of California, 2013.

Aref, Amjad J., and Kiarash M. Dolatshahi. "A three-dimensional cyclic meso-scale numerical procedure for simulation of unreinforced masonry structures." *Computres and Structures*, 2013: 9-23.

Ashurts, John. *Conservation of Ruins.* Burlington: Butterworth-Heinemann, 2007.

Backes, H.P. *On the behavior of masonry under tension in the direction of the bed joints.* Dissertation, Aachen: Aachen University of Technology, 1985.

Benzeggagh, M. L., ve M. Kenane. "Measurement of mixed-mode delamination fracture toughness of unidirectional glass/epoxy composites with mixed-mode bending apparatus." *Composite Science and Technnology*, 1996: 439-449.

Bull, J.W. *Computational modeling of masonry, brickwork and blockwork structures.* Stirling: Saxe-Coburg Publications, 2001.

Campilho, R.D.S.G, M.F.S.F de Moura, ve J.J.M.S Domingues. "Using a cohesive damage model to predict the tensile behaviour of CFRP single-trap repairs." *Int J Solids Struct*, 2008: 1497-1512.

Dolatshahi, Kiarash M., ve Amjad J. Aref. *Computational, analytical, and experimental modeling of masonry structures.* Technical Report, Buffalo: MCEER, 2015.

Drucker, D. C., ve W. Prager. "Soil mechanics and plastic analysis or limit design." *Q Appl Math*, 1952: 157-165.

Feilden, Bernard M. *Conservation of Historic Buildings.* Burlington: Architectural Press, 2003.

Giordano, A., E. Mele, and A. De Luca. "Modeling of historical masonry structures: comparison of different approaches through a case study." *Engineering Structures*, 2002: 1057-1069.

Griffith, M., ve J. Vaculik. "Out-of-plane flexural strength of unreinforced clay bricks masonry walls." *TMS J*, 2007: 53-68.

Karimian, Simin. *A computational modelling strategy for historic masonry structures.* Phd. Thesis, Leeds: The University of Leeds, 2015.

Kaushik, Hermant B., Durgesh C. Rai, ve Sudhir K. Jain. "Stress-strain characteristics of clay brick masonry under uniaxial compression." *J. Mater. Civ. Eng.*, 2007: 728-739.

Lourenco, P.B. *Computational strategies for masonry structures.* Phd. Thesis, Delft: Delft University of Technology, 1996.

Lourenco, P.B. "Computations on historic masonry structures." *Progress in Structural Engineering and Materials*, 2002: 301-319.

Lourenco, P.B., ve J. Pina-Henriques. "Validation of analytical and continuum numerical methods for estimating the compressive strength of masonry." *Computers and Structures*, 2006: 1977-1989.

Maier, G., E. Papa, ve A. Nappi. "On damage and failiure of brick masonry." *Experimental and Numerical Methods in Earthquake Engineering*, 1991: 223-245.

Özkut, Deniz. *Kültür Varlıklarının Belgelenmesi.* Eskişehir: T.C. Anadolu Üniversitesi Yayınları, 2009.

Park, Joonam, Peeranan Towashiraporn, James I. Craig, ve Barry J. Goodno. "Seismic fragility analysis of low-rise unreinforced masonry structures." *Engineering Structures*, 2009: 125-137.

Pasticier, Laurent, Claudio Amadio, ve Massimo Fragiacomo. "Non-linear seismic analysis and vulnerability evaluation of a masonry building by means of the SAP2000 V.10 code." *Earthquake Engng Struct. Dyn.*, 2007: 467-485.

Pluijm, R. Van Der. "Material properties of masonry and its components under tension and shear." *Proc. 6th Canadian Masonry Symposium.* Saskatoon, 1992. 675-686.

Pluijm, R. Van Der. "Shear behavior of bed joints." *Proc. 6th North American Masonry Conf.* Philadelphia, 1993. 125-136.

Raijmakers, T., ve A.T. Vermeltfoort. “Deformation controlled tests in masonry shear walls.” 1992.

Sacco, Elio. “Micro, multiscale and macro models for masonry structures.” *Mechanics of Masonry Structures*, 2014: 241-291.

Seismosoft. https://seismosoft.com/ (12/25/2020).

Teomete, Egemen. *Finite element modeling of historical masonry structures; case study: Urla Kamanli Mosque.* Msc. Thesis, İzmir: İzmir Institute of Technology, 2004.

Theodossopoulos, D., B.P. Sinha, ve A.S. Usmani. “Case study of the failure of a cross vaults: Church of Hollyrood Abbey.” *Journal of Architectural Engineering* (Journal of Architectural Engineering), 2003: 109-117.

Türkiye Deprem Tehlike Haritaları. https://tdth.afad.gov.tr/ (12/25/2020).